Forward Modeling and Inversion of Viscous Remanent Magnetization Responses in the Time Domain

by

Devin Christopher Cowan

B.Sc., University of Victoria, 2012

A THESIS SUBMITTED IN PARTIAL FULFILLMENT
OF THE REQUIREMENTS FOR THE DEGREE OF

Master of Science

in

THE FACULTY OF GRADUATE AND POSTDOCTORAL STUDIES

(Geophysics)

The University of British Columbia

(Vancouver)

August 2016

Abstract

In this thesis, I develop forward modeling and inversion methods for better characterizing viscous remanent magnetization (VRM) responses in the time-domain. Despite advances since the 1980s, aspects of modeling the VRM response and its impact on time-domain electromagnetic sensors remain elusive. Using Néel relaxation models, I parameterize the off-time viscous remanent magnetization in terms of an amalgamated magnetic property, which I show can be directly obtained using dual-frequency susceptibility measurements. For a half-space model, I derive empirical expressions for characterizing the relationship between the survey geometry and the cartesian components of the VRM response. Final expressions are verified with a 1D forward modeling code and used to determine the cross-over time at which the transient response within a large circular loop becomes dominated by the VRM signal. In order to predict the VRM responses from 3D geological structures, I develop a linear forward modeling code. This is accomplished by discretizing the Earth into a set of cells and implementing the parameterization of the off-time viscous remanent magnetization. Convergence of the forward model as a function of cell size is tested and the code is validated against a 1D code. Lastly, I develop an inversion approach for recovering the distribution of magnetically viscous materials from a set of field observations. A multitude of survey geometries are used to verify that our inversion is robust. A workflow is then presented for removing the VRM response from a set of survey data.

Preface

I, Devin Christopher Cowan, assert that all of the work done in accordance with this thesis is original, and that all external ideas, algorithms and research materials used in this thesis are duly cited.

Table of Contents

List of Tables

List of Figures

Acknowledgments

First and foremost I would like to thank my supervisor, Dr. Doug Oldenburg, for providing an opportunity to study geophysics at the University of British-Columbia. In my opinion, the learning environment in which a graduate student works is a direct reflection of the personality and character of the supervisor. I was fortunate enough to study geophysics in an environment which was inspiring, enthusiastic and friendly.

I would also like to thank Dr. Randy Enkin at the Pacific Geosciences Center for his continued mentorship. I am sincerely grateful to Lin Ping Song for always providing me with useful and comprehensive feedback. Special thanks to Kris Davis and Daniel Bild-Enkin for their tireless work on GIFtools. I would also like to thank the other members of the UBC-GIF group. I know that I have learned a great deal from working with such fantastic people.

Last but not least, I would like to thank my family and friends for their boundless encouragement.

Chapter 1

Introduction

1.1 Research Motivation

Over past decades, geophysical research has generated a number of invaluable tools for answering questions about the Earth's structure. In more recent decades, significant efforts have been made in developing time-domain electromagnetic (TEM) methods. To apply these methods, data are first collected as part of a survey. During the survey, a transmitter is used to generate a time-dependent electromagnetic field which induces a reaction within the Earth. This reaction generates a secondary field, or TEM response, which is then measured by one or more receivers. The distinct characteristics of the TEM response depend on the distribution of materials below the surface and their associated physical properties. Through techniques such as geophysical inversion, data collected during a TEM survey can be used to recover information about a buried target.

Two important applications of TEM methods include mineral exploration and unexploded ordnance (UXO) remediation. In mineral exploration, TEM methods are used to characterize the subsurface distribution of ore-bearing minerals and define other geological structures. This information can be used to infer the margins of ore-bearing rock units, plan drilling programs and assess the economic potential of mineral deposits. As the discovery of deeper and less conventional mineral deposits is needed to meet global demands, an increased emphasis is being placed on further developing these TEM methods.

UXOs are defined as munitions that were armed, fired and remain unexploded through malfunction. Between 1964 and 1973, the United-States released 2.1 million tons of ordnance over Laos alone (Khamvongsa and Russell, 2009). It is estimated that roughly 78 million of the ordnance dropped during this time did not explode and remain a hazard for civilians. Globally, the United Nations approximates that 15,000-25,000 people are killed or maimed each year from land mines and unexploded ordnance. With TEM methods, we can recover the depth and make assumption about the aspect ratios of compact buried objects from their TEM responses. This information can then be used to distinguish potential UXOs from non-hazardous items during remediation efforts.

TEM methods become less effective when the observed response over a geophysical is contaminated by responses from other sources. This is the case in many tropical and sub-tropical regions where lateritic topsoils are

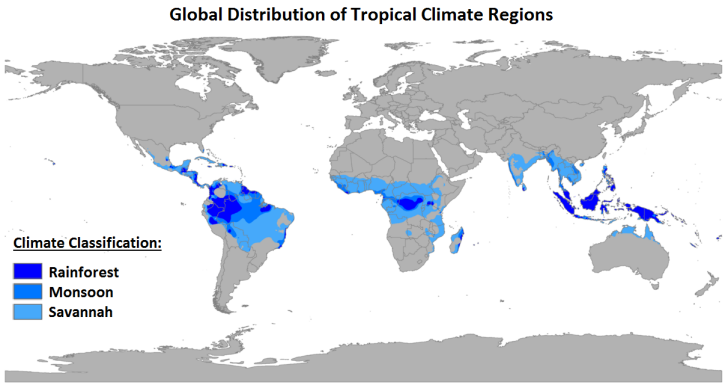

Figure 1.1: Distribution and classification of tropical climate regions according to Köppen-Geiger. This is used to illustrated regions where lateritic soils are most prominent. Adapted from Peel (et al., 2007).

prominent. Lateritic soils are defined has being highly weathered and rich in iron-oxide minerals. These soils have been known to exhibit a distinct magnetic response, called the viscous remanent magnetization (VRM) response, which masks the TEM anomalies from deeply buried conductors and unexploded ordnance items. Given that upwards of 16 % of the Earth's surface is covered by highly weathered iron-rich soils (C. P. B., 1977), the contamination of TEM data by VRM responses represents a challenge in many parts of the world. The global climatic regions in which lateritic soils are most prominent are illustrated in Figure 1.1.

To better understand the impact of lateritic soils on TEM sensors, let us consider an example wherein TEM data are collected over a UXO upon removal of the transmitter's primary field; this is typical of many TEM systems. A representation of non-contaminated and VRM contaminated data is illustrated in Figure 1.2. For data which are not contaminated by the VRM response (left), conventional inversion and discrimination algorithms can be used to infer information about the target from the entire response. For VRM contaminated data (right), the late-time response is masked by the VRM signal. Therefore, only a portion of the observed response can be used to infer information about the target.

Data collected by TEM systems depends on the survey geometry and the subsurface physical properties. Thus it is possible to design a survey which minimizes the impact of lateritic soils on TEM sensors if these geometric relationships are known. Over the past decades, studies have been done to characterize the relationship between the VRM response and the survey geometry (Buselli, 1982; Barsukov and Fainberg, 2001; Pasion et al., 2002; Billings et al., 2003; Pasion, 2007; Zadorozhnaya et al., 2012). Through experimental, analytical and numerical means, researchers have shown that measured VRM responses can be diminished by: separating the receiver from the transmitter, increasing the size of the transmitter loop, or elevating the sensor further above the ground (Buselli, 1982; Lee, 1984; Barsukov and Fainberg, 2001; Das, 2006; Kozhevnikov and Antonov, 2008; Zadorozhnaya et al., 2012). Despite providing significant insight, some details regarding the VRM response and its computation appear elusive. Existing numerical and analytical methods (Lee, 1984; Barsukov and Fainberg, 2001; Billings et al., 2003; Das, 2004, 2006; Kozhevnikov and Antonov, 2008; Pasion, 2007; Druyts et al., 2009) are both complicated and lack sufficient insight regarding the quantitative dependence of the VRM response on the survey geometry.

In addition, the current understanding of the VRM response is mainly drawn from the vertical component. Most importantly, available methods for predicting the VRM response only consider a 1D layered Earth model, and cannot be used to accurately predict the VRM response from 3D bodies.

If the impact of the VRM response cannot be reduced sufficiently by choosing an appropriate survey geometry, then efforts must be made to remove the VRM signal from the data. For UXO application, Pasion (2007) proposed a method based on recovering a best-fitting half-space for the background response. The recovered half-space was then used to predict the background response at other times and locations throughout the survey region. It was proposed that by subtracting the predicted response from the observed data, the response from UXOs could be isolated, and conventional algorithms could be applied. Although successful in many instances, this approach is unlikely to be effective in regions where the lateritic topsoils show large spatial inhomogeneities.

1.2 Thesis Structure and Goals

This thesis is organized as follows. In Chapter 2, a comprehensive review of viscous remanent magnetization is presented. First, I discuss the mineralogy of lateritic soils and its importance to viscous remanent magnetization. Next, mathematical models which describe magnetic viscosity in both time and frequency are presented according to Néel relaxation theory. These are used to explain the nature of the VRM response exhibited by lateritic soils. I define an amalgamated magnetic property for characterizing a soil's magnetic viscosity. I show how the amalgamated magnetic property may be obtained for a given sample using dual-frequency susceptibility measurements. Numerical modeling tools are then used to demonstrate the electromagnetic responses generated by a conductive and magnetically viscous Earth.

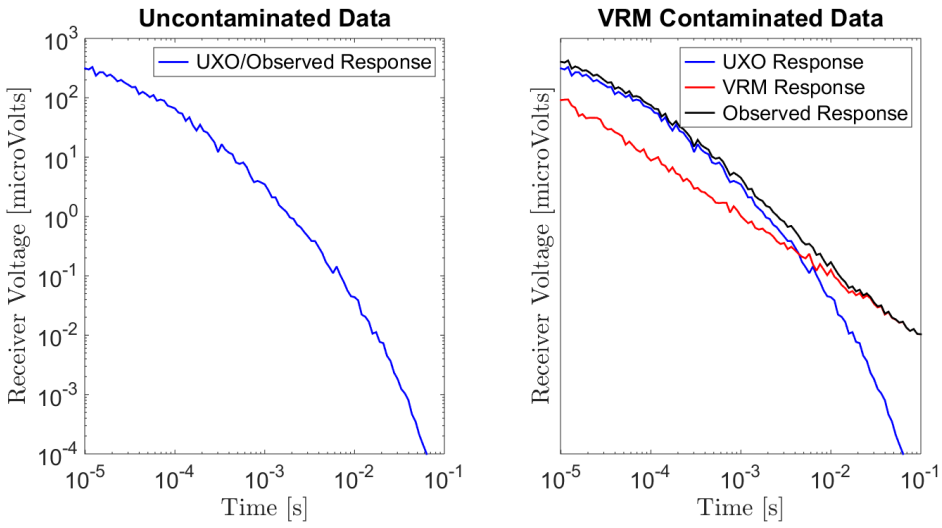

Figure 1.2: Representation of the TEM response over an unexploded ordnance item. On the left, observed TEM data are not contaminated by a VRM response. On the right, TEM data collected at late times are contaminated by a VRM response.

In Chapter 3, I attempt to fill gaps left by previous analytic expressions. I consider a circular transmitter loop over a magnetically viscous half-space and derive simplified analytical expressions for the vertical and horizontal components of the VRM response. Hankel-integral based expressions are approximated empirically so that numerical integration of elementary integrals is not required. Final expressions are used to investigate the dependence of the VRM response on the survey geometry; most notably, the size of the transmitter loop. In addition, I investigate the critical time at which the transient response within a large circular loop becomes dominated by the VRM signal. Analytical expressions derived in this chapter are intended to act as a preliminary survey design tool in regions where lateritic soils are prominent. Ideally, they can be used to choose an appropriate transmitter loop size and select an optimal range of observation times.

In Chapter 4, I present a three-dimensional forward model for predicting the off-time VRM response from a viscously magnetized body. This is accomplished by discretizing the source region into a set of cubic cells and parameterizing the off-time viscous remanent magnetization in each cell in terms of the amalgamated magnetic property.

In Chapter 5, inversion is used to recover the amalgamated magnetic property for each cell from a synthetic set of field observations. To test the versatility of the inversion, I consider data collected using several survey configurations. Using inversion, I describe a workflow for removing the contaminating VRM response from a set of TEM data.

Conclusions and future research are discussed in Chapter 6.

Chapter 2

Geophysical Responses due to Viscous Remanent Magnetization

2.1 Introduction

In this chapter, I examine the magnetic properties which characterize lateritic soils, as well as the distinct magnetic response they exhibit. I begin by discussing the source of the soil's magnetic response. Next, the fundamental theory of viscous remanent magnetization (VRM) is presented according to Néel relaxation theory. This is used to derive several mathematical models, capable of characterizing the time and frequency-dependent excitation of magnetically viscous soils. Parameters which define these models represent a set of diagnostic magnetic properties for the soil. The magnetostatic and frequency-dependent magnetic properties for iron-bearing soils are discussed. I show how simple dual-frequency measurements can be used to obtain important information regarding a soil's magnetic viscosity. This information can be used to characterize the soil's off-time magnetic response. Finally, the geophysical response from a conductive and magnetically viscous Earth is examined by considering an inductive source on the surface of a half-space. Both time and frequency-domain responses are modeled.

2.2 The Magnetization in Iron-Bearing Soils

The magnetic properties of soils are predominently attributed to the presence of iron-bearing minerals. These minerals can be both petrogenic or pedogenic in origin. Ferrimagnetic iron-oxides, namely magnetite, titanomagnetite and maghemite, represent a primary contribution towards the soil's magnetic characteristics (Igel et al., 2012). Of these iron-oxide minerals, magnetite is the most magnetic as well as the most important when considering the impact of magnetic soils on EM sensors (Pasion, 2007). If sufficiently abundant, paramagnetic silicate minerals also influence the magnetic characteristics of the soil. Anti-ferrimagnetic minerals, most notably hematite, exhibit weak magnetization. As a result, their contribution to the overall magnetic characteristics of the soil is frequently negligible.

The majority of magnetic minerals are paramagnetic (Dunlop and Özdemir, 1997). In paramagnetic minerals, individual electron magnetic moments will partially align themselves along the direction of an applied magnetic

field; thus magnetizing the material. Magnetization is the vector sum of individual magnetic moments per unit volume. Paramagnetic magnetization $\vec{M}$ is linearly proportional to the strength of the applied field $\vec{H}$, provided the field is not too strong (Griffiths, 2007):

$$\vec{M} = \chi \vec{H} \tag{2.1}$$

The constant of proportionality χ, is known as the magnetic susceptibility, and is used to characterize the magnetic properties of a material. Magnetic field strength and magnetization are both expressed in units of Ampères per metre [A/m]. Magnetic susceptibility is therefore defined in units of [A/m]/[A/m]; however, it is usually expressed as a unitless quantity. The density of total magnetic flux within a material is denoted by $\vec{B}$, and is expressed in units of Teslas [T]. In susceptible materials, induced magnetization will generate a contribution towards the total magnetic flux density. For most minerals, the relationship between $\vec{B}$ and the applied magnetic field is linear (Griffiths, 2007):

$$\vec{B} = \mu \vec{H} = \mu_0 \big[1 + \chi\big] \vec{H} = \mu_0 \big[\vec{H} + \vec{M}\big] \tag{2.2}$$

where μ is defined as the material's magnetic permeability. Magnetic permeability is expressed in units of Henrys per metre [H/m], or Tesla meters per Ampère [T $\cdot$ m/A]. The permeability of free-space is denoted by $\mu_0 = 4\pi \times 10^{-7}$ H/m. According to Eq. (2.2), $\mu = \mu_0 \big[1 + \chi\big]$. Therefore, the magnetic permeability can be considered a diagnostic magnetic property for susceptible materials.

Ferromagnetic minerals, as well as ferrimagnetic minerals, hold spontaneous magnetization below their Curie temperature. There are volumes within magnetic minerals, where electron magnetic moments are roughly aligned along a single direction. These volumes are known as magnetic domains. Magnetic domains are separated by surfaces, roughly 100 nm in width, called domain walls. Grains containing more than one magnetic domain are known as multi-domain grains (MD). MD grains are capable of holding permanent magnetic remanence. However, the migration of domain walls occurs under minimal stress, and the magnetization exhibited by MD grains is relatively unstable. Grains which are too small to accommodate domain walls are known as single-domain (SD) grains. The magnetization of SD grains is uniformly aligned throughout the entire grain. As a result, they are typically stable carriers of strong permanent magnetic remanence. In very small ferromagnetic and ferrimagnetic nanoparticles, thermal energy competes with magnetic anisotropy which attempt to maintain the coherent magnetization direction. As a result, these magnetizations are very unstable, and can experience random changes in direction over the course of an observation. This property is known as superparamagnetism, and occurs in ferrimagnetic iron-oxide minerals below 1 nm to some tens of nanometers in diameter, depending on mineral type, grain shape and temperature (Thompson and Oldfield, 1986; Dearing et al., 1996; Igel et al., 2012). Superparamagnetic (SP) grains mimic the paramagnetism exhibited by most minerals, only much stronger. The magnetization experienced by a collection of SP grains, in response to an applied field, can be referred to as superparamagnetic magnetization. SP magnetization along the direction of an applied field occurs less rapidly than regular paramagnetic magnetization. This property is known as viscous remanent magnetization, magnetic viscosity, or magnetic after-effect, and is commonly described using relaxation models (Néel, 1949; Buselli, 1982; Moskowitz, 1985; Dabas et al., 1992; Billings et al., 2003; Pasion, 2007). A comprehensive description of ferro, ferri, and superparamagnetism is covered in Dunlop and Ozdemir (1997).

When exposed to an applied magnetic field, magnetic soils experience an instantaneous change in magnetization (Dunlop and Özdemir, 1997). Some iron-bearing soils however, exhibit strong magnetic viscosity due to an abundance of SP iron-oxide grains (Mullins and Tite, 1973; Dabas et al., 1992; Pasion, 2007). This is prominently observed in highly weathered lateritic soils (Dabas et al., 1992; van Dam et al., 2008; Meglich et al., 2008; Igel et al., 2012, 2013). As a result of their magnetic viscosity, iron-bearing soils are characterized by frequency dependent magnetic susceptibilities (Lee, 1984; Dabas et al., 1992; Fannin and Charles, 1995; Meglich et al., 2008). The magnetic susceptibility of an iron-bearing soil depends on its parent material, and the extent of physical, chemical and biological weathering it has undergone (van Dam et al., 2008; Igel et al., 2012). Mature soils tend to exhibit stronger magnetism, and a higher degree of frequency dependence. In rock magnetism, frequency dependent magnetic susceptibilities are expressed using thermal relaxation models developed by Louis Néel (Néel, 1949; Buselli, 1982; Moskowitz, 1985; Dabas et al., 1992; Billings et al., 2003; Pasion, 2007). Néel modeled the magnetic viscosity by considering a collection of non-interacting SP single-domain grains (Néel, 1949).

2.3 Mathematical Models for the Magnetization of Iron-Bearing Soils

2.3.1 Magnetic Susceptibility of Iron-Bearing Soils

Magnetic susceptibility defines the degree of induced magnetization experienced by a material, proportional to the strength of an applied magnetic field. The magnetic susceptibility represents an important diagnostic property for magnetic materials. In iron-bearing soils, the induced magnetization depends on the frequency of the applied field (Lee, 1984; Dabas et al., 1992; Fannin and Charles, 1995; Meglich et al., 2008). As a result, these soils are characterized by frequency dependent magnetic susceptibilities. For a theoretical sample, the frequency dependent magnetic susceptibility can be described using a Debye model (Mullins and Tite, 1973; Dabas et al., 1992; Pasion, 2007; Meglich et al., 2008), which assumes all SP grains are identical:

$$\chi(\omega) = \chi_\infty + \frac{\Delta\chi}{1 + i\omega\tau} \tag{2.3}$$

where ω is the angular frequency in rad/s, and τ is the time relaxation constant for the collection of SP grains. The infinite frequency susceptibility χ_∞, is used to represent any instantaneous magnetization exhibited by the sample. Under the influence of a magnetostatic field, SP magnetization is at equilibrium, and $\chi(\omega \to 0) = \chi_\infty + \Delta\chi$. Thus, $\Delta\chi$ represents the zero-frequency magnetic susceptibility of all SP grains. For non-viscous materials, $\Delta\chi = 0$. For changing applied fields, SP magnetization cannot reach this equilibrium, and exhibits quadrature components over the mid-frequency range. For smaller values of τ, SP magnetization will adjust more rapidly to changes in the applied field. At high frequencies, SP grains are incapable of generating an induced magnetization along the applied field before it changes, and $\chi(\omega \to \infty) = \chi_\infty$.

The time relaxation constant (τ) is given by the Néel relaxation time (Néel, 1949):

$$\tau = \tau_0 \, exp\left(\frac{E_b}{k_B T}\right) \tag{2.4}$$

where k_b is the Boltzmann constant, T is the absolute temperature, and $\tau_0 \sim 10^{-9}$ s is the "attempt time" (Dunlop and Ozdemir, 1997). The energy barriers which maintain the current orientation of individual SP grains, are represented by E_b. In natural soils, E_b is not the same for all SP grains. According to Eq. (2.4), this implies the collection of SP grains within a soil is characterized by a distribution of time-relaxation constants. The distribution is highly sensitive to the volumes of individual SP grains. This is discussed in Appendix A. The distribution of time relaxation constants is represented using a weighting function $f(\tau)$. By applying the weighting function and integrating over all Debye models, the magnetic susceptibility is expressed as (Mullins and Tite, 1973; Dabas et al., 1992; Pasion, 2007; Meglich et al., 2008):

$$\chi(\omega) = \chi_\infty + \Delta\chi \int_0^\infty \frac{f(\tau)}{1+i\omega\tau} d\tau \tag{2.5}$$

The magnetic viscosity observed in iron-bearing soils is characterized by its weighting function. The majority of soil samples can be adequately fit by assuming a log-uniform distribution of time relaxation constants between a set of finite limits (Dabas et al., 1992; Worm, 1998; Igel et al., 2012). These limits correspond to ferrimagnetic grains sizes in which superparamagnetic behaviour is no longer apparent over the duration of a measurement. The weighting function for a log-uniform distribution of time relaxation constants is defined by (Mullins and Tite, 1973; Dabas et al., 1992; Billings et al., 2003; Das, 2006):

$$f(\tau) = \begin{cases} \dfrac{1}{\tau\, ln(\tau_2/\tau_1)} & \text{for} \quad \tau_1 \le \tau \le \tau_2 \\ 0 & \text{otherwise} \end{cases} \tag{2.6}$$

The corresponding magnetic susceptibility is obtained by substituting Eq. (2.6) into Eq. (2.5), and solving the resulting integral (Dabas et al., 1992; Pasion, 2007):

$$\chi(\omega) = \chi_\infty + \frac{\Delta\chi}{ln(\tau_2/\tau_1)} \int_{\tau_1}^{\tau_2} \frac{1}{\tau(1+i\omega\tau)} d\tau \tag{2.7}$$

$$= \chi_\infty + \Delta\chi \left[1 - \frac{1}{ln(\tau_2/\tau_1)} ln\left(\frac{1+i\omega\tau_2}{1+i\omega\tau_1} \right) \right] \tag{2.8}$$

Eq. (2.8) has the same zero and infinite frequency limits as the Debye model in Eq. (2.3). For frequencies $1/\tau_2 \ll \omega/2\pi \ll 1/\tau_1$, in-phase magnetic susceptibility decreases linearly as function of $ln(\omega)$, whereas the imaginary component will remain more or less constant (Mullins and Tite, 1973; Dabas et al., 1992):

$$\frac{\partial Re[\chi(\omega)]}{\partial\, ln(\omega)} \approx \frac{2}{\pi} Im[\chi(\omega)] \approx -\frac{\Delta\chi}{ln(\tau_2/\tau_1)} \tag{2.9}$$

According to Eq. (2.8), the magnetic permeability characterizing the majority of soil samples is:

$$\mu(\omega) = \mu_0\big[1+\chi(\omega)\big] = \mu_0 \left[1 + \chi_\infty + \Delta\chi - \frac{\Delta\chi}{ln(\tau_2/\tau_1)} ln\left(\frac{1+i\omega\tau_2}{1+i\omega\tau_1} \right) \right] \tag{2.10}$$

where $\mu(\omega)$ is the frequency dependent magnetic permeability, and $\mu_0 = 4\pi \times 10^{-7}$ N/A^2 is the permeability of free-space. Eq. (2.10) suggests that near the low and high frequency limits, the applied magnetic field and

total magnetic flux density are approximately in phase. For frequencies $1/\tau_2 \ll \omega/2\pi \ll 1/\tau_1$ however, the total magnetic flux density lags the applied magnetic field.

Occasionally, the magnetic viscosity exhibited by iron-bearing soil samples cannot be fit accurately using Eq. (2.8). In this case, a better fit may be obtained by choosing a weighting function which defines a log-normal distribution of time-relaxation constants (Pasion, 2007). The weighting function $g(\tau)$ for a log-normal distribution is:

$$g(\tau) = \frac{1}{\tau\beta\sqrt{2\pi}}\, e^{-(ln\,\tau - ln\,\tau_c)^2/2\beta^2} \tag{2.11}$$

where β and τ_c are parameters which define the shape of the distribution. A more comprehensive definition of β and τ can be found in Appendix A. Others have represented the frequency dependent magnetic susceptibility using a Cole-Cole model (Olhoeft and Strangway, 1974; Dabas et al., 1992; Pasion, 2007), where:

$$\chi(\omega) = \chi_\infty + \frac{\Delta\chi}{1 + (i\omega\tau_c)^\alpha} \tag{2.12}$$

The distribution of time relaxation constants representing the Cole-Cole model, is centered at τ_c. $\alpha \in [0,1]$ scales the distribution of time relaxation constants. For $\alpha = 1$, Eq. (2.12) is identical to the Debye model. A comparison between the Debye model, Cole-Cole model, log-normal distribution and log-uniform distribution is shown in Figure 2.1.

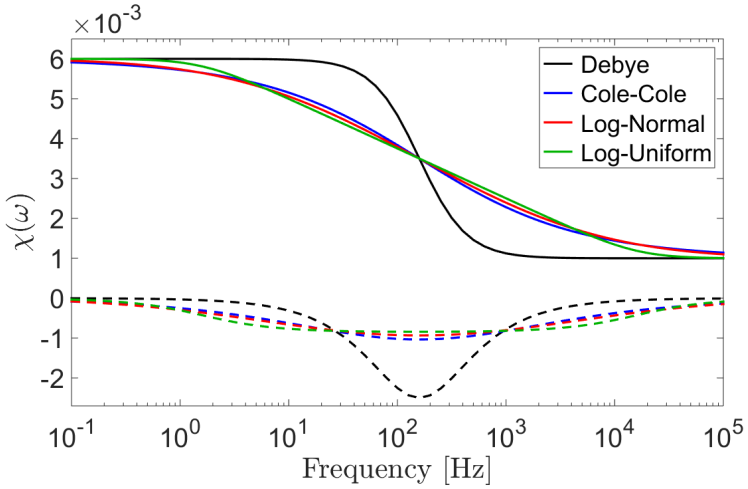

Figure 2.1: In-phase and quadrature magnetic susceptibility for various models, with $\chi_\infty = 0.001$ and $\Delta\chi = 0.005$. Additional parameters: $\tau = 10^{-3}$ s for Debye model, $\tau_c = 10^{-3}$ s and $\alpha = 0.5$ for the Cole-Cole model, $\tau_c = 10^{-3}$ s and $\beta = 3$ for the log-normal distribution, and $\tau_1 = 10^{-5}$ s and $\tau_2 = 0.1$ s for the log-uniform distribution.

2.3.2 Impulse Response Function for the Time-Dependent Magnetization of Iron-Bearing Soils

When exposed to a time-varying magnetic field, iron-bearing soils experience a corresponding alteration in magnetization. For magnetically viscous soils, a portion of the induced magnetization does not adjust instantaneously to changes in the applied field. This portion is attributed to the magnetization exhibited by SP iron-oxide grains. In the frequency domain, magnetization $\vec{M}(\omega)$ is the product of a material's magnetic susceptibility $\chi(\omega)$ and the applied magnetic field $\vec{H}(\omega)$:

$$\vec{M}(\omega) = \chi(\omega)\vec{H}(\omega) \tag{2.13}$$

In the time domain, this relationship becomes a convolution. The convolution can be obtained by performing an inverse Fourier transform on Eq. (2.13):

$$\vec{M}(t) = \chi(t) \otimes \vec{h}(t) = \int_{-\infty}^{\infty} \chi(\xi)\vec{h}(t-\xi)d\xi \tag{2.14}$$

where $\vec{M}(t)$ is the induced magnetization, $\vec{h}(t)$ is the applied magnetic field, and $\chi(t)$ represents the magnetization's impulse response. A system's impulse response is the inverse Fourier transform of its frequency response. The frequency dependent magnetic susceptibility $\chi(\omega)$ is therefore:

$$\chi(t) = \frac{1}{2\pi}\int_{-\infty}^{\infty} \chi(\omega)e^{i\omega t}d\omega \tag{2.15}$$

For a theoretical sample whose magnetic susceptibility is defined by the Debye model, $\chi(t)$ can be obtained by substituting Eq. (2.3) into Eq. (2.15):

$$\chi(t) = \chi_\infty \delta(t) + \frac{\Delta\chi}{\tau}e^{-t/\tau}u(t) \tag{2.16}$$

where $u(t)$ is the unit step function, and $\delta(t)$ is the Dirac delta function. In the case where SP grains within the sample are characterized by a distribution of time-relaxation constants, I must introduce a weighting function $f(\tau)$. By Multiplying the decaying term in Eq. (2.16) by the weighting function, and integrating over all time-relaxation constants:

$$\chi(t) = \chi_\infty \delta(t) + \Delta\chi u(t)\int_0^{\infty} f(\tau)\frac{e^{-t/\tau}}{\tau}d\tau \tag{2.17}$$

For a log-uniform distribution of time-relaxation constants, $f(\tau)$ is defined according to Eq. (2.6). By substituting Eq. (2.6) into Eq. (2.17), and evaluating the resulting integral:

$$\chi(t) = \chi_\infty \delta(t) + \frac{\Delta\chi u(t)}{ln(\tau_2/\tau_1)}\int_{\tau_1}^{\tau_2}\frac{e^{-t/\tau}}{\tau^2}d\tau \tag{2.18}$$

$$= \chi_\infty \delta(t) + \frac{\Delta\chi}{ln(\tau_2/\tau_1)}\left[\frac{e^{-t/\tau_2} - e^{-t/\tau_1}}{t}\right]u(t) \tag{2.19}$$

According to Eq. (2.19), the impulse response function characterizing iron-bearing soils is comprised of two terms: a delta function scaled by the infinite magnetic susceptibility (χ_∞), and a positive, monotonic decreasing function defined for $t > 0$. The general shape of the impulse response is shown in Figure 2.19. It should also be noted that Eq. (2.19) can be obtained by substituting Eq. (2.8) directly into Eq. (2.15).

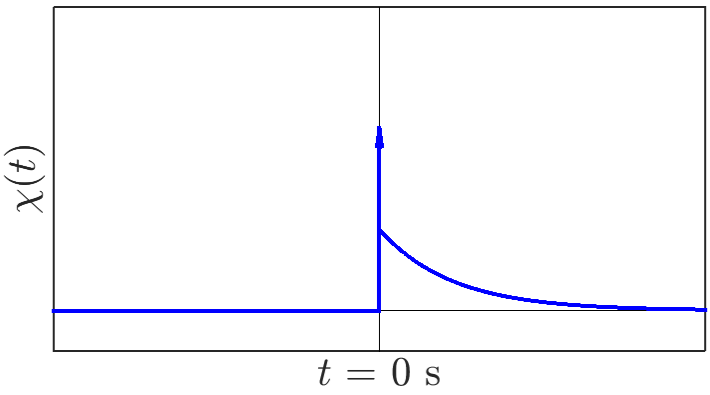

Figure 2.2: General shape of the impulse response defined by Eq. (2.19).

2.3.3 Response to Step Excitation

Consider the magnetization which results from a step-on excitation. In this case, the applied magnetic field $\vec{h}(t)$ takes the form:

$$h(t) = \vec{H}_0 u(t) \tag{2.20}$$

where $\vec{H}_0$ is the amplitude of an external magnetic field after it is applied, and $u(t)$ is the unit step function. For a sample which can be characterized using the Debye model, the magnetization $\vec{M}(t)$ can be determined by substituting Eqs. (2.16) and (2.20) into Eq. (2.14):

$$\vec{M}(t) = \vec{H}_0 \int_{-\infty}^{\infty} \chi(\xi) u(t-\xi) d\xi \tag{2.21}$$

$$= \begin{cases} 0 & \text{for } t < 0 \\ \vec{H}_0 \left[\chi_\infty + \Delta\chi \left(1 - e^{-t/\tau}\right) \right] & \text{for } t \geq 0 \end{cases} \tag{2.22}$$

Eq. (2.22) states that before the field is applied, the magnetization is zero. Upon application of the external field at $t = 0$, an instantaneous magnetization occurs within the sample. This magnetization is equal to $\chi_\infty \vec{H}_0$. For $t > 0$, the magnetic viscosity exhibited by SP grains results in a gradual increase in magnetization over time. The final magnetization experienced by the sample as $t \to \infty$ is $\left(\chi_\infty + \Delta\chi\right)\vec{H}_0$, and represents a magnetic equilibrium.

Similarly for step-off excitation:

$$\vec{M}(t) = \vec{H}_0 \int_{-\infty}^{\infty} \chi(\xi) u(\xi - t) d\xi \tag{2.23}$$

$$= \begin{cases} (\chi_\infty + \Delta\chi)\vec{H}_0 & \text{for } t < 0 \\ \Delta\chi \vec{H}_0 e^{-t/\tau} & \text{for } t \geq 0 \end{cases} \tag{2.24}$$

In this case, the sample exhibits an initial magnetization of $(\chi_\infty + \Delta\chi)\vec{H}_0$ for $t < 0$. At $t = 0$, the external magnetic field is removed and the sample experiences an instantaneous decrease in magnetization. This initial loss in magnetization is equal to $\chi_\infty \vec{H}_0$. For $t > 0$, the sample experiences an exponential decrease in magnetization. The exponential rate of decay depends on the time relaxation constant for SP grains within the sample.

The magnetic viscosity in iron-bearing soils is commonly represented by an after-effect function $F(t)$, which decays as a function of time (Néel, 1949; Moskowitz, 1985; Dabas et al., 1992; Pasion, 2007). For a step-on excitation, the magnetization of any sample can be expressed as:

$$\vec{M}(t) = \begin{cases} 0 & \text{for } t < 0 \\ \vec{H}_0 \left[\chi_\infty + \Delta\chi \left(1 - F(t) \right) \right] & \text{for } t \geq 0 \end{cases} \tag{2.25}$$

And for step-off excitation:

$$\vec{M}(t) = \begin{cases} (\chi_\infty + \Delta\chi)\vec{H}_0 & \text{for } t < 0 \\ \Delta\chi \vec{H}_0 F(t) & \text{for } t \geq 0 \end{cases} \tag{2.26}$$

The distribution of time relaxation constants characterizing a soil sample, also defines its after-effect function. Using a weighting function $f(\tau)$, the after-effect function can be expressed as (Néel, 1949; Pasion, 2007):

$$F(t) = \int_0^{\infty} f(\tau) e^{-t/\tau} d\tau \tag{2.27}$$

For a log-uniform distribution of time-relaxation constants, Eq. (2.6) may be substituted into Eq. (2.27) to obtain an after-effect function of the form:

$$F(t) = \frac{1}{ln(\tau_2/\tau_1)} \int_{\tau_1}^{\tau_2} \frac{1}{\tau} e^{-t/\tau} d\tau$$

$$= \frac{1}{ln(\tau_2/\tau_1)} \left[Ei\left(\frac{t}{\tau_2}\right) - Ei\left(\frac{t}{\tau_1}\right) \right] \tag{2.28}$$

where Ei is the exponential integral function. For observations at time $\tau_1 \ll t \ll \tau_2$, $Ei(t/\tau_1) \approx 0$ and $Ei(t/\tau_2) \approx -\gamma - ln(t/\tau_2)$; where $\gamma \approx 0.5772$ is the Euler constant (Pasion, 2007). Over this time period, the after-effect function can be approximated by:

$$F(t) \approx \bar{F}(t) = \frac{1}{ln(\tau_2/\tau_1)} \left[-\gamma - ln(t) + ln(\tau_2) \right] \tag{2.29}$$

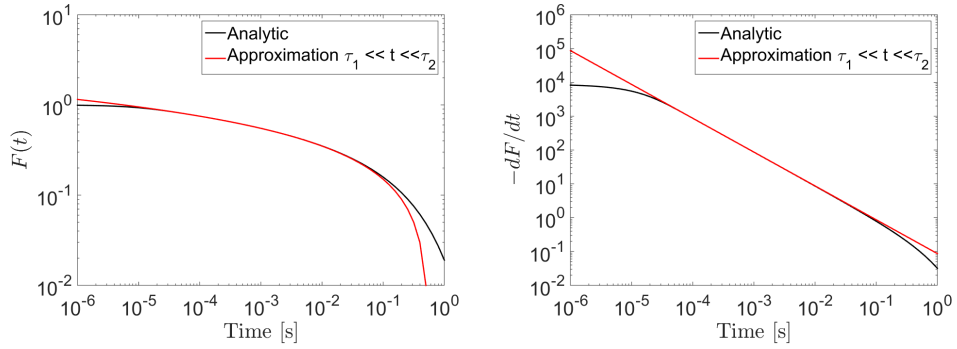

Figure 2.3: After-effect function for SP grains characterized by a log-uniform distribution of time-relaxation constants between $\tau_1 = 10^{-5}$ s and $\tau_2 = 1$ s. (a) After-effect function due unit step-off excitation. (b) Rate of decay in response to step-off excitation.

Expression (2.29) shows that magnetization within a collection of SP grains, in response to a step-off excitation, is proportional to ln(t) for $\tau_1 \ll t \ll \tau_2$. A comparison between $F(t)$ and $\bar{F}(t)$ for $\tau_1 = 10^{-5}$ s and $\tau_2 = 1$ s can be seen in Figure 2.3a. The rate of decay can be obtained by taking the time derivative of Eq. (2.28), and solving the resulting integral:

$$\begin{aligned} \frac{dF(t)}{dt} &= \frac{1}{ln(\tau_2/\tau_1)} \int_{\tau_1}^{\tau_2} -\frac{1}{\tau^2} e^{-t/\tau} d\tau \\ &= \frac{1}{ln(\tau_2/\tau_1)} \left[\frac{e^{-t/\tau_1} - e^{-t/\tau_2}}{t} \right] \end{aligned} \tag{2.30}$$

At time $\tau_1 \ll t \ll \tau_2$, Eq. (2.30) can be approximated by the following expression:

$$\frac{dF(t)}{dt} \approx \frac{d\bar{F}(t)}{dt} = -\frac{1}{ln(\tau_2/\tau_1)} \frac{1}{t} \tag{2.31}$$

Therefore, the rate of decay in response to a step-off excitation, is proportional to $1/t$ for $\tau_1 \ll t \ll \tau_2$. A comparison between dF/dt and $d\bar{F}/dt$ for a unit step-off with $\tau_1 = 10^{-5}$ s and $\tau_2 = 1$ s can be seen in Figure 2.3b.

Magnetization proportional to $ln(t)$, and decay proportional to $1/t$, have been observed in a variety of settings. Field examples can be found in: Buselli (1982), Barsukov and Fainbert (2001), and Pasion (2007). Notable laboratory experiments are summarized in Néel (1949), Dabas (et al., 1992), and Dabas and Skinner (1993).

2.3.4 Square-Pulse Response

For many time-domain EM systems, the primary field is generated by a square-pulse current waveform. Here, I present a derivation for the time-dependent magnetization of iron-bearing soils, in response to square-pulse excitation. I will assume the magnetic viscosity of the soil is characterized using a log-uniform distribution of

time relaxation constants. For a square-pulse excitation initially applied at $t = -\Delta t$, and removed at $t = 0$ (giving it a width of Δt), the external magnetic field $\vec{h}_p(t)$ is given by:

$$\vec{h}_p(t) = \vec{H}_0\Big[u(t+\Delta t) - u(t)\Big] \tag{2.32}$$

where $\vec{H}_0$ is the applied field during the on-time. Using Eqs. (2.14), (2.19) and (2.32), the magnetization $\vec{M}(t)$ can be expressed as:

$$\vec{M}(t) = \int_{-\infty}^{\infty} \chi(\xi)\,\vec{h}_p(t-\xi)d\xi \tag{2.33}$$

$$= \chi_\infty \vec{h}_p(t) + \frac{\Delta\chi\vec{H}_0}{ln(\tau_2/\tau_1)}\int_t^{t+\Delta t} \frac{e^{-\xi/\tau_2} - e^{-\xi/\tau_1}}{\xi} d\xi \tag{2.34}$$

$$= \chi_\infty \vec{H}_0\Big[u(t+\Delta t) - u(t)\Big] + \frac{\Delta\chi\vec{H}_0}{ln(\tau_2/\tau_1)}\left[E_i\left(\frac{t}{\tau_2}\right) - E_i\left(\frac{t}{\tau_1}\right) - E_i\left(\frac{t+\Delta t}{\tau_2}\right) + E_i\left(\frac{t+\Delta t}{\tau_1}\right)\right] \tag{2.35}$$

where $E_i(x)$ is the exponential integral function. I can see from Eq. (2.35), that as $\Delta t \to 0$, $\vec{M}(t) = 0$ at all times. I can also show that as $\Delta t \to \infty$, Eq. (2.35) behaves according to a step-off excitation. The time-dependent derivative of the magnetization can be obtained by taking the derivative of Eq. (2.33), and substituting Eqs. (2.19) and (2.32):

$$\frac{d\vec{M}(t)}{dt} = \int_{-\infty}^{\infty} \chi(\xi)\,\frac{\partial}{\partial t}\vec{h}_p(t-\xi)d\xi \tag{2.36}$$

$$= \chi_\infty \vec{H}_0\Big[\delta(t+\Delta t) - \delta(t)\Big] + \Delta\chi\vec{H}_0\int_{-\infty}^{\infty} \frac{e^{-\xi/\tau_2} - e^{-\xi/\tau_1}}{\xi}\Big[\delta(t+\Delta t-\xi) - \delta(t-\xi)\Big]d\xi \tag{2.37}$$

$$= \chi_\infty \vec{H}_0\Big[\delta(t+\Delta t) - \delta(t)\Big] + \frac{\Delta\chi\vec{H}_0}{ln(\tau_2/\tau_1)}\left[\frac{e^{-(t+\Delta t)/\tau_2} - e^{-(t+\Delta t)/\tau_1}}{t+\Delta t} - \frac{e^{-t/\tau_2} - e^{-t/\tau_1}}{t}\right] \tag{2.38}$$

We can see from Eq. (2.38), that as $\Delta t \to 0$, $d\vec{M}(t)/dt = 0$ at all times; which makes sense given that no magnetization is experienced by the sample. In addition, I can also show that as $t \to \infty$, Eq. (2.38) exhibits a rate of decay which is identical to that of a step-off excitation.

For square-pulse excitation, we may choose to represent the magnetic relaxation at $t > 0$ using an after-effect function. According Eq. (2.35):

$$F(t) = \frac{1}{ln(\tau_2/\tau_1)}\left[E_i\left(\frac{t}{\tau_2}\right) - E_i\left(\frac{t}{\tau_1}\right) - E_i\left(\frac{t+\Delta t}{\tau_2}\right) + E_i\left(\frac{t+\Delta t}{\tau_1}\right)\right] \tag{2.39}$$

where

$$\vec{M}(t>0) = \Delta\chi\,\vec{H}_0 F(t) \tag{2.40}$$

The magnetic relaxation process takes longer in SP grains characterized by larger time relaxation constants. As a result, these grains cannot reach a magnetic equilibrium during the on-time if the pulse width is too short. The magnetization of a sample for step-off excitation and for various pulse widths are shown in Figure 2.4a.

For observations made at $\tau_1 \ll t \ll \tau_2$, $E_i(t/\tau_1) \approx 0$ and $E_i(t/\tau_2) \approx -\gamma - ln(t/\tau_2)$; where $\gamma \approx 0.5772$ is the Euler constant. If the width of the pulse is sufficiently short (i.e. $\Delta t \ll \tau_2$), then for $\tau_1 \ll t \ll \tau_2$, the after-effect function is approximately equal to:

$$F(t) \approx \bar{F}(t) = \frac{1}{ln(\tau_2/\tau_1)} ln\left(1 + \frac{\Delta t}{t}\right) \tag{2.41}$$

Using Eq. (2.38), the time-dependent derivative of the after-effect function can be expressed as:

$$\frac{dF(t)}{dt} = \frac{1}{ln(\tau_2/\tau_1)} \left[\frac{e^{-(t+\Delta t)/\tau_2} - e^{-(t+\Delta t)/\tau_1}}{t+\Delta t} - \frac{e^{-t/\tau_2} - e^{-t/\tau_1}}{t} \right] \tag{2.42}$$

At early times, SP grains characterized by small time-relaxation constants dominate the magnetic relaxation of the sample. As a result, the rate of decay for both step-off excitation and a square-pulse waveform are approximately identical over early times. After sufficient time however, the rate of decay in response to a square-pulse waveform becomes steeper, eventually approaching a rate proportional to $1/t^2$ (Billings et al., 2003). dF/dt for step-off excitation and for several pulse widths are compared in Figure 2.4b. For observations made at $\tau_1 \ll t \ll \tau_2$, $e^{-t/\tau_1} \approx 0$ and $e^{-t/\tau_2} \approx 1$. If the width of the pulse is sufficiently short (i.e. $\Delta t \ll \tau_2$), then for $\tau_1 \ll t \ll \tau_2$, Eq. (2.42) is approximately equal to:

$$\frac{dF(t)}{dt} \approx \frac{d\bar{F}(t)}{dt} = -\frac{1}{ln(\tau_2/\tau_1)} \left[\frac{1}{t} - \frac{1}{t+\Delta t} \right] \tag{2.43}$$

Ultimately, Eqs. (2.39), (2.41), (2.42) and (2.43) state that characteristic magnetic responses from iron-bearing soils are dependent on: the physical properties of the soil, the width of the square-pulse, and the time of observation.

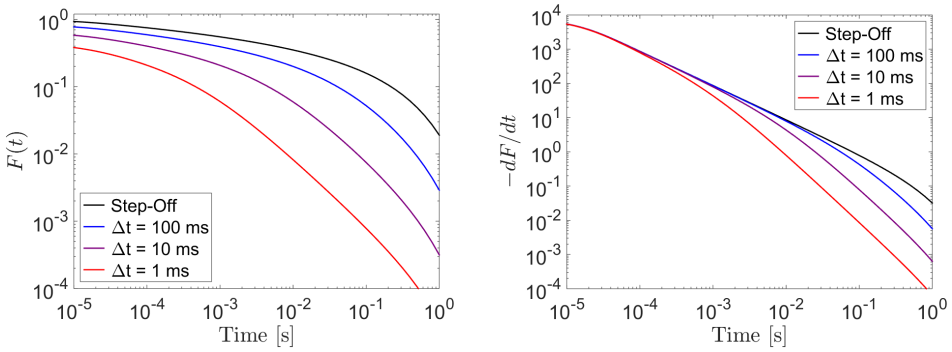

(a) **(b)**

Figure 2.4: After-effect function for SP grains characterized by a log-normal distribution of time-relaxation constants between $\tau_1 = 10^{-5}$ s and $\tau_2 = 1$ s. (a) Square-pulse after-effect functions for $\Delta t = 1$ ms, 10 ms and 100 ms, compared to a step-off excitation. (b) Square-pulse rate of decay for $\Delta t = 1$ ms, 10 ms and 100 ms, compared to a step-off excitation.

2.3.5 Arbitrary Waveform Response

For a given time-domain EM system, the primary field may be generated by an arbitrary current waveform. Here, the inducing field is approximated by a finite set of square pulse excitations. Using this approximation, analytic expressions are derived for predicting the time-dependent magnetization induced in iron-bearing soils. Once again, I will assume the soil's magnetic viscosity is characterized by a log-uniform distribution of time-relaxation constants.

Consider an inducing field $\vec{h}(t)$, which is only non-zero over times $-\lambda \leq t \leq 0$. Using a finite set of square-pulse functions with varying amplitudes, I approximate the inducing magnetic field as follows:

$$\vec{h}(t) \approx \vec{h}_a(t) = \sum_{\ell=1}^{L} \vec{h}\Big(\big[1/2-\ell\,\big]\Delta t\Big)\Big[u\Big(t+\ell\Delta t\Big) - u\Big(t+\big[\ell-1\big]\Delta t\Big)\Big] \tag{2.44}$$

where $\vec{h}_a(t)$ represents the approximation, $u(t)$ is the unit step function, L is the number of discrete square-pulses, and $\Delta t = \lambda/L$ is the width of each square pulse. An example of this is illustrated in Figure 2.5. In addition, the inducing field's time-dependent derivative is approximated by:

$$\frac{\partial \vec{h}(t)}{\partial t} \approx \frac{\partial \vec{h}_a(t)}{\partial t} = \sum_{\ell=1}^{L} \vec{h}\Big(\big[1/2-\ell\,\big]\Delta t\Big)\Big[\delta\Big(t+\ell\Delta t\Big) - \delta\Big(t+\big[\ell-1\big]\Delta t\Big)\Big] \tag{2.45}$$

where $\delta(t)$ is the Dirac delta function. Using Eq. (2.19) and the results from the convolution performed in Eq. (2.35), the magnetization of the soil as a function of time may be approximated as:

$$\vec{M}(t) \approx \int_{-\infty}^{\infty} \chi(\xi)\vec{h}_a(t-\xi)d\xi \tag{2.46}$$

$$\approx \chi_\infty \vec{h}(t) + \frac{\Delta\chi}{ln(\tau_2/\tau_1)} \sum_{\ell=1}^{L} \vec{h}\Big(\big[1/2-\ell\,\big]\Delta t\Big) \ldots \tag{2.47}$$

$$\left[E_i\left(\frac{t+(\ell-1)\Delta t}{\tau_2}\right) - E_i\left(\frac{t+(\ell-1)\Delta t}{\tau_1}\right) - E_i\left(\frac{t+\ell\Delta t}{\tau_2}\right) + E_i\left(\frac{t+\ell\Delta t}{\tau_1}\right)\right]$$

where $E_i(x)$ is the exponential integral function. Likewise, Eq. (2.19 and the convolution performed in Eq. (2.38) can be used to approximate the time-dependent derivative of the induced magnetization:

$$\frac{d\vec{M}(t)}{dt} \approx \int_{-\infty}^{\infty} \chi(\xi)\,\frac{\partial}{\partial t}\vec{h}_a(t-\xi)d\xi \tag{2.48}$$

$$\approx \chi_\infty \frac{\partial \vec{h}_a(t)}{\partial t} + \frac{\Delta\chi}{ln(\tau_2/\tau_1)} \sum_{\ell=1}^{L} \vec{h}\Big(\big[1/2-\ell\,\big]\Delta t\Big) \ldots \tag{2.49}$$

$$\left[\frac{e^{-(t+\ell\Delta t)/\tau_2} - e^{-(t+\ell\Delta t)/\tau_1}}{t+\ell\Delta t} - \frac{e^{-\Big((t+(\ell-1)\Delta t\Big)/\tau_2} - e^{-\Big(t+(\ell-1)\Delta t\Big)/\tau_1}}{t+(\ell-1)\Delta t}\right]$$

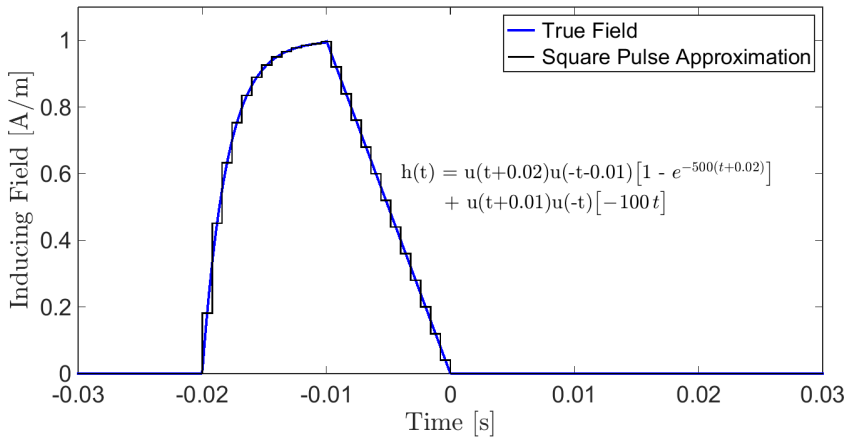

Figure 2.5: Approximation of the true inducing field using a finite set of square-pulse excitations. In this case, $\lambda = 0.02$ s, $L = 25$, and $\Delta t = 8\times10^{-4}$ s.

As previously shown in Sections 2.3.3 and 2.3.4, the viscous remanent magnetization at $t > 0$ can be expressed using an after-effect function $F(t)$, such that:

$$\vec{M}(t>0) = \Delta\chi\,\vec{H}_{max}\,F(t) \tag{2.50}$$

where $\Delta\chi$ is the zero-frequency magnetic susceptibility of all SP grains, and $\vec{H}_{max}$ is the value of the inducing field at its maximum amplitude. Before presenting an expression for the after-effect function, I first define the following function $g(t)$, where:

$$g(t) = \frac{h(t)}{H_{max}} = \frac{I(t)}{I_{max}} \tag{2.51}$$

Thus, $g(t)$ represents a ratio between the amplitude of the inducing field at time t, and the maximum amplitude of the inducing field. However, if the inducing field is generated by an inductive source, the Biot-Savart law may be used to represent $g(t)$ as the ratio between the transmitter's current at time t and the maximum current amplitude. From Eqs. (2.47). (2.50) and (2.51), the after-effect function for an arbitrary inducing field is approximated by:

$$\begin{aligned} F(t) \approx \frac{1}{ln(\tau_2/\tau_1)} \sum_{\ell=1}^{L} g\Big(\big[1/2-\ell\,\big]\Delta t\Big)\ldots \\ \left[E_i\left(\frac{t+(\ell-1)\Delta t}{\tau_2}\right) - E_i\left(\frac{t+(\ell-1)\Delta t}{\tau_1}\right) - E_i\left(\frac{t+\ell\Delta t}{\tau_2}\right) + E_i\left(\frac{t+\ell\Delta t}{\tau_1}\right)\right] \end{aligned} \tag{2.52}$$

For observations made at $\tau_1 \ll t \ll \tau_2$, $E_i(t/\tau_1) \approx 0$ and $E_i(t/\tau_2) \approx -\gamma - ln(t/\tau_2)$; where $\gamma \approx 0.5772$ is the Euler constant. If the total width of the waveform is sufficiently short (i.e. $\lambda \ll \tau_2$), and given that $\ell\Delta t < \lambda \;\forall\; \ell$, the after-effect function at $\tau_1 \ll t \ll \tau_2$ is approximately equal to:

$$F(t) \approx \bar{F}(t) = \frac{1}{ln(\tau_2/\tau_1)} \sum_{\ell=1}^{L} g\Big(\big[1/2-\ell\,\big]\Delta t\Big)\, ln\left(1+\frac{\Delta t}{t+(\ell-1)\Delta t}\right) \tag{2.53}$$

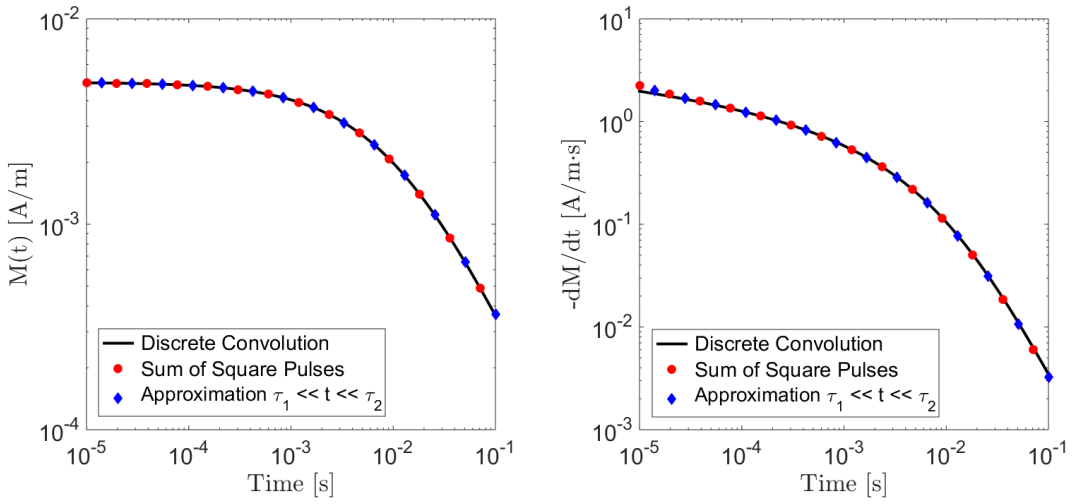

(a) **(b)**

Figure 2.6: Comparison between the discrete convolution, analytic approximation and $\tau_1 \ll t \ll \tau_2$ approximation for predicting the viscous remanent magnetization in iron-bearing soils. The inducing field is illustrated in Figure 2.5. Physical properties were given by $\Delta\chi = 0.05$, $\tau_1 = 10^{-6}$ s and $\tau_2 = 10$ s. (a) Time-dependent induced magnetization. (b) Time-dependent rate of decay.

Similarly from Eqs. (2.49). (2.50) and (2.51), the time-dependent derivative for the after-effect function is approximated by:

$$\frac{dF(t)}{dt} \approx \frac{1}{ln(\tau_2/\tau_1)} \sum_{\ell=1}^{L} g\Big(\big[1/2-\ell\big]\Delta t\Big) \ldots \left[\frac{e^{-(t+\ell\Delta t)/\tau_2} - e^{-(t+\ell\Delta t)/\tau_1}}{t+\ell\Delta t} - \frac{e^{-\left((t+(\ell-1)\Delta t\right)/\tau_2} - e^{-\left(t+(\ell-1)\Delta t\right)/\tau_1}}{t+(\ell-1)\Delta t}\right] \tag{2.54}$$

For observations made at $\tau_1 \ll t \ll \tau_2$, $E_i(t/\tau_1) \approx 0$ and $E_i(t/\tau_2) \approx -\gamma - ln(t/\tau_2)$; where $\gamma \approx 0.5772$ is the Euler constant. If the total width of the waveform is sufficiently short (i.e. $\lambda \ll \tau_2$), and given that $\ell\Delta t < \lambda \ \forall \ \ell$, the time-dependent derivative at $\tau_1 \ll t \ll \tau_2$ is approximately equal to:

$$\frac{dF(t)}{dt} \approx \frac{d\bar{F}(t)}{dt} = -\frac{1}{ln(\tau_2/\tau_1)} \sum_{\ell=1}^{L} g\Big(\big[1/2-\ell\big]\Delta t\Big) \left[\frac{1}{t+(\ell-1)\Delta t} - \frac{1}{t+\ell\Delta t}\right] \tag{2.55}$$

To verify the approximation of the soil's VRM response, I considered the inducing field shown in Figure 2.5. Physical properties for the soil were given by $\chi_\infty = 0$, $\Delta\chi = 0.05$, $\tau_1 = 10^{-6}$ s and $\tau_2 = 10$ s. Discrete convolutions were evaluated according to Eq. (2.14) and its derivative. The impulse response $\chi(t)$, analytic inducing field $h(t)$ and its time-dependent derivative $\partial h(t)/\partial t$ were discretized using a time-spacing of 2×10^{-7} s. For $L = 500$ discrete square pulses, Eqs. (2.50), (2.51), (2.52) and (2.54) were used to approximate the induced magnetization and its time-dependent derivative at $t > 0$. And for $L = 500$ discrete square pulses, Eqs. (2.50), (2.51), (2.53) and (2.55) were used to approximate the induced magnetization and its time-dependent derivative

at $t > 0$. Comparison between the convolution, analytic approximation, and approximation for $\tau_1 \ll t \ll \tau_2$ are shown in Figure 2.6. Results indicate that the approximation of the induced magnetization is very accurate so long as a sufficient number of square pulses are used. The number of square pulses required depends on how smooth the true current waveform and its time-dependent derivative are with respect to time.

2.4 Obtaining the Magnetic Properties of Iron-Bearing Soils

Several models have been used to explain the frequency dependent magnetic susceptibilities which characterize iron-bearing soils (Olhoeft and Strangway, 1974; Dabas et al., 1992; Pasion, 2007). The parameters defining each model represent a distinct set of properties for the soil. These properties may be physical or purely mathematical. The model parameters which fit a sample's magnetic viscosity are diagnostic, as they depend on the sample's mineralogy and weathering history. Here, I present a set of physical properties for iron-bearing soils. These physical properties are then related to mathematical models which characterize the soil's magnetic viscosity.

When exposed to a magnetostatic field, the magnetization of an iron-bearing soil is defined by its zero-frequency magnetic susceptibility. According to Eq. (2.8), this is equivalent to $\chi(\omega \to 0) = \chi_\infty + \Delta\chi$. The zero-frequency magnetic susceptibilities for iron-bearing rock types are shown in Figure 2.7a. Values are given in SI units; SI units are equivalent to units of [A/m]/[A/m]. The majority of laterites have zero-frequency magnetic susceptibilities between 10^{-4} SI and 5×10^{-2} SI, depending on the distinct mineralogy of each soil. Because their zero-frequency magnetic susceptibilities are quite small ($\chi_\infty + \Delta\chi \leq 0.05$), the magnetic properties of lateritic soils do not significantly impact the inductive response (van Dam et al., 2004, 2005; Druyts et al., 2009).

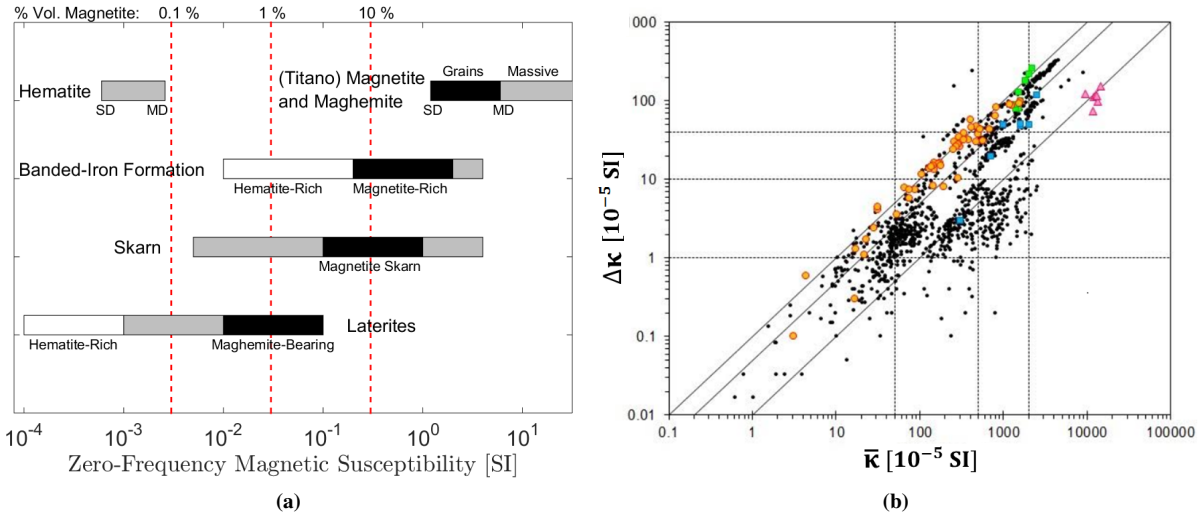

Figure 2.7: (a) Zero-frequency magnetic susceptibilities for various rock types, including laterites (Adapted from Clark and Emerson, 1991). Black and white boxes are used to denote ranges for rocks classified by more detailed mineralogies. (b) Cross plot showing the absolute magnetic susceptibility at 958 Hz ($\bar{\kappa}$), versus the difference in dual-frequency susceptibility measurements between 465 Hz and 4,650 Hz ($\Delta\kappa$). Figure taken from van Dam (et al., 2008). Black markers are used to denote samples collected in the United States, Panama and Honduras. Coloured markers are used to represent samples collected within the Sepon Mineral District, Laos.

Category (Billings et al., 2003)	$\bar{\kappa}$ [10^{-5} SI] (958 Hz)	$\Delta\kappa$ [10^{-5} SI] (465 to 4,650 Hz)
Neutral	$<$50	$<$1
Moderate	50-500	1-10
Severe	500-2000	10-40
Very Severe	$>$2000	$>$40

Table 2.1: Impact of magnetic viscosity on inductive sensors, according to dual-frequency measurements (Billings et al., 2003).

Furthermore, this implies that lateritic soils do not exhibit demagnetizing effects (Lelièvre and Oldenburg, 2006; Krahenbuhl and Li, 2007; Austin et al., 2014).

Parameters defining the frequency-dependent magnetic susceptibility are not easily determined. Infinite frequency susceptibilities cannot be directly measured, as EM induction will dominate the sample's response. Dabas (et al., 1992) measured the susceptibility over a range of frequencies, and fit the data using a Cole-Cole model. However, this experiment is both time-consuming and expensive. Dual-frequency measurements are commonly used to characterize the magnetic viscosity exhibited by lateritic soils. Using a Barington MS2B dual-frequency sensor (Dearing et al., 1996; van Dam et al., 2008), the absolute magnetic susceptibility of a sample is measured at two frequencies (465 Hz and 4,650 Hz). The absolute magnetic susceptibility is defined by:

$$\kappa(\omega) = \left|\chi(\omega)\right| \tag{2.56}$$

Dual-frequency measurements at 465 Hz and 4,650 Hz can be used to calculate the sample's absolute magnetic susceptibility at 958 Hz, using the method from Dearing (et al., 1996). The absolute magnetic susceptibility at 958 Hz will be denoted by $\bar{\kappa}$. The absolute difference between high and low frequency measurements is denoted by $\Delta\kappa$. A database containing dual-frequency measurements on a total of 1,027 samples, from tropical to semi-arid regions, currently exists (van Dam et al., 2008). A cross-plot of $\bar{\kappa}$ versus $\Delta\kappa$ for these soils is shown in Figure 2.7b. According to the database: 1) $\bar{\kappa}$ and $\Delta\kappa$ are positively correlated, 2) both $\bar{\kappa}$ and $\Delta\kappa$ increase with respect to soil maturity, and 3) $\Delta\kappa < 0.1\bar{\kappa}$ for nearly all samples. Dual-frequency measurements have been used to classify a soil's impact on inductive source transmitters (Billings et al., 2003). This classification scheme is illustrated in Table 2.1. If characterized by sufficiently large values of $\bar{\kappa}$ and $\Delta\kappa$, iron-bearing soils are capable of generating magnetic fields which can mask the responses from unexploded ordnance and buried conductors (Buselli, 1982; Barsukov and Fainberg, 2001; Billings et al., 2003; Pasion, 2007; Zadorozhnaya et al., 2012). Dual-frequency susceptibility measurements are therefore quite useful. However, they cannot be directly used to recover parameters which define the magnetic susceptibility models I have presented.

Now consider a sample whose frequency-dependent magnetic susceptibility is defined by a log-uniform distribution of time-relaxation constants. According to Eq. (2.9), quadrature susceptibility is much smaller than in-phase susceptibility if: 1) χ_∞ is sufficiently large in comparison to $\Delta\chi$, or 2) the distribution of time-relaxation

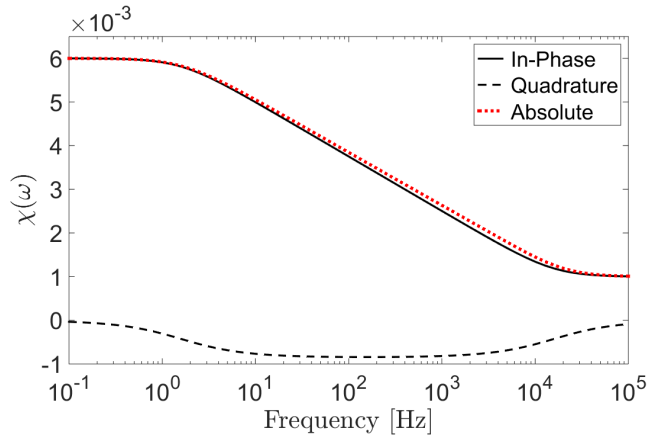

Figure 2.8: Real, quadrature and absolute magnetic susceptibility for a sample defined by Eq. (2.8), using properties: $\chi_\infty = 0.001$, $\Delta\chi = 0.005$, $\tau_1 = 10^{-5}$ s, and $\tau_2 = 10^{-1}$ s.

constants is sufficiently broad. For the majority of soil samples, it is safe to assume these conditions are met, thus:

$$\kappa(\omega) \approx Re[\chi(\omega)] \tag{2.57}$$

An example comparing absolute susceptibility to in-phase susceptibility can be seen in Figure 2.8. At frequencies $2\pi/\tau_2 \ll \omega \ll 2\pi/\tau_1$, the sample will behave according to Eq. (2.9) (Mullins and Tite, 1973; Dabas et al., 1992). The slope of the absolute magnetic susceptibility is slightly shallower, however, it only differs by a few % in comparison to the in-phase component. From this, I infer that:

$$\left|\frac{d\,Re[\chi(\omega)]}{d\,ln(\omega)}\right| \approx \left|\frac{d\,\kappa(\omega)]}{d\,ln(\omega)}\right| \approx \frac{\Delta\chi}{ln(\tau_2/\tau_1)} \tag{2.58}$$

The right-hand side of Eq. (2.58) represents an amalgamated magnetic property for the soil. This parameter is of great interest, as it characterizes the time-dependent magnetic decay during the off-time. According to expressions derived in Sections (2.3.3), (2.3.4) and (2.3.5), at $\tau_1 \ll t \ll \tau_2$:

$$\vec{M}(t) \approx \frac{\Delta\chi\vec{H}_0}{ln(\tau_2/\tau_1)} ln\left(1+\frac{\Delta t}{t}\right) \qquad \text{for Square-Pulse Excitation} \tag{2.59}$$

$$\vec{M}(t) \approx \frac{\Delta\chi\vec{H}_{max}}{ln(\tau_2/\tau_1)} \sum_{\ell=1}^{L} g\Big(\big[1/2-\ell\,\big]\Delta t\Big)\, ln\left(1+\frac{\Delta t}{t+(\ell-1)\Delta t}\right) \qquad \text{for Arbitrary Excitation} \tag{2.60}$$

$$\frac{d\vec{M}(t)}{dt} \approx -\frac{\Delta\chi\vec{H}_0}{ln(\tau_2/\tau_1)}\frac{1}{t} \qquad \text{for Step-Off Excitation} \tag{2.61}$$

$$\frac{d\vec{M}(t)}{dt} \approx -\frac{\Delta\chi\vec{H}_0}{ln(\tau_2/\tau_1)}\left[\frac{1}{t}-\frac{1}{t+\Delta t}\right] \qquad \text{for Square-Pulse Excitation} \tag{2.62}$$

$$\frac{d\vec{M}(t)}{dt} \approx -\frac{\Delta\chi\vec{H}_{max}}{ln(\tau_2/\tau_1)} \sum_{\ell=1}^{L} g\Big(\big[1/2-\ell\,\big]\Delta t\Big)\left[\frac{1}{t+(\ell-1)\Delta t}-\frac{1}{t+\ell\Delta t}\right] \qquad \text{for Arbitrary Excitation} \tag{2.63}$$

where $\vec{H}_0$ is the on-time field for step-off and square-pulse excitation, $\vec{H}_{max}$ is the applied magnetic field at its maximum amplitude, Δt sets the width for square pulse waveforms, and $g(t)$ is defined by Eq. (2.51). The amalgamated magnetic property can be recovered using dual-frequency measurements, if performed over the soil's mid-frequency range. This property can then be used to predict the soil's characteristic off-time response. For measurements acquired using a Barington MS2B dual-frequency sensor:

$$\frac{\Delta\kappa}{ln(10)} \approx \frac{\Delta\chi}{ln(\tau_2/\tau_1)} \tag{2.64}$$

The database presented by van Dam (et al., 2008), can therefore be used to infer a range of typical values for the amalgamated magnetic property. By examining $\Delta\kappa$ in Figure 2.7b, the majority of lateritic soils are characterized by values:

$$10^{-6} \leq \frac{\Delta\chi}{ln(\tau_2/\tau_1)} \leq 2.5\times10^{-3} \tag{2.65}$$

2.5 Electromagnetic Response from a Conductive and Magnetically Viscous Earth

Inductive source EM systems are frequently used for mineral exploration and the detection of unexploded ordnance. The viscous remanent magnetization exhibited by lateritic soils has been known to generate a distinct response. This response, which I will call the VRM response, becomes problematic when it masks anomalies generated by desired targets. The impact of iron-bearing soils on EM sensors can be examined by considering the response from a conductive and magnetically viscous half-space (Das, 2006; Pasion, 2007; Kozhevnikov and Antonov, 2008). Here, a half-space model is used to examine inductive and VRM responses in both the frequency and time-domain.

2.5.1 Model for the Response from a Conductive and Magnetically Viscous Half-Space

Consider the case where a large circular loop is placed horizontally over the surface of a conductive and magnetically viscous half-space. The geometry of the model is shown in Figure 2.9. In the frequency domain, the vertical and radial electromagnetic responses can be expressed using the Hankel transform (Ward and Hohmann, 1988):

$$H_z(\rho,z,\omega) = \frac{Ia}{2}\int_0^\infty r_{TE}e^{-\lambda(z+h)}\lambda J_1(\lambda a)J_0(\lambda\rho)d\lambda \tag{2.66}$$

and

$$H_\rho(\rho,z,\omega) = -\frac{Ia}{2}\int_0^\infty r_{TE}e^{-\lambda(z+h)}\lambda J_1(\lambda a)J_1(\lambda\rho)d\lambda \tag{2.67}$$

where ρ is the radial distance from the loop's center axis, z is the observation height, a is the radius of the loop and h is the loop's height off the ground. $J_0(\cdot)$ and $J_1(\cdot)$ are 0^{th} and 1^{st} order Bessel functions of the first kind, respectively. The reflection coefficient r_{TE}, for a homogeneous Earth with frequency-dependent physical properties, is defined by:

$$r_{TE} = \frac{\mu\lambda - \mu_0 k}{\mu\lambda + \mu_0 k} \tag{2.68}$$

where $k = \sqrt{\lambda^2 - i\omega\mu\sigma}$, ω is the angular frequency, σ is the Earth's conductivity, μ is the frequency-dependent magnetic premeability defined by Eq. 2.10, and $\mu_0 = 4\pi \times 10^{-7}$ N/A^2 is the permeability of free-space. For a given frequency and measurement location, Eqs. (2.66) and (2.67) are solved using the IIPBF adaptive quadrature package (Ratnanather et al., 2011).

The transient response to step-off excitation can be numerically computed using inverse sine and cosine transforms (Newman et al., 1986):

$$h(t) = -\frac{2}{\pi}\int_0^\infty \frac{Im[H(\omega)]}{\omega} cos(\omega t)\, d\omega = h(0) - \frac{2}{\pi}\int_0^\infty \frac{Re[H(\omega)]}{\omega} sin(\omega t)\, d\omega \tag{2.69}$$

and

$$\frac{\partial h(t)}{\partial t} = \frac{2}{\pi}\int_0^\infty Im[H(\omega)]\, sin(\omega t)\, d\omega = -\frac{2}{\pi}\int_0^\infty Re[H(\omega)]\, cos(\omega t)\, d\omega \tag{2.70}$$

where $h(0)$ represents the component of the field at $t = 0$. For my analysis, the UBC EM1DTM forward modeling code will be used to predict TEM responses. For this code, the shape of the transmitter can be arbitrary, any current waveform can be used to generate the primary field, and we can input a layered Earth model.

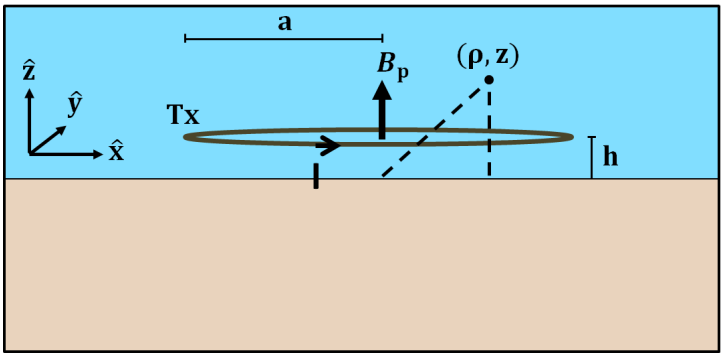

Figure 2.9: Schematic representing the geometry of the forward model.

2.5.2 Frequency Domain Response over a Conductive and Magnetically Viscous Half-Space

The primary field from a controlled source induces regions of magnetization and EM induction within the Earth. A qualitative representation of this is illustrated in Figure 2.10; where purple is used to show regions of magnetization, and red is used to show regions of EM induction. More saturated coloring is used to represent regions where magnetization and EM induction is likely stronger. Near the resistive limit ($\omega \to 0$), Faraday's law states that EM induction within the Earth is negligible. As a result, the Earth's response at low frequency is purely attributed to the magnetization of susceptible materials (Figure 2.10a). The intensity of the magnetization depends both on the strength of the inducing field and the magnetic susceptibility of the Earth. For a dipole source, the field will fall off proportional to r^{-3}. As the frequency of the primary field increases, so does the strength of EM induction within the Earth. The primary field is also subject to frequency-dependent attenuation. According to Griffiths (2007), the frequency-dependent attenuation of electromagnetic waves through a medium can be defined

by the skin depth:

$$\delta = \sqrt{\frac{2}{\omega \mu \sigma}} \tag{2.71}$$

where δ is the skin depth, ω is the angular frequency of the field, σ is conductivity, and μ is the frequency-dependent magnetic permeability from Eq. (2.10). Skin depth is defined as the distance at which the amplitude of a propagating wave decreases by a factor of $1/e$. Eq. (2.71) states that δ decreases proportional to $\omega^{-1/2}$. As frequency increases, the primary field does not penetrate the Earth as deeply. As a result, magnetization and EM induction begin to occur at shallower depths. The case where magnetic and inductive responses are competing is illustrated in Figure 2.10b. Towards the inductive limit ($\omega \to \infty$), EM induction is very strong and the Earth's magnetic response is negligible. According to Eq. (2.71), EM induction only occurs near the surface at high frequency. This case is illustrated in Figure 2.10c.

The vertical frequency domain response, for a circular transmitter loop on the surface of the Earth, is shown in Figure 2.11. In keeping with common convention, negative real and imaginary values are plotted in the upper right quadrant. I have chosen to plot only the secondary field. Eq. (2.8) is used to define the frequency-dependent magnetic susceptibility for the half-space. The frequency domain response was predicted for several models, including: a purely conductive Earth (σ = 0.1 S/m and χ = 0), a purely susceptible Earth (σ = 0 S/m, χ_∞ = 0.1, $\Delta\chi$ = 0.2, $\tau_1 = 10^{-5}$ s and τ_2 = 1 s), and a conductive and magnetically susceptible Earth (σ = 0.1 S/m, χ_∞ = 0.1, $\Delta\chi$ = 0.2, $\tau_1 = 10^{-5}$ s and τ_2 = 1 s).

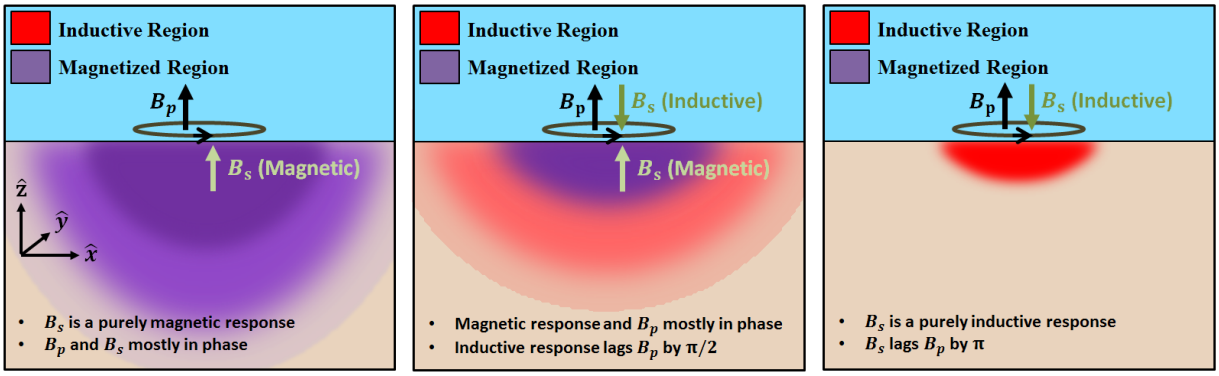

(a) Resistive Limit ($\omega \to 0$) **(b) Mid-Frequency** **(c) Inductive Limit ($\omega \to \infty$)**

Figure 2.10: Qualitative illustration of the Earth's frequency-domain response. More saturated colouring indicates regions where magnetization and EM induction are likely stronger.

The response at low frequencies is equal to the response from a purely susceptible Earth, as EM induction is negligible. Near the resistive limit, the secondary field is more or less in phase with the primary field. However, Figure 2.11b indicates the response of a magnetically viscous Earth at low frequencies exhibits small quadrature components. Because the frequency-dependent magnetic susceptibility decreases in magnitude with respect to ω, so does the Earth's magnetic response, even in the absence of EM induction. At sufficiently high frequencies, superparamagnetism is negligible, and only the infinite magnetic susceptible is capable of contributing towards the Earth's magnetic response. According to Ward and Hohmann (1988), the Earth's inductive response should

lag the primary field by $\pi/2$ radians at lower frequencies. This is observed for $f < 10^4$ Hz in Figure 2.11. As $\omega \to \infty$, the Earth's inductive response begins to lag the primary field by π radians; thus the inductive response opposes the primary field at high frequencies. From Figure 2.11, we can also see that as $\omega \to \infty$, the Earth's response is equivalent to that of a purely conductive Earth; implying the Earth's magnetic response is negligible.

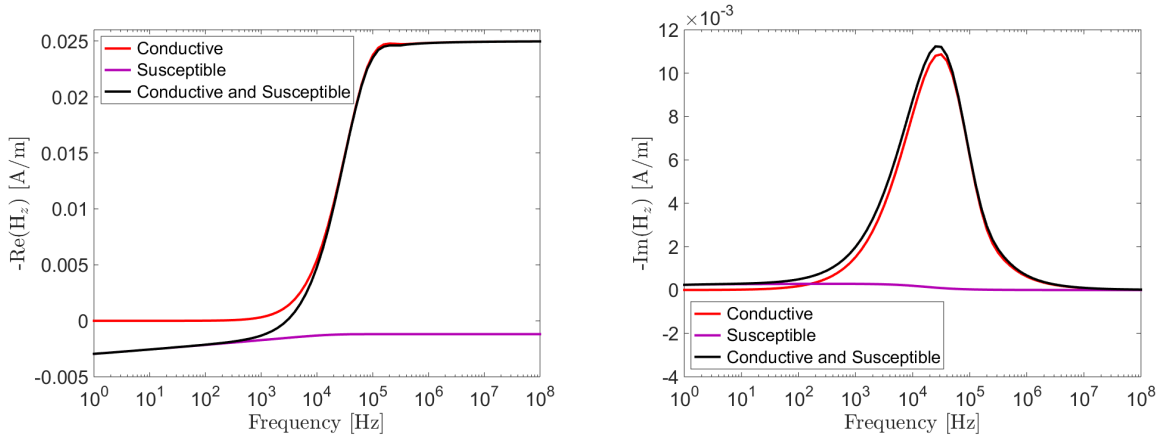

(a) In-Phase **(b)** Quadrature

Figure 2.11: Vertical frequency-domain response at the center of a circular transmitter loop over a conductive and magnetically viscous half-space. Responses were predicted at (ρ, z) = (0 m, 0.5 m) for a loop of radius a = 20 m using physical properties: purely conductive (σ = 0.1 S/m, χ = 0.1), purely susceptible (σ = 0 S/m, χ_∞ = 0.1, $\Delta\chi$ = 0.2, $\tau_1 = 10^{-5}$ s and τ_2 = 1 s), and conductive and magnetically susceptible (σ = 0.1 S/m, χ_∞ = 0.1, $\Delta\chi$ = 0.2, $\tau_1 = 10^{-5}$ s and τ_2 = 1 s)

2.5.3 Step-Off Response over a Conductive and Magnetically Viscous Half-Space

Removal of the primary field from a controlled source induces regions of VRM and EM induction within the Earth. A qualitative representation of this is illustrated in Figure 2.12; where purple is used to show regions of VRM, and red is used to show regions of EM induction. The strength of the VRM at early, mid and late times is represented by colour saturation of the purple region. According to field observation and numerical experimentation, the VRM response and its time-dependent derivative decay proportional to $ln(t)$ and $1/t$, respectively (Colani and Aitken, 1966; Buselli, 1982; Billings et al., 2003; Das, 2006; Pasion, 2007). The time-dependent diffusion of inductive eddy currents can be described using a downward propagating current filament, which maintains the geometry of the transmitter (Nabighian, 1979). A red ring is used to represent the current filament, or "smoke ring". In Figure 2.12, the concentration of inductive currents at early, mid and late times is represented by the thickness of the ring. At early times, inductive currents are near the surface, and the inductive response is strong (Figure 2.12a). By late times, inductive currents have diffused outwards and downwards, resulting in a weaker inductive response. (Figure 2.12c). Within a circular loop, the vertical step-off response from a conductive half-space will decay according to (Nabighian, 1979):

$$b_z(t) \approx \frac{I\sigma^{3/2}\mu_0^{5/2}a^2}{30\sqrt{\pi}}\, t^{-3/2} \tag{2.72}$$

and

$$\frac{\partial b_z(t)}{\partial t} \approx -\frac{I\sigma^{3/2}\mu_0^{5/2}a^2}{20\sqrt{\pi}}\, t^{-5/2} \tag{2.73}$$

where a is the radius of the loop, σ is the half-space conductivity, I is the steady-state current within the transmitter, and $\mu_0 = 4\pi \times 10^{-7}$ N/A^2 is the permeability of free-space. By comparing the characteristic decay of inductive and VRM responses, I postulate that EM induction likely dominates the early time response, whereas VRM likely dominates the late time response.

The vertical step-off response, for a circular transmitter loop on the surface of conductive and magnetically viscous half-space, is shown in Figure 2.13. Eq. (2.8) is used to define the frequency dependent magnetic susceptibility for the half-space. The time domain response was predicted for several models, including: a purely conductive Earth ($\sigma = 0.1$ S/m and $\chi = 0$), a purely susceptible Earth ($\sigma = 0$ S/m, $\chi_\infty = 0$, $\Delta\chi = 0.1$, $\tau_1 = 10^{-5}$ s and $\tau_2 = 1$ s), and a conductive and susceptible Earth ($\sigma = 0.1$ S/m, $\chi_\infty = 0$, $\Delta\chi = 0.1$, $\tau_1 = 10^{-5}$ s and $\tau_2 = 1$ s). The step-off response for a conductive and magnetically viscous Earth experiences a decay which is steep at early times, and more shallow at late times (reference). Early time responses to step-off excitation characteristically contain a large quantity of high frequency content. Thus, they represent the Earth's inductive response. In contrast, the late time response to step-off excitation is primarily comprised of low frequency content. This portion of the signal represents the VRM response.

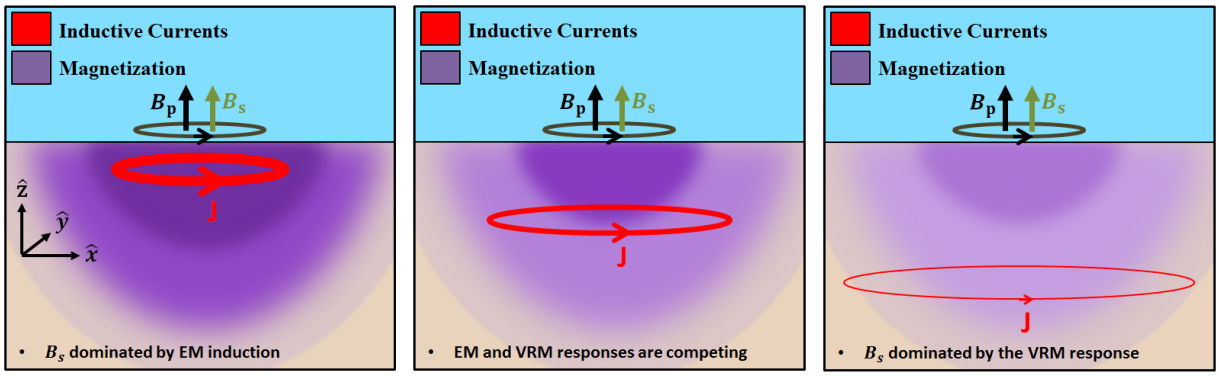

(a) Early Time Step-Off Response **(b) Mid-Time Step-Off Response** **(c) Late Time Step-Off Response**

Figure 2.12: Qualitative illustration of the Earth's step-off response. More saturated colouring indicates regions where VRM is stronger. The thickness of the current filament is used to represent the strength of induced eddy currents.

To first order, the Earth's inductive and VRM responses are separable, so long as the Earth's magnetic susceptibility is sufficiently small (Druyts et al., 2009) (Figure 2.13). This was first postulated by Buselli (1982); who used various SiroTEM configurations to perform field experiments. The approximation was later validated numerically by Pasion (2007), among others. At early times, the response is equivalent to that of a purely conductive Earth (red); at late times, the response is equivalent to that of a purely viscous Earth (purple). By summing the responses from these two models, I can approximate the response from a conductive and magnetically viscous Earth.

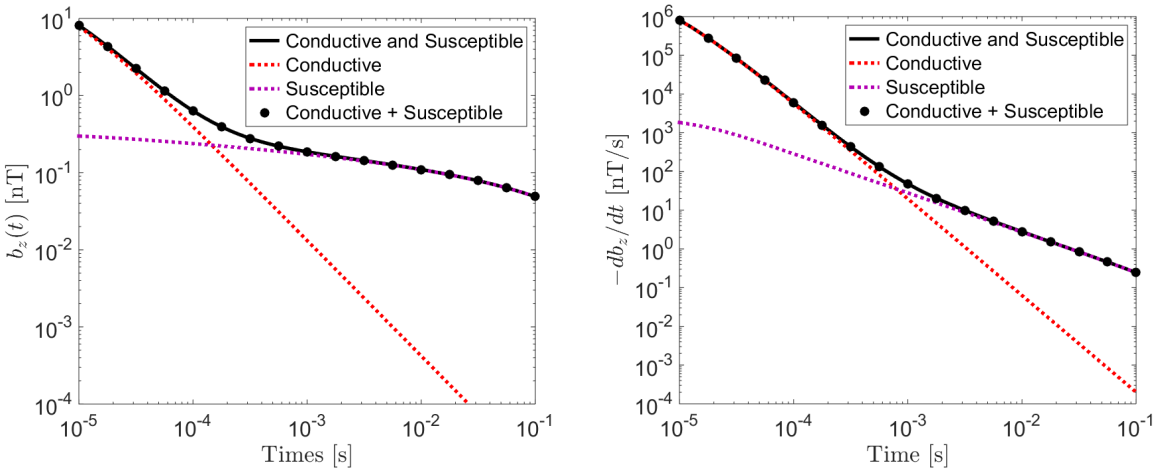

Figure 2.13: Vertical time domain response at the center of a circular transmitter loop over a conductive and magnetically viscous half-space. (a) $b_z(t)$ for unit step-off excitation (b) $-\partial b_z/\partial t$ for unit step-off excitation. Responses were predicted at (ρ, z) = (0 m, 0.5 m) for a loop of radius a = 20 m using physical properties: purely conductive (σ = 0.1 S/m, χ = 0), purely susceptible (σ = 0 S/m, χ_∞ = 0, $\Delta\chi$ = 0.1, $\tau_1 = 10^{-5}$ s and τ_2 = 1 s), conductive and susceptible (σ = 0.1 S/m, χ_∞ = 0, $\Delta\chi$ = 0.1, $\tau_1 = 10^{-5}$ s and τ_2 = 1 s). Conductive + susceptible is the sum of the responses from a purely conductive and a purely susceptible Earth.

2.6 Summary

In this chapter, I examined the magnetic properties which characterize iron-bearing soils, as well as the distinct magnetic response they produce. Iron-bearing soils exhibit viscous remanent magnetization, due to the presence of superparamagnetic iron-oxide grains. The magnetic properties of viscous soils were represented using a frequency-dependent magnetic susceptibility. A model for the magnetic susceptibility, defined by a log-uniform distribution of time-relaxation constants, was derived according to Néel relaxation theory. Not only is this model straightforward, but it can be used to adequately fit the magnetic viscosity in most soil samples. Over the mid-frequency range, in-phase magnetic susceptibility has been shown to decrease linearly with respect to $ln(\omega)$. In response to step-off excitation, the majority of viscous soils characteristically exhibit a magnetic decay proportional to $ln(t)$, with a time-dependent derivative proportional to $1/t$.

The zero-frequency magnetic susceptibilities for common iron-bearing soils are less than 0.05 SI. As a result, the effects of self-demagnetization are negligible. Mature soils tend to exhibit larger magnetic susceptibilities, as well as an increase in frequency-dependence. I defined an amalgamated magnetic property for magnetic viscosity, based on the susceptibility model; this model is characterized by a log-uniform distribution of time-relaxation constants. Not only is the amalgamated magnetic property easily obtained using dual-frequency magnetic susceptibility measurements, it also defines the soil's transient magnetic response during the off-time.

The response from a conductive and magnetically viscous Earth was examined by considering a large circular transmitter loop on the surface of a half-space. At low frequencies, the Earth's response is equivalent to that of a purely susceptible Earth, whereas at high frequencies, the Earth's response is equivalent to that of a purely conductive Earth. To first order, the inductive and VRM responses to step-off excitation can be considered separable if the Earth's magnetic susceptibility is sufficiently small. At early times, the response is purely inductive. Within the loop, the vertical inductive response is characterized by a decay proportional to $t^{-3/2}$, and a time-dependent derivative proportional to $t^{-5/2}$. At late times, the observed response is entirely attributed to magnetic viscosity. Thus at sufficiently late times, the response from a conductive and magnetically viscous Earth is equal to the VRM response. The decay of the VRM response and its time-dependent derivative are proportional to $ln(t)$ and $1/t$, respectively. In Chapter 3, I investigate the dependence of the VRM response on survey geometry.

Chapter 3

Dependence of Transient Inductive and VRM Responses on Survey Geometry

3.1 Introduction

In this chapter, I derive and test simplified expressions for the step-off VRM response, generated by a large circular loop over a conductive and magnetically viscous half-space. This is accomplished by considering the inductive and VRM responses as approximately separable. After sufficient time, EM induction is negligible and the VRM response can be predicted using a purely viscous Earth. Vertical and horizontal components of the VRM response, as well as its time-dependent rate of decay, are derived. Analytic expressions are used to determine relationships which exist between the transmitter loop, the VRM response and the inductive response. Expressions for the inductive response within the loop are provided by Nabighian (1979). Results are veried using the EM1DTM forward modeling code; the background theory of this code was covered in Section 2.5. Although the derivation in this chapter considers only the response to step-off excitation, analytic expressions may be easily adapted for square-pulse or other waveforms.

3.2 Integral Solution for the VRM Response Over a Magnetically Viscous Earth

Consider the step-off response from a conductive and magnetically viscous Earth. According to Section 2.5: 1) transient inductive and VRM responses are approximately separable, 2) inductive responses are negligible at sufficiently late times, 3) the late time response is approximately equal to the VRM response, and 4) the VRM response at late times can be approximated using a purely viscous Earth. From this, I may assume the late time signal is attributed solely to the viscous remanent magnetization occurring below the Earth's surface. According to Blakely (1996), the anomalous magnetic field outside of a magnetized region is given by the following integral equation:

$$\vec{b}(\vec{r},t) = \frac{\mu_0}{4\pi}\int_{V'} \nabla\nabla \frac{1}{|\vec{r}-\vec{r}'|}\cdot\vec{M}(\vec{r}',t)\,dV' \tag{3.1}$$

where $\vec{r}$ is the measurement location, $\vec{r}'$ are locations within the source region, and $\vec{M}(\vec{r}',t)$ is the viscous remanent magnetization at time t. According to Eq. (2.26), the viscous remanent magnetization in response to step-off excitation is given by:

$$\vec{M}(t) = \Delta\chi \vec{H}_0 F(t) \tag{3.2}$$

where $\Delta\chi$ is the zero-frequency magnetic susceptibility of all superparamagnetic (SP) grains, $\vec{H}_0$ represents the primary field during the on-time, and $F(t)$ is the after-effect function defined by Eq. (2.28). I assume that all viscous materials within the source region exhibit the same characteristic decay upon removal of the primary field. Under this assumption, $F(t)$ may be taken outside the integral in Eq. (3.3), thus:

$$\begin{aligned}\vec{b}(\vec{r},t) &= \frac{\mu_0}{4\pi} F(t) \int_{V'} \nabla\nabla \frac{1}{|\vec{r}-\vec{r}'|} \cdot \Delta\chi(\vec{r}')\vec{H}_0(\vec{r}')\, dV' \\ &= \vec{b}(\vec{r},0) F(t)\end{aligned} \tag{3.3}$$

where $\vec{b}(\vec{r},0)$ represents the steady-state magnetic response of all SP grains. Thus if $\vec{b}(\vec{r},0)$ is known, Eqs. (2.28) and (3.3) can be used to predict the VRM response at $t > 0$.

Similarly for the rate of decay:

$$\begin{aligned}\frac{\partial \vec{b}(\vec{r},t)}{\partial t} &= \frac{\mu_0}{4\pi} \frac{dF(t)}{dt} \int_{V'} \nabla\nabla \frac{1}{|\vec{r}-\vec{r}'|} \cdot \Delta\chi(\vec{r}')\vec{H}_0(\vec{r}')\, dV' \\ &= \vec{b}(\vec{r},0) \frac{dF(t)}{dt}\end{aligned} \tag{3.4}$$

where $dF(t)/dt$ is defined by Eq. (2.30). Thus if $\vec{b}(\vec{r},0)$ is known, Eqs. (2.30) and (3.4) can be used to predict $\partial B/\partial t$ at $t > 0$. Note that Eqs. (2.29) and (2.31) can be used instead of Eqs. (2.28) and (2.30) to approximate the response over $\tau_1 \ll t \ll \tau_2$. The necessary analytic expressions for $\vec{b}(\vec{r},0)$ are derived in Section 3.3.

3.3 Deriving the Steady-State Response Over a Superparamagnetic Half-Space

Here, expressions for the steady-state magnetic response are derived for a circular transmitter loop over a SP half-space. These expressions are used to replace $\vec{b}(\vec{r},0)$ in Eqs. (3.3) and (3.4). As only SP grains are considered, I are assuming $\chi_\infty = 0$ in Eq. (2.8).

Vertical and radial components of $\vec{b}(\vec{r},0)$ can be obtained directly from Hankel transform solutions found in Ward and Hohmann by taking their limits as $\omega \to 0$; Eqs. (4.87) and (4.88) in Ward and Hohmann (1988). For a transmitter loop of radius a, at height h above the surface, with steady-state current I:

$$b_z(\rho,z) = \frac{\mu_0 I a}{2} \left(\frac{\Delta\chi}{2+\Delta\chi} \right) \int_0^\infty \lambda e^{-\lambda(z+h)} J_1(\lambda a) J_0(\lambda\rho) d\lambda \tag{3.5}$$

and

$$b_\rho(\rho,z) = -\frac{\mu_0 Ia}{2}\left(\frac{\Delta\chi}{2+\Delta\chi}\right)\int_0^\infty \lambda e^{-\lambda(z+h)} J_1(\lambda a) J_1(\lambda\rho) d\lambda \tag{3.6}$$

where $\Delta\chi$ is the steady-state magnetic susceptibility due to the SP effects of the half-space, $\mu_0 = 4\pi\times10^{-7}$ N/A^2 is the permeability of free-space, ρ is the radial distance from the loop's center axis, and z is the height above the surface. $J_0(\cdot)$ and $J_1(\cdot)$ are 0$^{\text{th}}$ and 1$^{\text{st}}$ order Bessel functions of the first kind, respectively.

Thus in order to define the vertical and radial components of $\vec{b}(\vec{r},0)$, I require solutions to the integrals in Eqs. (3.5) and (3.6). For the vertical component $b_z(\rho,z)$, analytic solutions for several cases are derived in section 3.3.1. For the radial component $b_\rho(\rho,z)$, an approximate solution for special cases is proposed in section 3.3.2.

3.3.1 Vertical Steady-State Response for a Circular Loop over a Superparamagnetic Half-Space

Here, I predict the vertical steady-state response from a circular transmitter loop over SP half-space. According to Eq. (3.5), I require a solution to the integral:

$$\int_0^\infty \lambda e^{-\lambda(z+h)} J_1(\lambda a) J_0(\lambda\rho) d\lambda \tag{3.7}$$

For $\alpha \geq 0$, $\eta > -1/2$, and where $\Gamma(\cdot)$ is the gamma function, I can use the following integral identity (Erdelyi et al., 1954):

$$\int_0^\infty \lambda^{\eta-\nu} e^{-\lambda\alpha} J_\eta(\lambda a) J_\nu(\lambda\rho) d\lambda = \frac{a^\eta \rho^\nu \Gamma(\eta+\frac{1}{2})}{2^{\nu-\eta}\pi\Gamma(\nu+\frac{1}{2})}\int_0^\pi (sin\phi)^{2\nu}\left[(\alpha+i\rho cos\phi)^2+a\right]^{-\eta-1/2} d\phi \tag{3.8}$$

Where $\alpha = z+h \geq 0$, $\eta = 1$ and $\nu = 0$:

$$\int_0^\infty \lambda e^{-\lambda(z+h)} J_1(\lambda a) J_0(\lambda\rho) d\lambda = \frac{a}{\pi}\int_0^\pi \left[(z+h+i\rho cos\phi)^2+a^2\right]^{-3/2} d\phi \tag{3.9}$$

A general non-integral solution to Eq. (3.9) is difficult to derive analytically. However, I can gain valuable insight by considering several special cases.

Large Circular Loop on the Earth's Surface (h = 0)

Consider a large circular transmitter loop of radius a. If the steady-state response is examined close to the Earth's surface ($z \to 0$), then according to Eq. (3.9):

$$\lim_{z\to0}\int_0^\infty \lambda e^{-\lambda z} J_1(\lambda a) J_0(\lambda\rho) d\lambda = \frac{a}{\pi}\int_0^\pi \left[a^2-(\rho cos\phi)^2\right]^{-3/2} d\phi \tag{3.10}$$

$$= \frac{1}{\pi a}\frac{1}{\sqrt{a^2-\rho^2}} E\left[x\middle|\frac{\rho^2}{\rho^2-a^2}\right]\Bigg|_0^\pi \tag{3.11}$$

Eq. (3.11) was obtained from the right-hand side of Eq. (3.10) for $h,z=0$ using Wolfram Mathematica's online integration tool (Mathematica, 2016). $E[x|m]$ is the incomplete elliptic integral of the second kind, defined

by:

$$E[x|m] = \int_0^x [1 - m\sin^2\theta]^{1/2} d\theta \tag{3.12}$$

The incomplete elliptic integral has a few convenient properties. First of all, $E[\pi|m] = 2E[\pi/2|m] = 2E[m]$, where $E[m] = E[\pi/2|m]$ is the complete elliptic integral of the second kind. Given that $E[0|m] = 0$, Eq. (3.11) simplifies to:

$$\begin{aligned}\lim_{z\to 0}\int_0^\infty \lambda e^{-\lambda z} J_1(\lambda a) J_0(\lambda\rho) d\lambda &= \frac{2}{\pi a}\frac{1}{\sqrt{a^2-\rho^2}} E\left[\frac{\rho^2}{\rho^2 - a^2}\right] \\ &= \frac{2}{\pi a^2}\frac{1}{\sqrt{1-\left(\frac{\rho}{a}\right)^2}} E\left[\frac{\left(\frac{\rho}{a}\right)^2}{\left(\frac{\rho}{a}\right)^2 - 1}\right]\end{aligned} \tag{3.13}$$

Substituting Eq. (3.13) into Eq. (3.5), the vertical steady-state response on the Earth's surface, at time $t \leq 0$ and radial distance ρ from the loop's center axis is:

$$b_z(\rho,0) = \frac{\mu_0 I}{\pi a}\left(\frac{\Delta\chi}{2+\Delta\chi}\right)\frac{1}{\sqrt{1-\left(\frac{\rho}{a}\right)^2}} E\left[\frac{\left(\frac{\rho}{a}\right)^2}{\left(\frac{\rho}{a}\right)^2 - 1}\right] \tag{3.14}$$

$$= b_z(0,0)\left(\frac{2}{\pi\sqrt{1-\left(\frac{\rho}{a}\right)^2}} E\left[\frac{\left(\frac{\rho}{a}\right)^2}{\left(\frac{\rho}{a}\right)^2 - 1}\right]\right) \tag{3.15}$$

$$= b_z(0,0)\, G\left(\frac{\rho}{a}\right) \tag{3.16}$$

where $b_z(0,0)$ represents the stead-state magnetic response of the SP half-space at the loop's center, and G is a function which depends strictly on ρ/a.

For measurements inside the loop ($\rho < a$), I would like to find an approximate solution for G which does not contain the elliptic integral. At the center of the loop, $\rho/a = 0$, $E[0] = \pi/2$, and Eq. (3.15) simplifies to $b_z(0,0)$ as expected. As $\rho \to a$, we see that the steady-state response will approach infinity. To preserve these properties, I suggest an empirical function Q of the form:

$$G\left(\frac{\rho}{a}\right) \approx Q\left(\frac{\rho}{a}\right) = 1 + \frac{9}{4\pi}\left(\frac{\left(\frac{\rho}{a}\right)^2}{1-\left(\frac{\rho}{a}\right)^2}\right) \quad for\ \rho < a \tag{3.17}$$

This approximation proved to be accurate to within 1% for values ($\rho/a \leq 0.8$); at which point it began to increasingly overestimate the function (Figure 3.1a).

Using expressions (3.16) and (3.17), the vertical steady-state response at any location ($\rho < a, z = 0$), for a loop located on the Earth surface ($h = 0$), is approximately equal to:

$$b_z(\rho,0) \approx \frac{\mu_0 I}{2a}\left(\frac{\Delta\chi}{2+\Delta\chi}\right)\left[1 + \frac{9}{4\pi}\left(\frac{\left(\frac{\rho}{a}\right)^2}{1-\left(\frac{\rho}{a}\right)^2}\right)\right] \tag{3.18}$$

Response Along the Transmitter's Vertical Axis ($\rho = 0$)

Consider a circular transmitter loop of radius a at height h above the surface. Where z is the observation height along the transmitters vertical axis of symmetry, the vertical steady-state response can be obtained by setting $\rho \to 0$ and integrating Eq. (3.9):

$$\lim_{\rho \to 0} \int_0^\infty \lambda e^{-\lambda(z+h)} J_1(\lambda a) J_0(\lambda \rho) d\lambda = \frac{a}{\pi} \int_0^\pi \left(\frac{1}{(z+h)^2 + a^2} \right)^{3/2} d\phi = a \left(\frac{1}{(z+h)^2 + a^2} \right)^{3/2} \tag{3.19}$$

By substituting Eq. (3.19) into Eq. (3.5), the steady-state response is:

$$b_z(0,z) = \frac{\mu_0 I a^2}{2} \left(\frac{\Delta\chi}{2+\Delta\chi} \right) \left(\frac{1}{(z+h)^2 + a^2} \right)^{3/2} \tag{3.20}$$

By expressing the dipole moment of the transmitter as $m = \pi a^2 I$, Eq. (3.20) becomes :

$$b_z(0,z) \approx \frac{\mu_0 m}{2\pi} \left(\frac{\Delta\chi}{2+\Delta\chi} \right) \left(\frac{1}{(z+h)^2 + a^2} \right)^{3/2} \tag{3.21}$$

3.3.2 Radial steady-state Response from a Large Circular Loop

Here, I predict the radial steady-state response from a circular transmitter loop over a SP half-space. According to Eq. (3.6), I require a solution to the integral:

$$\int_0^\infty \lambda e^{-\lambda(z+h)} J_1(\lambda a) J_1(\lambda \rho) d\lambda \tag{3.22}$$

Although analytic solutions of Eq. (3.22) exist, they are far too complicated to develop any straightforward relationships with respect to the transmitter loop radius and observation locations. However, I can gain valuable insight by considering empirical solutions for several cases.

For $z+h > 0$, Eq. (3.22) was evaluated numerically using the IIPBF adaptive quadrature package (Ratnanather et al., 2011). I observed that for values of $0 < z+h \leq a/5$, numerical solutions to Eq. (3.22) displayed the characteristics of a Cauchy distribution centered around $\rho = a$. Using the probability density function for a Cauchy distribution, I approximate Eq. (3.22) as:

$$\int_0^\infty \lambda e^{-\lambda(z+h)} J_1(\lambda a) J_0(\lambda \rho) d\lambda \sim \left[\pi a \gamma \left(1 + \left(\frac{\rho - a}{\gamma} \right)^2 \right) \right]^{-1} \tag{3.23}$$

where an emprical function for γ is given by:

$$\gamma = 2(z+h) \left(\frac{2}{\pi} \right)^{3/2} \tag{3.24}$$

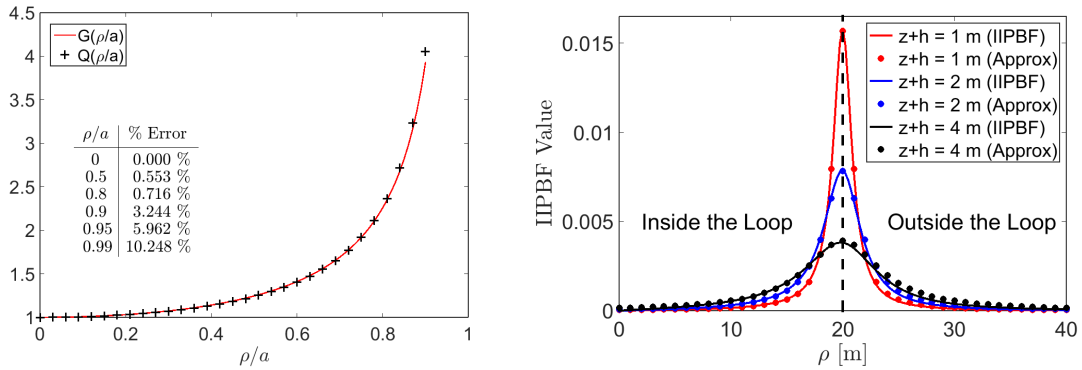

Figure 3.1: (a) Comparison between $G(\rho/a)$ and its approximation $Q(\rho/a)$ for various values of $\rho/a<1$. A % error for selected values is provided. (b) Comparison between computations of the Hankel transform using IIPBF adaptive quadrature and using the empirical expression from Eq. (3.23). Comparisons are done for various values of $0<z+h\leq a/5$, using a loop radius of $a=20$ m.

A comparison between computations using IIPBF adaptive quadrature and Eq. (3.23) for a loop of radius $a=20$ m is shown in (Figure 3.1b) for several values of $0<z+h\leq a/5$. As $z+h$ decreased over the accepted range, the Cauchy distribution became less broad. For $z+h\to 0$, the weighted orthogonality property of the Hankel transform can be used to show (Li and Wong, 2008):

$$\lim_{z+h\to 0}\int_0^\infty \lambda e^{-\lambda(z+h)}J_1(\lambda a)J_1(\lambda\rho)d\lambda=\frac{\delta(a-\rho)}{a} \tag{3.25}$$

where $\delta(x)$ is the Dirac delta function. By substituting expression (3.23) into Eq. (3.6), the radial steady-state response of the SP half-space for $0<z+h\leq a/5$ is approximated by:

$$B_\rho(\rho,z)\sim-\frac{\mu_0 I}{2}\left(\frac{\Delta\chi}{2+\Delta\chi}\right)\left[\pi a\gamma\left(1+\left(\frac{\rho-a}{\gamma}\right)^2\right)\right]^{-1} \tag{3.26}$$

It should be noted that although Eq. (3.26) provides a reasonable approximation over a certain range of values, it cannot be used to show that $B_\rho(\rho\to 0,z)=0$. This property can be obtained directly from Eq. (3.6) since $J_1(0)=0$.

3.4 VRM Response from a Large Circular Transmitter Loop

In this section, Eqs. (3.3) and (3.4) are used to approximate the VRM response over a SP half-space for $\tau_1\ll t\ll\tau_2$. Approximations for the after-effect function and its derivative for $\tau_1\ll t\ll\tau_2$ are provided by Eqs. (2.29) and (2.31). Vertical and radial components of the steady-state response in each case were derived in section (3.3).

3.4.1 Vertical VRM Response from a Large Circular Transmitter Loop

Large Circular Loop on the Earth's Surface (h = 0)

Using expressions (2.29), (3.3), and (3.18), the vertical magnetic flux density at any location $(\rho < a, z = 0)$ at time $\tau_1 \ll t \ll \tau_2$, is approximately equal to:

$$b_z(\rho,0,t) \approx \frac{\mu_0 I}{2a}\left(\frac{\Delta\chi}{2+\Delta\chi}\right)\left[1+\frac{9}{4\pi}\left(\frac{\left(\frac{\rho}{a}\right)^2}{1-\left(\frac{\rho}{a}\right)^2}\right)\right]\bar{F}(t) \tag{3.27}$$

Similarly using expressions (2.31), (3.4) and (3.18):

$$\frac{\partial b_z(\rho,0,t)}{\partial t} \approx \frac{\mu_0 I}{2a}\left(\frac{\Delta\chi}{2+\Delta\chi}\right)\left[1+\frac{9}{4\pi}\left(\frac{\left(\frac{\rho}{a}\right)^2}{1-\left(\frac{\rho}{a}\right)^2}\right)\right]\frac{d\bar{F}(t)}{dt} \tag{3.28}$$

According to expressions (3.27) and (3.28), the vertical VRM response is relatively consistent near the center of the loop ($\rho/a \leq 0.5$), and is inversely proportional to the transmitter loop's radius; matching results obtained by others (Buselli, 1982; Lee, 1984; Barsukov and Fainberg, 2001). However, as one moves out towards the edges of the loop, the VRM response can increase in magnitude rapidly with respect to ρ. The VRM response within a loop of radius $a = 20$ m can be seen in Figure 3.2. In practice, measurements of the magnetic flux density are not performed directly on the Earth's surface. Instead, data are typically collected at heights less than 1 m off the ground. However, for a sufficiently large loop, with a sufficiently larger than z, we should expect similar behaviour to the case which was just derived.

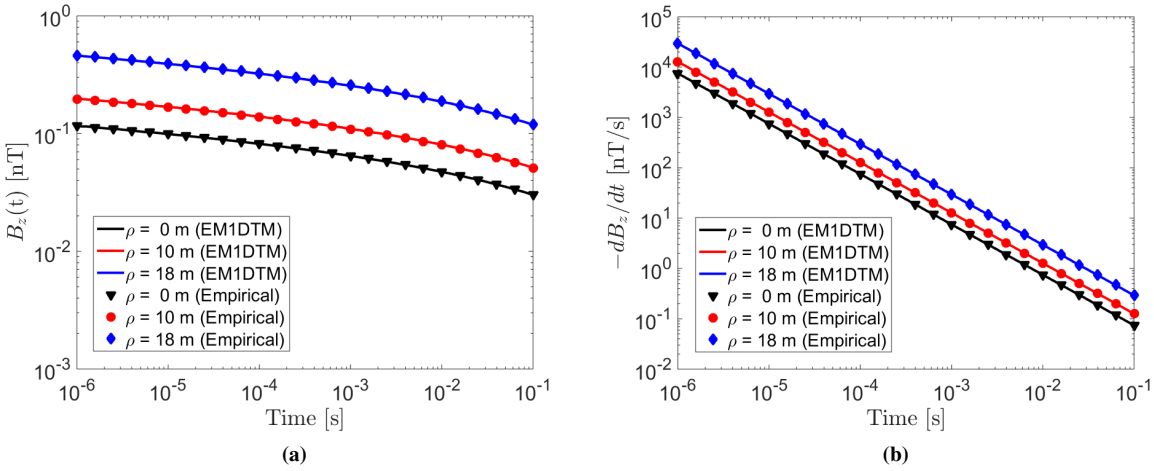

Figure 3.2: Vertical VRM response for a large circular loop of radius $a = 20$ m on the Earth's surface, at radial distance ρ from the loop's center, using properties $\Delta\chi = 0.01$, $\tau_1 = 10^{-8}$ s and $\tau_2 = 10$ s. This plot compares expressions (3.27) and (3.28) to values obtained using the EM1DTM code.

Response Along the Transmitter's Vertical Axis ($\rho = 0$)

Using expressions (2.29), (3.3), and (3.21), the magnetic flux density observed at time $\tau_1 \ll t \ll \tau_2$ is:

$$b_z(0,z,t) \approx \frac{\mu_0 m}{2\pi}\left(\frac{\Delta\chi}{2+\Delta\chi}\right)\left(\frac{1}{(z+h)^2+a^2}\right)^{3/2}\bar{F}(t) \tag{3.29}$$

Similarly, using expressions (2.31), (3.3), and (3.21), I obtain:

$$\frac{\partial b_z(0,z,t)}{\partial t} \approx \frac{\mu_0 m}{2\pi}\left(\frac{\Delta\chi}{2+\Delta\chi}\right)\left(\frac{1}{(z+h)^2+a^2}\right)^{3/2}\frac{d\bar{F}(t)}{dt} \tag{3.30}$$

According to expressions (3.29) and (3.30), the VRM response is smaller in magnitude when the size of the loop or the size of $z+h$ is increased. This matches analytic results and field observations made by others (Buselli, 1982; Lee, 1984; Barsukov and Fainberg, 2001). For $a \ll z+h$, the magnitude of the VRM response is proportional to $(z+h)^{-3}$. For $z+h=0$ and $m=\pi a^2 I$, expressions (3.29) and (3.30) are equivalent to expressions (3.27) and (3.28) at $\rho = 0$. The VRM response observed for a loop of radius $a = 0.2$ m is shown in Figure 3.3a.

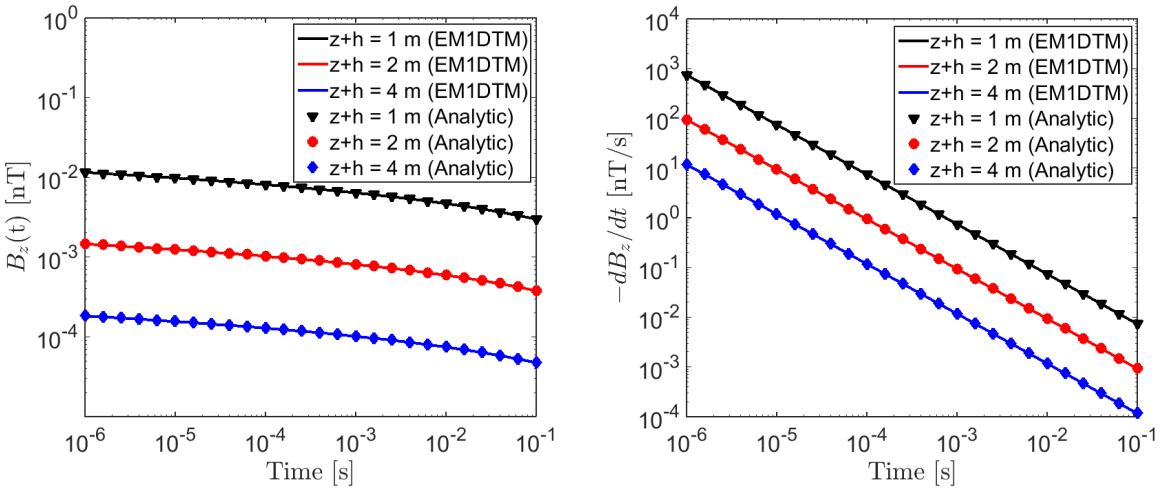

Figure 3.3: Vertical VRM response along the transmitters vertical axis of symmetry, using a radius of $a = 0.2$ m. Responses were predicted for several values $z+h$, using properties $\Delta\chi = 0.01$, $\tau_1 = 10^{-8}$ s and $\tau_2 = 10$ s. Plots compare Eqs. (3.29) and (3.30) to values obtained using the EM1DTM code.

3.4.2 Radial VRM Response from a Large Circular Loop

Using Eqs. (2.29), (3.3), and (3.26), the radial VRM response for $0 < z+h \leq a/5$ at time $\tau_1 \ll t \ll \tau_2$ is approximately equal to:

$$B_\rho(\rho,z,t) \sim -\frac{\mu_0 I}{2}\left(\frac{\Delta\chi}{2+\Delta\chi}\right)\left[\pi a\gamma\left(1+\left(\frac{\rho-a}{\gamma}\right)^2\right)\right]^{-1}\bar{F}(t) \tag{3.31}$$

Similarly, using expressions (2.31), (3.3) and (3.26):

$$\frac{\partial B_\rho(\rho,z,t)}{\partial t} \sim -\frac{\mu_0 I}{2}\left(\frac{\Delta\chi}{2+\Delta\chi}\right)\left[\pi a\gamma\left(1+\left(\frac{\rho-a}{\gamma}\right)^2\right)\right]^{-1}\frac{d\bar{F}}{dt} \tag{3.32}$$

Expressions (3.31) and (3.32) show that near the center of the loop, the radial component of the VRM response is small, however, the radial component of the VRM response increases signicantly as observations are made closer to the transmitter wire. The increase in magnitude as $\rho \to a$ is more gradual as $z+h$ increases. This effect was observed during field observations for various SiroTEM configurations (Buselli, 1982).

The radial VRM response for a loop of radius $a = 20$ m was forward modeled using the EM1DTM code. The radial VRM response was also predicted using Eqs. (3.31) and (3.32). Results using EM1DTM and empirical functions were compared for $z+h = 1$ for several values $\rho < a$ (Figures. 3.4a and 3.4b). Both approaches show the VRM response decays proportionally to $ln(t)$ for $B_\rho(t)$, and decays proportionally to $1/t$ for $\partial B_\rho/\partial t$.

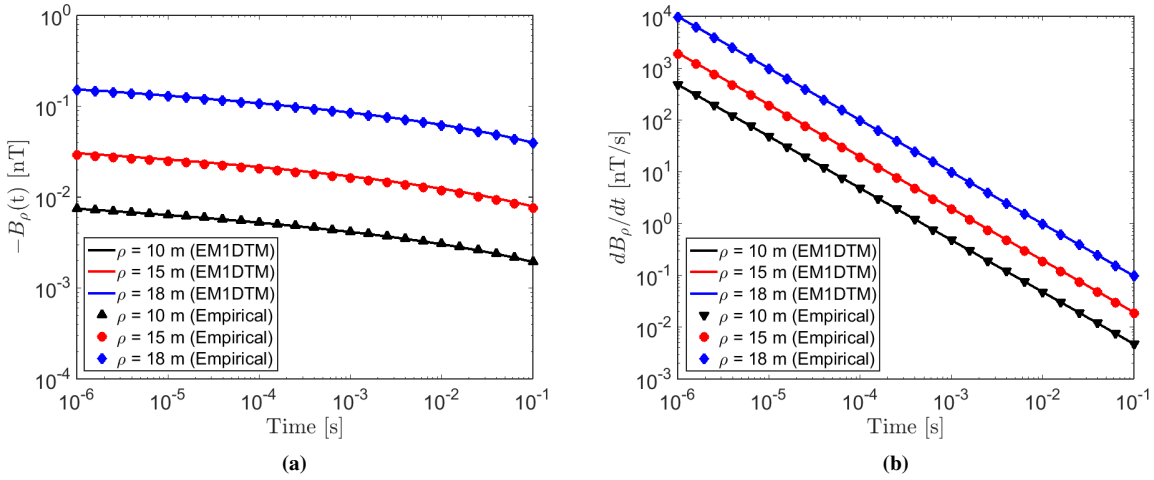

Figure 3.4: Comparison between EM1DTM and empirical functions (3.31) and (3.32) for the radial VRM response with a loop of radius $a = 20$ m. The response was predicted for $z+h = 20$ m using physical properties $\Delta\chi = 0.01$, $\tau_1 = 10^{-8}$ s and $\tau_2 = 10$ s. (a) $B_\rho(t)$. (b) dB_ρ/dt.

3.5 Comparing Inductive and VRM Responses over a Conductive and Magnetically Viscous Half-Space

The magnetic susceptibilities of lateritic soils are generally low ($\chi < 0.01$) (van Dam et al., 2004, 2005; Druyts et al., 2009); as such, the magnetic properties of lateritic soils do not have a significant impact on the inductive response. Research has indicated conductivity may be neglected when considering the soil's VRM response (Billings et al., 2003; Das, 2006; Druyts et al., 2009). Because of this, several publications have suggested the inductive and VRM responses from lateritic soils are approximately separable (Buselli, 1982; Das, 2006; Pasion, 2007). Here, I use the work in previous sections to compute the vertical inductive and VRM responses within a large circular transmitter loop and compare them as a function of the loop's radius. I assume the inductive and VRM responses are separable and that the inductive response is given by the late time approximation found in Nabighian (1979).

Nabighian (1979) showed that for a step-function excitation, to first-order, the quasi-static transient response from a transmitter loop on the Earth's surface could be approximated by a downward and outward moving current filament which maintained the geometry of the transmitter. Additionally, he showed that after sufficient time, the inductive response observed at locations within the loop would asymptotically approach the following expression:

$$b_z(t) \approx \frac{I\sigma^{3/2}\mu_0^{5/2}a^2}{30\sqrt{\pi}}t^{-3/2} \tag{3.33}$$

And that:

$$\frac{\partial b_z}{\partial t} \approx -\frac{I\sigma^{3/2}\mu_0^{5/2}a^2}{20\sqrt{\pi}}t^{-5/2} \tag{3.34}$$

where a is the loop's radius, σ is the Earth's conductivity and μ_0 is the permeability of free space. Note that the magnetic field and its derivative decay according to $t^{-3/2}$ and $t^{-5/2}$ respectively. Furthermore, the strength of the inductive response is proportional to a^2.

The ratio between the vertical inductive response $b_z^{(IND)}$ and the vertical VRM response $b_z^{(VRM)}$ within the loop at time $\tau_1 \ll t \ll \tau_2$, can be obtained using expressions (3.17), (3.27) and (3.33):

$$\begin{aligned} R_b &= \frac{b_z^{(IND)}}{b_z^{(VRM)}} \\ &\approx \frac{ln(\tau_2/\tau_1)}{15\,Q(\rho/a)\sqrt{\pi}}\left(\frac{2+\Delta\chi}{\Delta\chi}\right)\left(\frac{t^{-3/2}}{-\gamma - ln(t/\tau_2)}\right)(\mu_0\sigma)^{3/2}a^3 \end{aligned} \tag{3.35}$$

Similarly for the derivative, using expressions (3.17), (3.28) and (3.34):

$$\begin{aligned} R_{db/dt} &= \frac{db_z/dt^{(IND)}}{db_z/dt^{(VRM)}} \\ &\approx \frac{ln(\tau_2/\tau_1)}{10\,Q(\rho/a)\sqrt{\pi}}\left(\frac{2+\Delta\chi}{\Delta\chi}\right)(\mu_0\sigma)^{3/2}a^3t^{-3/2} \end{aligned} \tag{3.36}$$

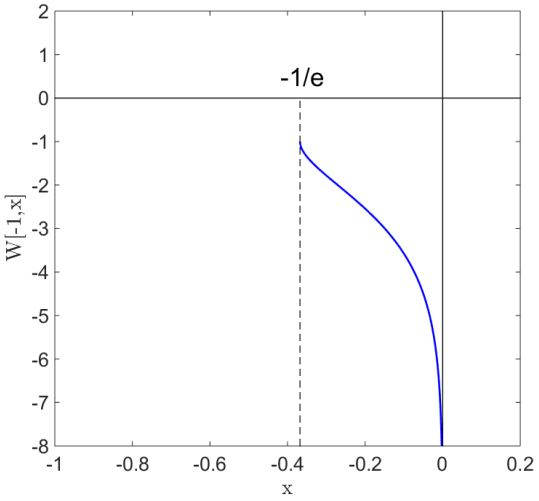

Figure 3.5: Lower branch of the Lambert W function $W[-1,x]$ for values $-1/e \leq x \leq 0$.

We would like to know the time at which magnetic viscosity begins to dominate the vertical observed response. This can be accomplished by solving $R_b = 1$ and $R_{db/dt} = 1$ in expressions (3.35) and (3.36), respectively. For db_z/dt, this is straightforward:

$$t_\beta \approx \left[\frac{ln(\tau_2/\tau_1)}{10Q(\rho/a)\sqrt{\pi}} \left(\frac{2+\Delta\chi}{\Delta\chi} \right) \right]^{2/3} \mu_0 \sigma a^2 \tag{3.37}$$

Expression (3.37) states that by increasingly the radius of a transmitter loop, the expected time t_β at which db_z/dt becomes dominated by the VRM response, is pushed to a later time. At the center of any loop, $Q = 1$ and $t_\beta \propto \sigma a^2$. Because $t_\beta \propto Q^{-2/3}$, we expect t_β to decrease as we move towards the edge of the loop. For $b_z(t)$, the VRM response begins to dominate at time:

$$t_\alpha \approx t_\beta \left(-W\left[-1, -\left(\frac{t_\beta}{\tau_2} e^\gamma \right)^{3/2} \right] \right)^{-2/3} \leq t_\beta \tag{3.38}$$

where $W[-1,x]$ is the lower branch of the Lambert W function (Corless et al., 1996), $\gamma = 0.5772$ is the Euler constant, and t_β is given by expression (3.37). $W[-1,x]$ for values $-1/e \leq x \leq 0$ is shown in Figure (3.5). A detailed derivation of Eq. (3.38), beginning at expression (3.35), can be found in Appendix B.

Expression (3.38) is rather complicated, but it does provide an explicit expression for t_α. In addition, t_α is a monotonic increasing function with respect to t_β. This implies that the relationships which exist between t_β, a and $Q(\rho/a)$ apply qualitatively to t_α as well. From expression (3.38), I can also state that TEM instruments which measure $b_z(t)$ are much more affected by the magnetic viscosity than instruments which measure db_z/dt. Expression (3.38) can also be used to show that $t_\alpha \ll t_\beta$ for $t_\beta \ll \tau_2 e^\gamma$.

The vertical transient responses at the center of several transmitter loops of varying radii are shown in Figure 3.6, and were calculated using the EM1DTM code. t_α and its corresponding value $b_z(t)$ were calculated using expressions (2.29), (3.27), (3.33) and (3.38). t_β and its corresponding value db_z/dt were calculated using expressions (2.31), (3.28), (3.34) and (3.37). Figure 3.6 confirms that t_α and t_β increase with respect to a, and that $t_\alpha \leq t_\beta$.

Now consider a single transmitter loop with fixed radius a, located on the Earth's surface. According to Eq. (3.17), Q increases as $\rho \to a$. As a result, the VRM response will begin to dominate the total observed transient response at increasingly early times. We expect to see this because magnetic viscosity is known to be most problematic at locations near the edges of the transmitter loop (Lee, 1984; Buselli, 1982; Barsukov and Fainberg, 2001). The vertical transient responses at various radial locations ρ within a transmitter loop of radius $a = 20$ m are shown in Figure 3.7, and were calculated using the EM1DTM code. t_α and its corresponding value $b_z(t)$ were calculated using expressions (2.29), (3.27), (3.33) and (3.38). t_β and its corresponding value db_z/dt were calculated using expressions (2.31), (3.28), (3.34) and (3.37). Figure 3.6 confirms that t_α and t_β increase with respect to ρ, and that $t_\alpha \leq t_\beta$.

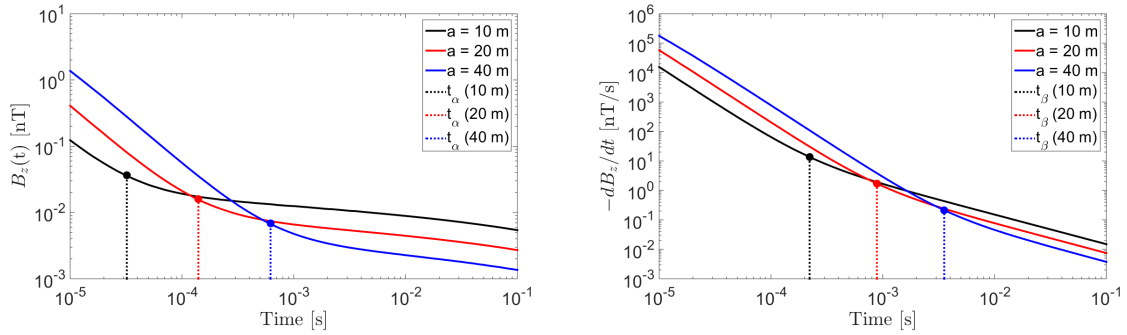

(a) **(b)**

Figure 3.6: Vertical transient response at the center of a set of transmitter loops with varying radii, located on the Earth's surface. EM1DTM was used to predict the responses for a half-space with physical properties: $\sigma = 10^{-2}$ S/m, $\Delta\chi = 0.001$, $\tau_1 = 10^{-8}$ s and $\tau_2 = 10$ s.

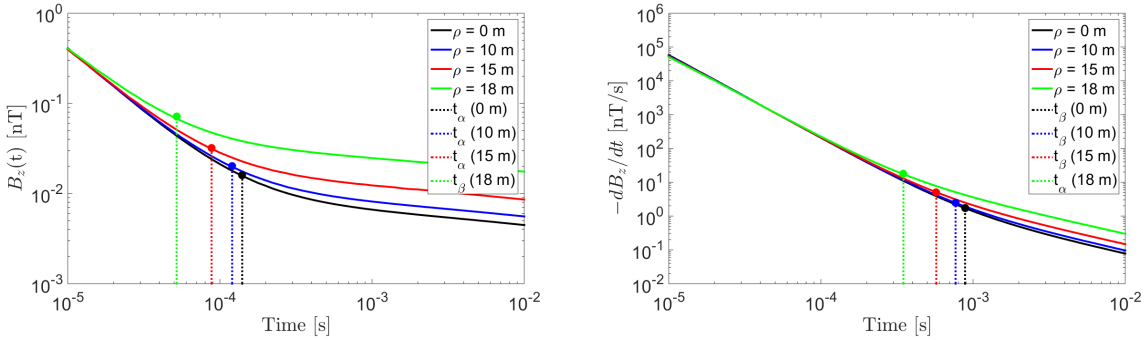

(a) **(b)**

Figure 3.7: Vertical transient response at off axis locations ρ, for a loop of radius $a = 20$ m, located on the Earth's surface. EM1DTM was used to predict the responses for a half-space with physical properties: $\sigma = 10^{-2}$ S/m, $\Delta\chi = 0.001$, $\tau_1 = 10^{-8}$ s and $\tau_2 = 10$ s.

Figures 3.6 and 3.7 demonstrate how Eqs. (3.37) and (3.38) can be used to predict the critical times (dashed lines) at which $b_z(t)$ and $\partial b_z/\partial t$ within the loop become dominated by the VRM response. Provided that a-priori information is supplied regarding the Earth's physical properties, Eqs. (3.35) through (3.38) have several practical applications. For example, Eqs. (3.35) and (3.36) can be used to approximate the loop size which renders the VRM response negligible over a specified range of time channels. This may assist in preliminary aspects of survey design. Meanwhile, Eqs. (3.37) and (3.38) can be used to indicate whether an increasingly shallow rate of decay during the late-time response may be attributed to a deeply buried conductor or viscous remanent magnetization.

3.6 Summary

In this chapter, I derived and tested simplified expressions for the transient VRM response, generated by a large circular loop over a conductive and magnetically viscous half-space. This was accomplished by solving integral equations representing the steady-state magnetic response, and using after-effect functions derived by Néel (1949) for a collection of non-interacting SP grains. Analytic expressions were then verified using the UBC EM1DTM forward modeling code.

According to the derivations performed in this chapter, both the vertical and radial components of the VRM response vary minimally near the center of the loop; with the vertical component being proportional to $1/a$. The results conclude that observed VRM responses are larger near the transmitter wire, larger for smaller transmitter loops, and lower when observations are made further above the ground; these conclusions are consistent with various field observations and numerical modeling results (Buselli, 1982; Barsukov and Fainberg, 2001; Billings et al., 2003; Pasion, 2007; Kozhevnikov and Antonov, 2008; Zadorozhnaya et al., 2012). By deriving expressions for the radial component of the VRM response, we can better understand the impact of magnetic viscosity on TEM instruments which collect 3-component data about a large transmitter loop. Analytic expressions show that magnetic viscosity begins to affect the magnetic ux density $b(t)$ at much earlier times than its time derivative db/dt. For db/dt, the time at which the VRM response begins to dominate the response is $\propto a^2$; the equivalent expression for $b(t)$ is more complicated. As a first pass, expressions derived in this chapter provide an intuitive understanding of the VRM response and how it depends on the survey geometry. Unfortunately, the derived expressions are not applicable in geological environments where the soil's magnetic properties show significant spatial variation. As a result, I construct a model for predicting the VRM responses from three-dimensional bodies in Chapter 4.

Chapter 4

Modeling the VRM Response in 3D

4.1 Introduction

Models for predicting the anomalous field outside a magnetized body have been researched for over half a century. Rapid computation of the anomalous field can be performed by discretizing the body into a finite set of volumes (or cells), each with its own uniform magnetization. By assuming magnetizations within nearby cells do not impact one another, the anomalous field can be expressed as the vector sum of all individual contributions; which can be represented using a linear system (Sharma, 1966; Rao and Babu, 1993; Varga et al., 1996; Fournier, 2015).

In this chapter, I present a linear forward modeling scheme for predicting the off-time VRM response from three-dimensional bodies. The Earth's subsurface is discretized into a set of rectangular prisms with homogenous physical properties. If the characteristic decay of the response is known, the forward model may be written compactly, and the VRM response does not need to be predicted independently at each time. For viscous remanent magnetization to be uniform within each cell, I assume the on-time inducing field throughout each cell is approximately equal its value at the cell's center. For cells which are close to the transmitter, I introduce an algorithm for refining geometric sensitivities; thus providing an increase in numerical accuracy. Convergence of the forward model as a function of the level of refinement is examined. The forward modeling code (called VRM3D) is validated using EM1DTM. Given that the off-time inductive and VRM responses are approximately separable, the output from the VRM3D code can be added to that of a 3D TEM code to predict the response from a conductive and magnetically viscous Earth.

4.2 Forward Model for VRM Responses from 3D Objects

4.2.1 VRM Response from a Magnetized Body

In Section 2.5 I established that EM and VRM responses during the off-time are approximately separable, and that VRM responses could be predicted using a purely viscous Earth. In Section 3.2, I presented an integral expression for predicting the anomalous magnetic field outside a region exhibiting viscous remanent magnetization.

According to Eq. (3.3), the VRM response $\vec{b}(P,t)$, at location P, due to viscous remanent magnetization at Q is (Blakely, 1996):

$$\vec{b}(P,t) = \frac{\mu_0}{4\pi} \int_V \nabla\nabla \frac{1}{r} \cdot \vec{M}(Q,t)\, dV \tag{4.1}$$

where

$$r = \sqrt{\left(x_P - x_Q\right)^2 + \left(y_P - y_Q\right)^2 + \left(z_P - z_Q\right)^2} \tag{4.2}$$

and $\vec{M}(Q,t)$ represents the viscous remanent magnetization within the source region.

For a rectangular prism, Bhattacharyya (1964) was able to provide an analytic solution to the integral in Eq. (4.1); provided the magnetization within the volume is homogeneous. A more pleasant form of this solution may be found in Varga (1996). If this condition is satisfied, Eq. (4.1) can be expressed as a linear system:

$$\vec{b}(t) = G \cdot \vec{M}(t) \tag{4.3}$$

where

$$\vec{b}(P,t) = \begin{bmatrix} b_x(P,t) \\ b_y(P,t) \\ b_z(P,t) \end{bmatrix} \;,\; \vec{M}(t) = \begin{bmatrix} M_x(t) \\ M_y(t) \\ M_z(t) \end{bmatrix} \text{ and } G = \begin{bmatrix} g_{xx} & g_{xy} & g_{xz} \\ g_{yx} & g_{yy} & g_{yz} \\ g_{zx} & g_{zy} & g_{zz} \end{bmatrix} \tag{4.4}$$

G is a 3×3 tensor representing a linear operator between the magnetization of the cell, and the anomalous VRM response at location P. G is a symmetric matrix with $g_{xx} + g_{yy} + g_{zz} = 0$. Therefore, $\mathbf{G}$ only has 5 unique entries. From Eq. (4.3) the components of $\vec{b}(P,t)$ may be expressed as:

$$b_x(P,t) = g_{xx}M_x(t) + g_{xy}M_y(t) + g_{xz}M_z(t) \tag{4.5}$$

$$b_y(P,t) = g_{yx}M_x(t) + g_{yy}M_y(t) + g_{yz}M_z(t) \tag{4.6}$$

$$b_z(P,t) = g_{zx}M_x(t) + g_{zy}M_y(t) + g_{zz}M_z(t) \tag{4.7}$$

Now consider a discrete set of K uniformly magnetized rectangular volumes. By assuming magnetizations within nearby cells do not impact one another, the total anomalous field can be expressed as a sum of the individual contributions (Sharma, 1966):

$$\vec{b}(P,t) = \sum_{k=1}^{K} G^k \cdot \vec{M}^k(t) \tag{4.8}$$

From Eq. (4.8), the $\hat{x}$ component $b_x(P,t)$ can be expressed as:

$$b_x(P,t) = \begin{bmatrix} g_{xx}^1 \ldots g_{xx}^K & g_{xy}^1 \ldots g_{xy}^K & g_{xz}^1 \ldots g_{xz}^K \end{bmatrix} \begin{bmatrix} \mathbf{M_x}(t) \\ \mathbf{M_y}(t) \\ \mathbf{M_z}(t) \end{bmatrix} \tag{4.9}$$

where

$$\mathbf{M_x}(t) = \begin{bmatrix} M_x^1(t) \\ \vdots \\ M_x^K(t) \end{bmatrix}, \quad \mathbf{M_y}(t) = \begin{bmatrix} M_y^1(t) \\ \vdots \\ M_y^K(t) \end{bmatrix} \quad \text{and} \quad \mathbf{M_z}(t) = \begin{bmatrix} M_z^1(t) \\ \vdots \\ M_z^K(t) \end{bmatrix} \tag{4.10}$$

Similar expressions can be shown for $b_y(P,t)$ and $b_z(P,t)$. In practice, the anomalous magnetic field generated by a magnetized body is measured at multiple locations. For N locations, the $\hat{x}$, $\hat{y}$ and $\hat{z}$ components of the anomalous field can be organized as:

$$\mathbf{b_x}(t) = \begin{bmatrix} b_x(P_1,t) \\ \vdots \\ b_x(P_N,t) \end{bmatrix}, \quad \mathbf{b_y}(t) = \begin{bmatrix} b_y(P_1,t) \\ \vdots \\ b_y(P_N,t) \end{bmatrix} \quad \text{and} \quad \mathbf{b_z}(t) = \begin{bmatrix} b_z(P_1,t) \\ \vdots \\ b_z(P_N,t) \end{bmatrix} \tag{4.11}$$

Each of the vectors in Eq. (4.11) are obtained by applying a linear operation to an identical vector. Therefore, I can define the following compact system:

$$\mathbf{b}(t) = \mathbf{G}\,\vec{\mathbf{M}}(t) \tag{4.12}$$

where

$$\mathbf{b}(t) = \begin{bmatrix} \mathbf{b_x}(t) \\ \mathbf{b_y}(t) \\ \mathbf{b_z}(t) \end{bmatrix}, \quad \vec{\mathbf{M}}(t) = \begin{bmatrix} \mathbf{M_x}(t) \\ \mathbf{M_y}(t) \\ \mathbf{M_z}(t) \end{bmatrix} \quad \text{and} \quad \mathbf{G} = \begin{bmatrix} G_{xx} & G_{xy} & G_{xz} \\ G_{yx} & G_{yy} & G_{yz} \\ G_{zx} & G_{zy} & G_{zz} \end{bmatrix} \tag{4.13}$$

$\mathbf{b}(t)$ is a column vector of length $3N$, $\vec{\mathbf{M}}(t)$ is a column vector of length $3K$, and $\mathbf{G}$ is a $3N \times 3K$ matrix whose rows are created according to Eq. (4.9). Note that $\mathbf{G}$ is independent of time. If the anomalous $\partial\vec{b}(t)/\partial t$ response is being measured, I can simply take the derivative of Eq. (4.12).

$$\frac{\partial}{\partial t}\mathbf{b}(t) = \mathbf{G}\,\frac{d\vec{\mathbf{M}}(t)}{dt} \tag{4.14}$$

where $d\vec{\mathbf{M}}(t)/dt$ contains cartesian components of the time-dependent rate of decay for each cell.

4.2.2 Parameterizing the VRM Response Using the Amalgamated Magnetic Parameter

From Sections 2.3.3, 2.3.4 and 2.3.5, I showed that viscous remanent magnetization during the off-time could be expressed in terms of an after-effect function:

$$\vec{M}(t) = \Delta\chi\,\vec{H}\,F(t) \tag{4.15}$$

where $\Delta\chi$ is the zero-frequency magnetic susceptibility of all superparamagnetic grains and $F(t)$ is the after-effect function. $\vec{H}$ represents the primary field at its maximum amplitude during the on-time. $\vec{H}$ was defined in Chapter 2 as $\vec{H}_0$ for step-off and square-pulse excitations and defined as $\vec{H}_{max}$ for an arbitrary waveform excitation. $\vec{H}$ can be split into cartesian components such that:

$$\vec{H} = \begin{bmatrix} H_x \\ H_y \\ H_z \end{bmatrix} \tag{4.16}$$

In Section 2.4, I proposed an amalgamated magnetic property to represent the magnetic viscosity of a sample. This property characterizes the time-dependent magnetic relaxation during the off-time. It can also be obtained using dual-frequency magnetic susceptibility measurements. According to Eq. (2.58), the amalgamated magnetic property for each cell is:

$$m = \frac{\Delta\chi}{ln(\tau_2/\tau_1)} \tag{4.17}$$

where τ_1 and τ_2 are finite limits for a log-uniform distribution of time-relaxation constants, which characterize a collection of superparamagnetic grains. According to expressions from Sections 2.3.3, 2.3.4 and 2.3.5, if observations are made a $\tau_1 \ll t \ll \tau_2$:

$$\vec{M}(t) \approx -m\vec{H}\,ln(t) + \frac{\Delta\chi\,\vec{H}}{ln(\tau_2/\tau_1)}\big[-\gamma + ln(\tau_2)\big] \qquad \text{for Step-Off Excitation} \tag{4.18}$$

$$\vec{M}(t) \approx m\vec{H}\,ln\left(1+\frac{\Delta t}{t}\right) \qquad \text{for Square-Pulse Excitation} \tag{4.19}$$

$$\vec{M}(t) \approx m\vec{H}\sum_{\ell=1}^{L} g\Big(\big[1/2-\ell\,\big]\Delta t\Big)\,ln\left(1+\frac{\Delta t}{t+(\ell-1)\Delta t}\right) \qquad \text{for an Arbitrary Waveform} \tag{4.20}$$

$$\frac{d\vec{M}(t)}{dt} \approx -m\vec{H}\,\frac{1}{t} \qquad \text{for Step-Off Excitation} \tag{4.21}$$

$$\frac{d\vec{M}(t)}{dt} \approx -m\vec{H}\left[\frac{1}{t}-\frac{1}{t+\Delta t}\right] \qquad \text{for Square-Pulse Excitation} \tag{4.22}$$

$$\frac{d\vec{M}(t)}{dt} \approx -m\vec{H}\sum_{\ell=1}^{L} g\Big(\big[1/2-\ell\,\big]\Delta t\Big)\left[\frac{1}{t+(\ell-1)\Delta t}-\frac{1}{t+\ell\Delta t}\right] \qquad \text{for an Arbitrary Waveform} \tag{4.23}$$

where $\gamma \approx 0.5772$ is the Euler constant and Δt is the square-pulse width. $g(t) = I(t)/I_{max}$ was defined by Eq. (2.51), and represents a function based on on-time current within the transmitter. For square-pulse excitation, I also require that $\Delta t \ll \tau_2$. And for an arbitrary inducing field, I require the total time-length of the waveform $\lambda \ll \tau_2$. Unfortunately, the magnetization to step-off excitation cannot be parameterized solely in terms of the amalgamated magnetic parameter, and requires an additional term. For the remaining expressions however, $\vec{M}(t)$ or $d\vec{M}(t)/dt$ can be predicted at $\tau_1 \ll t \ll \tau_2$ if m and the properties of the inducing field are known.

Now consider the off-time magnetization $\vec{\mathbf{M}}(t)$ experienced by all cells at time $\tau_1 \ll t \ll \tau_2$. Because magnetization is parallel to the inducing field, each component of the magnetization is separable. For square-pulse excitation, Eq. (4.19) can be adapted to show that:

$$\mathbf{M_x}(t) = \mathbf{H_x}\cdot\mathbf{m}\,ln\Big(1+\Delta t/t\Big) \tag{4.24}$$

$$\mathbf{M_y}(t) = \mathbf{H_y}\cdot\mathbf{m}\,ln\Big(1+\Delta t/t\Big) \tag{4.25}$$

$$\mathbf{M_z}(t) = \mathbf{H_z}\cdot\mathbf{m}\,ln\Big(1+\Delta t/t\Big) \tag{4.26}$$

where

$$\mathbf{H_x} = \begin{bmatrix} H_x^1 & & \\ & \ddots & \\ & & H_x^K \end{bmatrix}, \quad \mathbf{H_y} = \begin{bmatrix} H_y^1 & & \\ & \ddots & \\ & & H_y^K \end{bmatrix}, \quad \mathbf{H_z} = \begin{bmatrix} H_z^1 & & \\ & \ddots & \\ & & H_z^K \end{bmatrix}, \quad \text{and} \quad \mathbf{m} = \begin{bmatrix} m_1 \\ \vdots \\ m_K \end{bmatrix} \tag{4.27}$$

Vector $\mathbf{m}$ represents the amalgamated magnetic parameter for all cells. $\mathbf{H_x}$, $\mathbf{H_y}$, and $\mathbf{H_z}$ are diagonal $K \times K$ matricies. They contain the $\hat{x}$, $\hat{y}$ and $\hat{z}$ components of the maximum amplitude on-time field at the cell centers, respectively. $\vec{\mathbf{M}}(t)$ can be obtained using expressions (4.24) through (4.27):

$$\vec{\mathbf{M}}(t) = \mathbf{H}\mathbf{m}\, ln\Big(1 + \Delta t/t\Big) \tag{4.28}$$

where

$$\mathbf{H} = \begin{bmatrix} \mathbf{H_x} \\ \mathbf{H_y} \\ \mathbf{H_z} \end{bmatrix} \tag{4.29}$$

Substituting Eq. (4.28) into Eq. (4.12), $\mathbf{b}(t)$ for square-pulse excitation is given by:

$$\mathbf{b}(t) = \mathbf{G}\mathbf{H}\mathbf{m}\, ln\Big(1 + \Delta t/t\Big) \tag{4.30}$$

By the same approach, the time-dependent rate of decay for square-pulse excitation is given by:

$$\frac{\partial}{\partial t}\mathbf{b}(t) = -\mathbf{G}\mathbf{H}\mathbf{m} \left[\frac{1}{t} - \frac{1}{t + \Delta t}\right] \tag{4.31}$$

And for an arbitrary waveform, $\mathbf{b}(t)$ is given by:

$$\mathbf{b}(t) = \mathbf{G}\mathbf{H}\mathbf{m} \left[\sum_{\ell=1}^{L} g\Big(\big[1/2 - \ell\,\big]\Delta t\Big)\, ln\left(1 + \frac{\Delta t}{t + (\ell - 1)\Delta t}\right)\right] \tag{4.32}$$

Notice that Eqs. (4.30), (4.31) and (4.32) are obtained by scaling the product of $\mathbf{G}\mathbf{H}\mathbf{m}$ by a purely time-dependent function. Regardless of whether $\mathbf{b}(t)$ or $\partial\mathbf{b}/\partial t$ are being predicted, the same approach may be applied for any waveform. The time-dependent function which scales $\mathbf{G}\mathbf{H}\mathbf{m}$ in each case depends on the waveform. This function, which I define using $\eta(t)$, will be referred to as the characteristic decay function; for example, $\eta(t) = ln\big(1 + \Delta t/t\big)$ in Eq. (4.30). As a result, the off-time VRM response for any waveform can be expressed as follows:

$$\mathbf{d}(t) = \eta(t)\,\mathbf{G}\mathbf{H}\mathbf{m} \tag{4.33}$$

where $\mathbf{d}(t)$ represents either $\mathbf{b}(t)$ or $\partial\mathbf{b}/\partial t$ at time $\tau_2 \ll t \ll \tau_2$. Where N is the number of observation locations, the product of $\mathbf{G}\mathbf{H}\mathbf{m}$ is a vector of length $3N$.

We may be interested in predicting data for multiple times. For M time channels, I define the following vector:

$$\eta = \begin{bmatrix} \eta(t_1) \\ \vdots \\ \eta(t_M) \end{bmatrix}, \tag{4.34}$$

where η contains evaluations of the characteristic decay function at discrete times. To predict the VRM response at all location and at all times, I simply need to multiply each of the elements within vector $\mathbf{G}\,\mathbf{H}\,\mathbf{m}$ by the elements within vector η; resulting in $3MN$ values which must be organized appropriately into a final data vector. Thus, only a single evaluation of $\mathbf{G}\,\mathbf{H}\,\mathbf{m}$ is required, regardless of the number of measurement times. By introducing a linear operator $\mathbf{T}$, the final predicted data vector may be expressed as:

$$\mathbf{d} = \mathbf{T}\,\mathbf{G}\,\mathbf{H}\,\mathbf{m} \tag{4.35}$$

where $\mathbf{d}$ is a vector of length $3MN$ which contains the predicted VRM response at all locations and at all times. $\mathbf{T}$ is called the characteristic decay matrix and has dimensions $3MN \times 3N$. $\mathbf{T}$ is sparse, and populated by elements from vector η. The structure of $\mathbf{T}$ depends on the desired ordering of elements within $\mathbf{d}$. I have chosen to organize $\mathbf{d}$ as follows:

$$\mathbf{d} = \begin{bmatrix} \mathbf{d_x} \\ \mathbf{d_y} \\ \mathbf{d_z} \end{bmatrix}, \quad \mathbf{d_x} = \begin{bmatrix} d_x^1 \\ \vdots \\ d_x^N \end{bmatrix}, \quad \text{and} \quad d_x^1 = \begin{bmatrix} d_x^1(t_1) \\ \vdots \\ d_x^1(t_M) \end{bmatrix} \tag{4.36}$$

In this case, matrix $\mathbf{T}$ is formed by the following Kronecker product:

$$\mathbf{T} = \mathbf{I_{3N}} \otimes \eta \tag{4.37}$$

where $\mathbf{I_{3N}}$ is the $3N \times 3N$ identity matrix, and η is defined by Eq. (4.34). The final expression for the forward model is obtained by combining $\mathbf{G}$ and $\mathbf{H}$ into a single matrix $\mathbf{A}$; which contains all geometric information related to the forward problem. Thus:

$$\mathbf{d} = \mathbf{T}\,\mathbf{G}\,\mathbf{H}\,\mathbf{m} = \mathbf{T}\,\mathbf{A}\,\mathbf{m} \tag{4.38}$$

$\mathbf{A}$ is called the geometric sensitivity matrix, and has dimension $3N \times K$; where N is the number of observation locations and K is the number of cells. Because $\mathbf{H}$ is sparse, explicit generation of $\mathbf{A}$ is computationally fast. According to Eq. (4.38), the final data vector is obtained by applying a sparse matrix $\mathbf{T}$ to the product of $\mathbf{A}\,\mathbf{m}$. Although $\mathbf{A}$ is a dense matrix, its dimensions do not depend on the number of observation times. Therefore, the computational expense and memory requirements for the forward model do not increase noticeably as the number of observation times is increased.

4.3 Refinement of the Geometry Sensitivity Matrix

For sufficient numerical accuracy, the inducing field within each cell must be approximately equal to the value at the cell's center. For cells in proximity to a controlled source, this condition is violated. Numerical error can be reduced by further discretizing the mesh near the transmitter. However, the forward problem becomes more com-

putationally expensive by doing so. In this section, I propose an algorithm for improving the numerical accuracy without increasing the size of the model space. This is accomplished by flagging cells which are sufficiently close to the transmitter, then replacing their pre-existing geometric sensitivities by a better approximation.

4.3.1 Refinement of Geometric Sensitivities

Improved Approximation of Geometric Sensitivities using Subvolumes

Consider Eq. (4.1) for a single cubic cell with homogenous physical properties; this cell is denoted by k in Figure 4.1a. By using Eq. (4.15) to represent the off-time viscous remanent magnetization within the cell, the VRM response at location P and time t is:

$$\vec{b}(P,t) = \frac{\mu_0}{4\pi}\left[\int_V \nabla\nabla\frac{1}{r}\cdot\vec{H}(Q)\,dV\right]\Delta\chi F(t) \tag{4.39}$$

where $\Delta\chi$ is the zero-frequency magnetic susceptibility for all superparamagnetic grains, $F(t)$ is the after-effect function, and:

$$r = \sqrt{\left(x_P - x_Q\right)^2 + \left(y_P - y_Q\right)^2 + \left(z_P - z_Q\right)^2} \tag{4.40}$$

For this section, $\vec{H}(Q)$ is called the inducing field. For step-off or square-pulse excitation, $\vec{H}(Q)$ is the on-time field. For an arbitrary waveform approximated by a discrete set of square pulses, $\vec{H}(Q)$ represents the inducing field at its maximum amplitude.

In section 4.2.2, I assumed the inducing field throughout the cell was equal to the inducing field at the cell's center. This led to an approximation of the VRM response which was expressed as a linear system. According to Eq. (4.3):

$$\vec{b}(P,t) \approx \left[G\cdot\vec{H}\,\right]\Delta\chi F(t) = \vec{a}\,\Delta\chi F(t) \tag{4.41}$$

where

$$\vec{b}(P,t) = \begin{bmatrix} b_x(P,t) \\ b_y(P,t) \\ b_z(P,t) \end{bmatrix}, \quad G = \begin{bmatrix} g_{xx} & g_{xy} & g_{xz} \\ g_{yx} & g_{yy} & g_{yz} \\ g_{zx} & g_{zy} & g_{zz} \end{bmatrix}, \quad \vec{H} = \begin{bmatrix} H_x \\ H_y \\ H_z \end{bmatrix} \quad \text{and} \quad \vec{a} = \begin{bmatrix} a_x \\ a_y \\ a_z \end{bmatrix} \tag{4.42}$$

H_x, H_y and H_z are cartesian components of the inducing field at the cell's center, and G can be obtained from Bhattacharyya (1964). The approximate geometric sensitivities relating the cell to observation location P are represented by elements a_x, a_y and a_z; true geometric sensitivities would require an analytic solution to the integral in Eq. (4.39). For a collection of cells, and for multiple observation locations, a_x, a_y and a_z ultimately represent three of the vectorial elements which comprise the geometric sensitivity matrix $\mathbf{A}$.

Let us now consider what happens if I divide the cell into $J = 2^{3\lambda}$ equivalent subvolumes (Figure 4.1b). I refer to λ as the refinement factor; where λ = 0, 1, 2 ... has integer values. If the cubic cell is given a side length of h, then each subvolume within the cell has a side length of $h/2^{\lambda}$. From this, I may re-express Eq. (4.39) as a sum

over all subvolumes:

$$\vec{b}(P,t) = \frac{\mu_0}{4\pi}\left[\sum_{j=1}^{J}\int_{V_j}\nabla\nabla\frac{1}{r}\cdot\vec{H}(Q)\,dV\right]\Delta\chi F(t) \tag{4.43}$$

where V_j is the volume of subvolume j. If I assume the inducing field is approximately homogeneous throughout each subvolume, but not necessarily throughout the cell, then:

$$\vec{b}(P,t) \approx \left[\sum_{j=1}^{J} G_j\cdot\vec{H}_j\right]\Delta\chi F(t) = \left[\sum_{j=1}^{J}\vec{a}_j\right]\Delta\chi F(t) \tag{4.44}$$

where $\vec{H}_j$ contains cartesian components of the inducing field at the center of subvolume j, and G_j can be constructed according in Bhattacharyya (1964). Elements within $\vec{a}_j$ contain the approximate geometric sensitivities associated with subvolume j. Eq. (4.44) is analogous to a mid-point Riemann sum for the integral in Eq. (4.39). Therefore, I expect Eq. (4.44) to offer a better approximation of the cell's geometric sensitivities than Eq. (4.41); which only uses one point.

Now consider the forward model derived in section 4.2. According to Eq. (4.38), the forward model is expressed as:

$$\mathbf{d} = \mathbf{T}\mathbf{A}\mathbf{m} \tag{4.45}$$

where $\mathbf{d}$ is the final data vector, $\mathbf{T}$ is the characteristic decay matrix, $\mathbf{m}$ is the model, and $\mathbf{A}$ is known as the geometric sensitivity matrix. For K cells and N observation locations, $\mathbf{A}$ has dimensions $3N \times K$. The approximate geometric sensitivities for cell k comprise the k^{th} column of $\mathbf{A}$; which I will denote as $\mathbf{a_k}$. For cell k (Figure 4.1a),

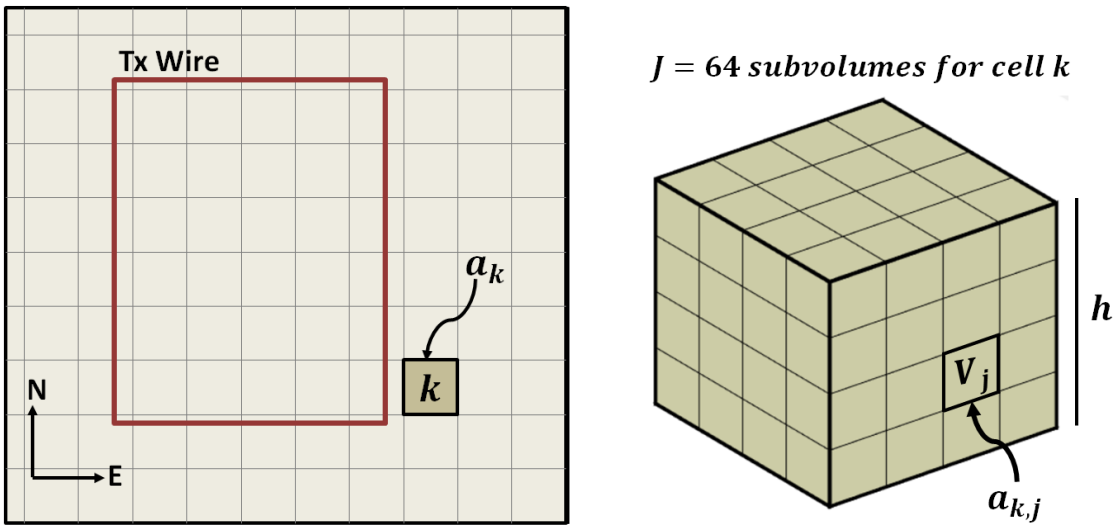

(a) (b)

Figure 4.1: (a) Top view of survey geometry with cell k outlined. The geometric sensitivities of all data to cell k are contained in the k^{th} column of $\mathbf{A}$; which is denoted by $\mathbf{a_k}$. (b) Subdivision of cell k into $J = 2^{3\lambda}$ equal subvolumes. Each subvolume V_j has a vector of geometric sensitivities $\mathbf{a_{k,j}}$ which can be summed to obtain a better approximation of $\mathbf{a_k}$.

located near a controlled source, I may decide the approximate geometric sensitivities $\mathbf{a_k}$ are insufficient. In that case, cell k is divided into $J = 2^{3\lambda}$ equivalent subvolumes. I let $\mathbf{a_{k,j}}$ denote the approximate geometric sensitivities for subvolume j within cell k. Vector $\mathbf{a_{k,j}}$ can be generated in the exact same manner as $\mathbf{a_k}$; except now, a different volume and on-time field are being used. To improve the approximation of the geometric sensitivities for cell k, the k^{th} column of $\mathbf{A}$ simply needs to be replaced by:

$$\mathbf{a_k} = \sum_{j=1}^{J} \mathbf{a_{k,j}} \tag{4.46}$$

Thus, to generate the final geometric sensitivity matrix for the forward problem, I propose the following approach. First, an initial geometric sensitivity matrix $\mathbf{A}$ is constructed according to theory presented in section 4.2. Cells which are too close to the transmitter wire are each divided into $J = 2^{3\lambda}$ subvolumes. A method for locating these cells is discussed in the following section. For all cells which must be subdivided, and for all subvolumes within these cells, vectors $\mathbf{a_{k,j}}$ are generated. For each of these cells, Eq. (4.46) is used to generate an improved approximation of the geometric sensitivities. The new approximate sensitivities are then used to replace pre-existing columns within $\mathbf{A}$. Although the approach does not increase the model space, additional memory is required to store vectors $\mathbf{a_{k,j}}$ for each subvolume.

Locating Cells Near the Transmitter

Consider a controlled source which may be constructed using a set of straight wire segments. For a single segment, with end points (x_1, y_1, z_1) and (x_2, y_2, z_2), I define the following parametric equation for a line:

$$\begin{bmatrix} x \\ y \\ z \end{bmatrix} = \begin{bmatrix} x_2 - x_1 \\ y_2 - y_1 \\ z_2 - z_1 \end{bmatrix} s + \begin{bmatrix} x_1 \\ y_1 \\ z_1 \end{bmatrix} \tag{4.47}$$

where s is defined over the entire real axis. Note that $s \in [0,1]$ is used to represent locations lying along the wire segment. Now consider a cell whose center lies at (x_c, y_c, z_c). If the cell's center is within distance D from the line defined by Eq. (4.47), then there exists two points in which (Figure 4.2):

$$D^2 = \big(s x_2 + (1-s)x_1 - x_c\big)^2 + \big(s y_2 + (1-s)y_1 - y_c\big)^2 + \big(s z_2 + (1-s)z_1 - z_c\big)^2 \tag{4.48}$$

We can see from Figure 4.2, that one of the points which lies distance D from (x_c, y_c, z_c) also lies along the transmitter segment; with some locations along the transmitter segment lying closer than D. This corresponds to a value of $s \in [0,1]$. Thus, the geometric sensitivities of this cell should be replaced. I can re-express Eq. (4.48) as a quadratic equation in terms of s:

$$As^2 + Bs + C = 0 \tag{4.49}$$

where

$$A = (x_2 - x_1)^2 + (y_2 - y_1)^2 + (z_2 - z_1)^2 \tag{4.50}$$

$$B = 2(x_2 - x_1)(x_1 - x_c) + 2(y_2 - y_1)(y_1 - y_c) + 2(z_2 - z_1)(z_1 - z_c) \tag{4.51}$$

$$C = (x_1 - x_c)^2 + (y_1 - y_c)^2 + (z_1 - z_c)^2 - D^2 \tag{4.52}$$

The solution to Eq. (4.49) is:

$$s_{\pm} = \frac{-B \pm \sqrt{B^2 - 4AC}}{2A} \tag{4.53}$$

which provides two values, s_- and s_+. Evaluation of Eq. (4.53) for a given cell can result in one of four cases:

$$\begin{aligned} &\text{Case 1: } \{s_+, s_-\} \in \mathbb{R} \text{ with } s_- \text{ or } s_+ \in [0,1] \\ &\text{Case 2: } \{s_+, s_-\} \in \mathbb{R} \text{ with } s_- < 0 \text{ and } 1 < s_+ \\ &\text{Case 3: } \{s_+, s_-\} \in \mathbb{R} \text{ with } s_-, s_+ < 0 \text{ or } s_-, s_+ > 1 \\ &\text{Case 4: } \{s_+, s_-\} \in \mathbb{C} \end{aligned} \tag{4.54}$$

For case 1, there is at least one location along the wire segment which is distance D from (x_c, y_c, z_c). This is shown in Figure 4.2. For case 2, all locations along the transmitter segment (represented by $s \in [0,1]$) are less than distance D from (x_c, y_c, z_c). This only occurs if the transmitter segment is shorter than D. For case 3, (x_c, y_c, z_c) is sufficiently close to the parametric line, but not the transmitter segment. And for case 4, there are no locations along the parametric line that are distance D from (x_c, y_c, z_c); implying there are no locations along the transmitter segment. Therefore, if cases 1 or 2 are satisfied for a given cell, the sensitivities are replaced in matrix $\mathbf{A}$.

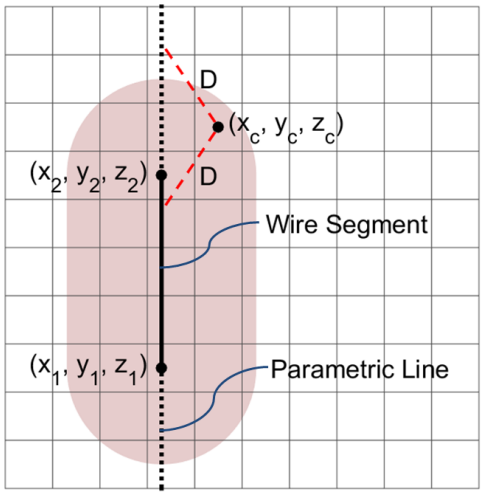

Figure 4.2: Geometry for determining cell centers which lie within distance D of a given transmitter segment (red region). These cell centers will have exactly 2 locations along the parametric line which are at distance D.

For each wire segment comprising the transmitter, Eq. (4.53) is used to identify cells which are in sufficiently close proximity. Eq. (4.46) then computes a new set of geometric sensitivities for each cell. These geometric sensitivities are then used to replace columns in **A**. To limit computer memory requirements, this three step process is performed independently for each wire segment. However, book-keeping is done to ensure redundant computations are not performed for cells which lie sufficiently close to multiple wire segments.

Geometric Sensitivity Refinement Algorithm

When predicting the VRM response for synthetic cases, I may want to apply decreasing levels of refinement $\lambda_1 > \lambda_2 > \lambda_3 > ...$ at increasing distances $D_1 < D_2 < D_3 < ...$ from the transmitter. To accomplish this, the algorithm performs a set of operations independently for each wire segment. Book-keeping is done to ensure redundant calculations are not performed on cells whose sensitivities have already been replaced by a better approximation. For a given wire segment, cells within distance D_1 are found by computing $s_{\pm}$. Each of these cells are divided into $2^{3\lambda_1}$ subvolumes. Eq. (4.46) is then used to better approximate the geometric sensitivities $\mathbf{a_k}$ for these cells; which are used to replaced pre-existing columns within **A**. This process is then repeated for D_2, D_3, and so forth, before moving on to the next wire segment. The algorithm for generating and refining **A** is illustrated below.

Algorithm 1 Refinement of Geometric Sensitivities

Require: $\lambda_1 > \lambda_2 > \lambda_3 > ...$ and $D_1 < D_2 < D_3 < ...$
- Generate initial **A** matrix
for all transmitter segments **do**
  for $n = 1, 2, 3, ...$ **do**
    - Compute $\mathbf{s}_{\pm}$ for all cells using distance D_n
    for all cells satisfying cases 1 or 2 in Eq. (4.54) **and not** already refined using some factor $\lambda \geq \lambda_n$ **do**
      - Approximate geometric sensitivities $\mathbf{a_k}$ vectors using $2^{3\lambda_n}$ subvolumes
      - Replace the appropriate columns within **A**
    end for
  end for
end for

4.3.2 Convergence of the Sensitivity Refinement Algorithm

For cells located near a controlled source, the sensitivity refinement algorithm presented in section 4.3.1 can be used to minimize associated numerical errors. In this section, a homogeneous block is used to examine the convergence of the VRM3D code as a function of the refinement factor. Results can be used to determine the refinement needed to accurately predict VRM responses using synthetic models.

The sensitivity of predicted data to the geometry of the forward problem is contained in **A**; whereas the characteristic decay of the response is contained in **T**. Thus for the off-time VRM response, convergence of the forward model depends on convergence of the following vector:

$$\mathbf{v} = \mathbf{A}\,\mathbf{m} \tag{4.55}$$

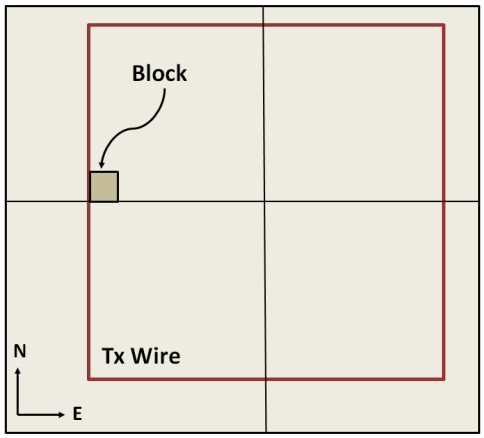

Figure 4.3: Illustration showing a magnetically viscous block located along the edge of a square transmitter loop. For the test problem, the block has a side length of 2 m, and the transmitter loop is given a side length of 40 m.

where $\mathbf{A}$ is the geometric sensitivity matrix and $\mathbf{m}$ is the model. Let $\mathbf{v}^{\lambda}$ be the vector predicted using mesh refinement p, and let $\mathbf{v}^{t}$ represent an analytic solution to the problem. The errors ε^{λ} associated with $\mathbf{v}^{\lambda}$ are defined by:

$$\mathbf{v}^{\lambda} = \mathbf{v}^{t} + \varepsilon^{\lambda} \tag{4.56}$$

Because an analytic solution does not exist for the test problem, I cannot directly show that $\mathbf{v}^{\lambda}$ converges to $\mathbf{v}^{t}$ as $\lambda \to \infty$. Instead, I define the following vector:

$$\mathbf{u}^{\lambda} = \mathbf{v}^{\lambda} - \mathbf{v}^{\lambda-1} = \varepsilon^{\lambda} - \varepsilon^{\lambda-1} \tag{4.57}$$

where $\mathbf{u}^{\lambda}$ is a relative difference in errors for the current refinement factor λ and the previous one $\lambda - 1$. From Eq. (4.57), I assume that as $\lambda \to \infty$, $\mathbf{v}^{\lambda}$ approaches the analytic solution; or at the very least, ε^{λ} converges to something sufficiently small. In either case:

$$\lim_{\lambda \to \infty} \mathbf{u}^{\lambda} = \vec{\mathbf{0}} \tag{4.58}$$

where $\vec{\mathbf{0}}$ is a column vector of all zeros. Convergence of the numerical solution is therefore inferred when the elements of $\mathbf{u}$ are sufficiently small. Another way to quantify this is by taking the various norms of $\mathbf{u}$ for increasing values of λ. For refinement factor λ, I define the L_1, L_2 and L_∞ norms of $\mathbf{u}$ as follows:

$$\left\| \mathbf{u}^{\lambda} \right\|_1 = \left\| \mathbf{v}^{\lambda} - \mathbf{v}^{\lambda-1} \right\|_1 = \sum_{i=1}^{N} \left| v_i^{\lambda} - v_i^{\lambda-1} \right| \tag{4.59}$$

$$\left\| \mathbf{u}^{\lambda} \right\|_2 = \left\| \mathbf{v}^{\lambda} - \mathbf{v}^{\lambda-1} \right\|_2 = \left[\sum_{i=1}^{N} \left| v_i^{\lambda} - v_i^{\lambda-1} \right|^2 \right]^{1/2} \tag{4.60}$$

$$\left\| \mathbf{u}^{\lambda} \right\|_\infty = \left\| \mathbf{v}^{\lambda} - \mathbf{v}^{\lambda-1} \right\|_\infty = \max_i \left\{ \left| v_i^{\lambda} - v_i^{\lambda-1} \right| \right\} \tag{4.61}$$

where i refers to an element within $\mathbf{v}^{\lambda}$, and N is the total number of elements. From Eq. (4.59), the L_1 norm

represents the average amount in which elements within $\mathbf{v}$ are changing as λ is increased. And according to Eq. (4.61), the L_∞ norm represents the maximum change in any element.

The product of $\mathbf{A}\,\mathbf{m}$ in Eq. (4.55) may split into 3 vectors:

$$\mathbf{v} = \begin{bmatrix} \mathbf{v_x} \\ \mathbf{v_y} \\ \mathbf{v_z} \end{bmatrix} \tag{4.62}$$

where $\mathbf{v_x}$, $\mathbf{v_y}$ and $\mathbf{v_z}$ are vectors associated with each cartesian component of the VRM response. For the analysis, Eqs. (4.58), (4.59), (4.60) and (4.61) are used to observe the convergence of each component separately.

To test the convergence of the forward problem, a square transmitter loop of side length 40 m, centered at the origin, was placed on the Earth's surface. A magnetically viscous cube of side length 2 m, centered at (X,Y,Z) = (-19 m, 1 m , -1 m), was then placed in proximity of the transmitter. This test problem represents a worst case scenario, given that one of the edges of the cube is actually touching the transmitter wire (Figure 4.3). Magnetic properties: $\Delta\chi$ = 0.05, $\tau_1 = 10^{-6}$ s and τ_2 = 1 s were given to the cube. Using increasingly large refinement factors, $\mathbf{v_x}$, $\mathbf{v_y}$ and $\mathbf{v_z}$ were predicted at N = 3721 locations near the cube, at a height 0.5 m above the ground. The refinement factors and subsequent number of subvolumes within the block are shown in Table 4.1. The side length of each subvolume is given by $h/2^\lambda$.

λ	$h/2^\lambda$	# Subvolumes
0	2 m	1
1	1 m	8
2	0.5 m	64
3	0.25 m	512
4	0.125 m	4,096
5	0.0625 m	32,768

Table 4.1: Table showing the refinement factors λ, subvolume widths, and the total number of subvolumes for the convergence test.

For λ = 0, λ = 3 and λ = 5, $\mathbf{v_x}$, $\mathbf{v_y}$ and $\mathbf{v_z}$ are shown in Figure 4.4. As λ was increased from 0 (no refinement) to 3, $\mathbf{v}$ began to generate a more compact anomaly. In addition, the maximum amplitudes of $\mathbf{v_x}$, $\mathbf{v_y}$ and $\mathbf{v_z}$ increased. For $\mathbf{v_x}$, the region of maximum amplitude began to align itself along the path of the transmitter wire. This makes sense given that magnetization should be strongest in proximity of the wire. Similar behaviours can be seen for $\mathbf{v_y}$ and $\mathbf{v_z}$. For $\lambda > 3$, the overall shape of the $\mathbf{v}$ anomaly did not change significantly as λ was increased; however, differences were still measurable in certain locations. In Figure 4.5, $\mathbf{u_x}$, $\mathbf{u_y}$ and $\mathbf{u_z}$ are shown for λ = 4. Within 0.5 m of the transmitter wire, I see that elements within $\mathbf{v_x}$, $\mathbf{v_y}$ and $\mathbf{v_z}$ are changing as λ is increased; whereas outside this area, changes are minimal. This implies that subvolumes adjacent to the wire are not small enough to accurately characterize the inducing field within the block. However, because the anomaly at sufficient distance from the wire is less impacted by these subvolumes, the associated error is reduced. The L_1, L_2 and L_∞

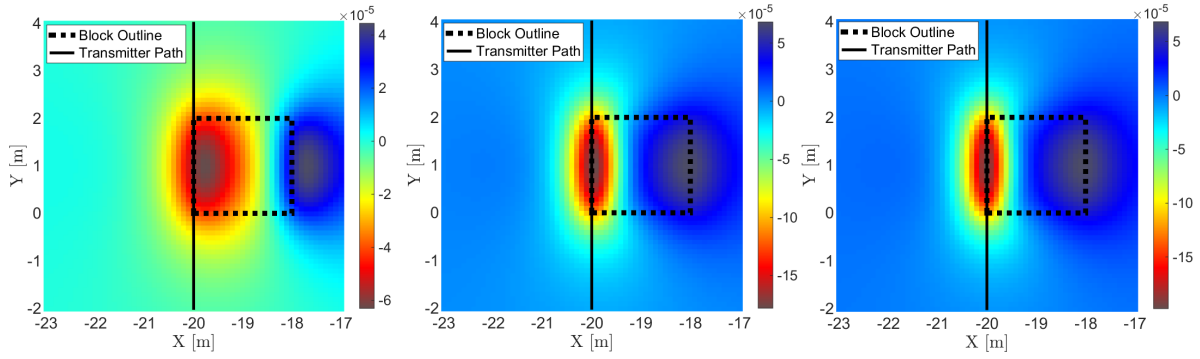

(a) $\mathbf{v_x}$ for $h/2^{\lambda} = 2$ m **(b)** $\mathbf{v_x}$ for $h/2^{\lambda} = 0.25$ m **(c)** $\mathbf{v_x}$ for $h/2^{\lambda} = 0.0625$ m

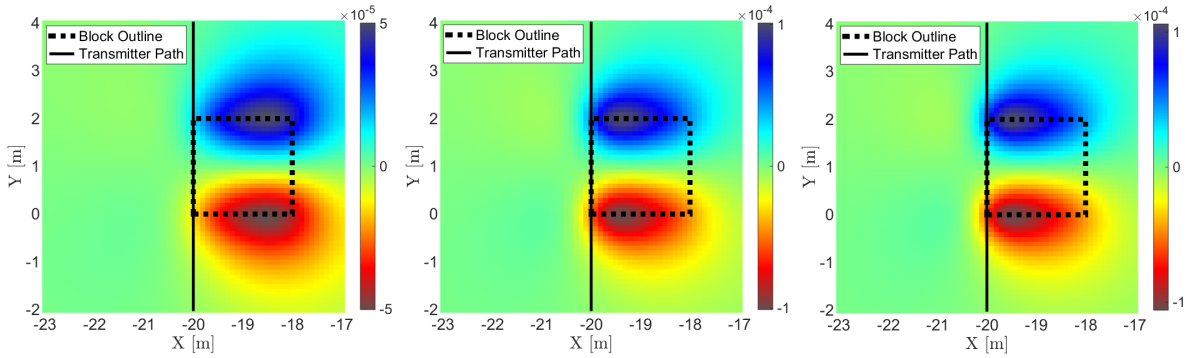

(d) $\mathbf{v_y}$ for $h/2^{\lambda} = 2$ m **(e)** $\mathbf{v_y}$ for $h/2^{\lambda} = 0.25$ m **(f)** $\mathbf{v_y}$ for $h/2^{\lambda} = 0.0625$ m

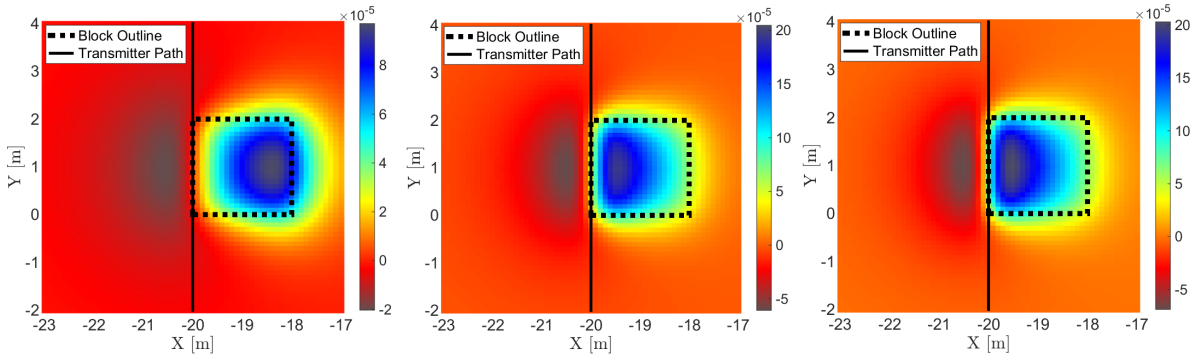

(g) $\mathbf{v_z}$ for $h/2^{\lambda} = 2$ m **(h)** $\mathbf{v_z}$ for $h/2^{\lambda} = 0.25$ m **(i)** $\mathbf{v_z}$ for $h/2^{\lambda} = 0.0625$ m

Figure 4.4: $\mathbf{v_x}$, $\mathbf{v_y}$ and $\mathbf{v_z}$ at height 0.5 m above the ground for $\lambda = 0$, $\lambda = 3$ and $\lambda = 5$. A dashed line is used to outline the margins of a block with side length 2 m. A solid line is used to represent the path of the transmitter wire. The subvolumes width is given by $h/2^{\lambda}$.

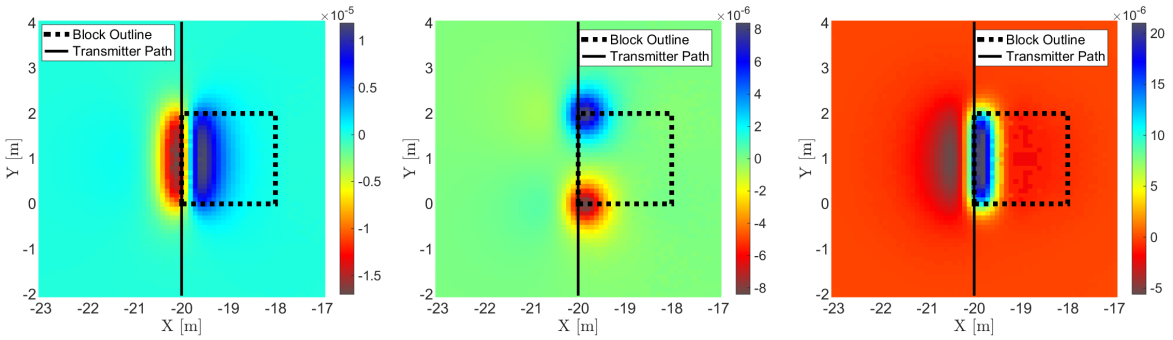

(a) $\mathbf{u_x}$ for $\lambda = 4$ **(b)** $\mathbf{u_y}$ for $\lambda = 4$ **(c)** $\mathbf{u_z}$ for $\lambda = 4$

Figure 4.5: $\mathbf{u_x}$, $\mathbf{u_y}$ and $\mathbf{u_z}$ for $\lambda = 4$. A dashed line is used to outline the margins of a block with side length 2 m. A solid line is used to represent the path of the transmitter wire. This figure shows that $\mathbf{v}$ changes most near the transmitter wire as λ is increased. Away from the transmitter, changes are minimal.

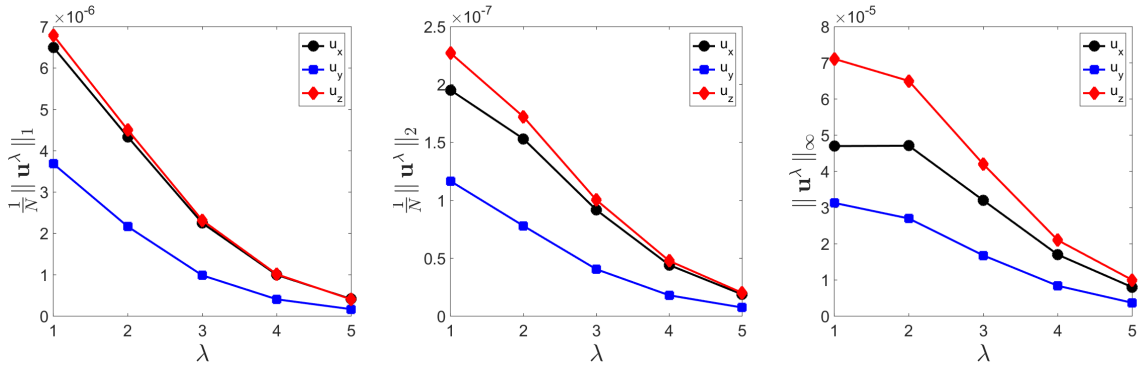

(a) **(b)** **(c)**

Figure 4.6: Convergence of $\mathbf{u}$ in L_1, L_2 and L_∞ norms, as a function of the mesh refinement factor λ. For the L_1 and L_2 norms, values were normalized by the total number of elements in $\mathbf{u_x}$, $\mathbf{u_y}$ and $\mathbf{u_z}$, respectively.

norms of $\mathbf{u_x}$, $\mathbf{u_y}$ and $\mathbf{u_z}$, as a function of λ, are shown in Figure 4.6. The L_1 and L_2 norms were normalized by the total number of elements in $\mathbf{u_x}$, $\mathbf{u_y}$ and $\mathbf{u_z}$, respectively. When the side length of subvolumes was decreased by a factor of 2, $\mathbf{u_x}$, $\mathbf{u_y}$ and $\mathbf{u_z}$ decreased by a factor of 2 in all three norms; indicating convergences of order $O(h)$.

By examining Figures 4.4 and 4.5, I determined that if observations were made at least 0.5 m from the wire, using $\lambda = 4$ instead of $\lambda = 3$ would change the elements in $\mathbf{v}$ by at most 10 %. Improved accuracy can be obtained by using a higher mesh refinement factor, however, the problem becomes much more computationally intensive for $\lambda \geq 4$; especially if the number of cells being refined is sufficiently large. As a result of the analysis, I suggest a subvolume width of 0.25 m be used on all cells which are touching the transmitter wire. For cells with a side width of 2 m, this is obtained using a mesh refinement factor of $\lambda = 3$.

4.4 Validation of the Forward Modeling Scheme Against EM1DTM

Here, the VRM3D code is validated against the UBC EM1DTM code. For comparison, a square transmitter loop of side length 30 m was placed on the Earth's surface. The $\partial\vec{b}(t)/\partial t$ response for step-off excitation was then modeled using a magnetically viscous layer. This layer was extended from the surface to a maximum depth of 6 m and given physical properties: $\Delta\chi = 0.05$, $\tau_1 = 10^{-6}$ s and $\tau_2 = 1$ s. A cell size of 2 m was used to discretize the layer. Cells within 2 m of the transmitter wire were assigned a mesh refinement factor of $\lambda = 3$; resulting in a subvolume width of 0.25 m. The adjacent layer of cells was given a mesh refinement factor of 2, followed by a refinement factor of 1 for the 3rd layer of cells.

A comparison between responses predicted using each code can be seen in Figure 4.7a. For $\tau_1 \ll t \ll \tau_2$, both codes showed excellent agreement. As expected, the VRM3D code was unable to accurately predict the response at very early or very late times, and overestimates the response. This is due to the approximation of the rate of decay for the VRM response. Therefore, the VRM3D code is limited by the range of time relaxation constants which characterize the magnetic viscosity.

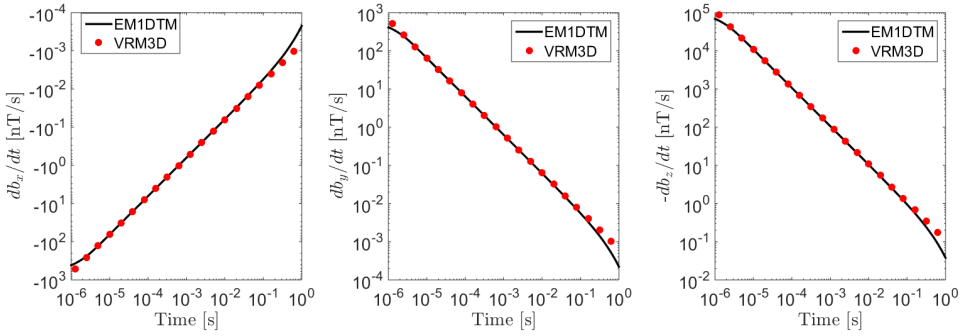

(a)

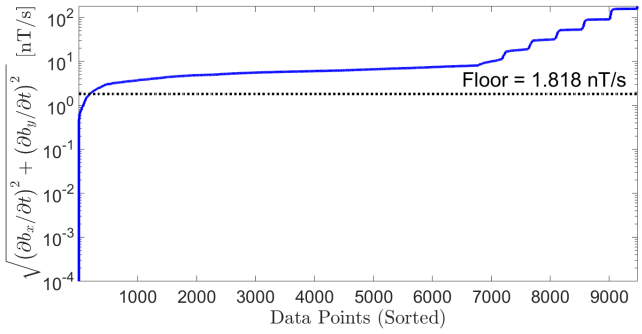

(b)

Figure 4.7: (a) Comparison between EM1DTM and VRM3D for a magnetically viscous layer at X = -10 m, Y = 10 m and Z = 1 m. The layer was extended 6 m below the Earth's surface and was given physical properties $\Delta\chi = 0.05$, $\tau_1 = 10^{-6}$ s and $\tau_2 = 1$ s. Codes show good agreement for $\tau_1 \ll t \ll \tau_2$. VRM3D overestimates the response at very early and very late times. (b) Floor uncertainty value for comparison at 1 ms. Plot shows the magnitude of the horizontal component of the response, sorted by size. ε_{floor} = 1.818 nT/s is the threshold value for the smallest 2%.

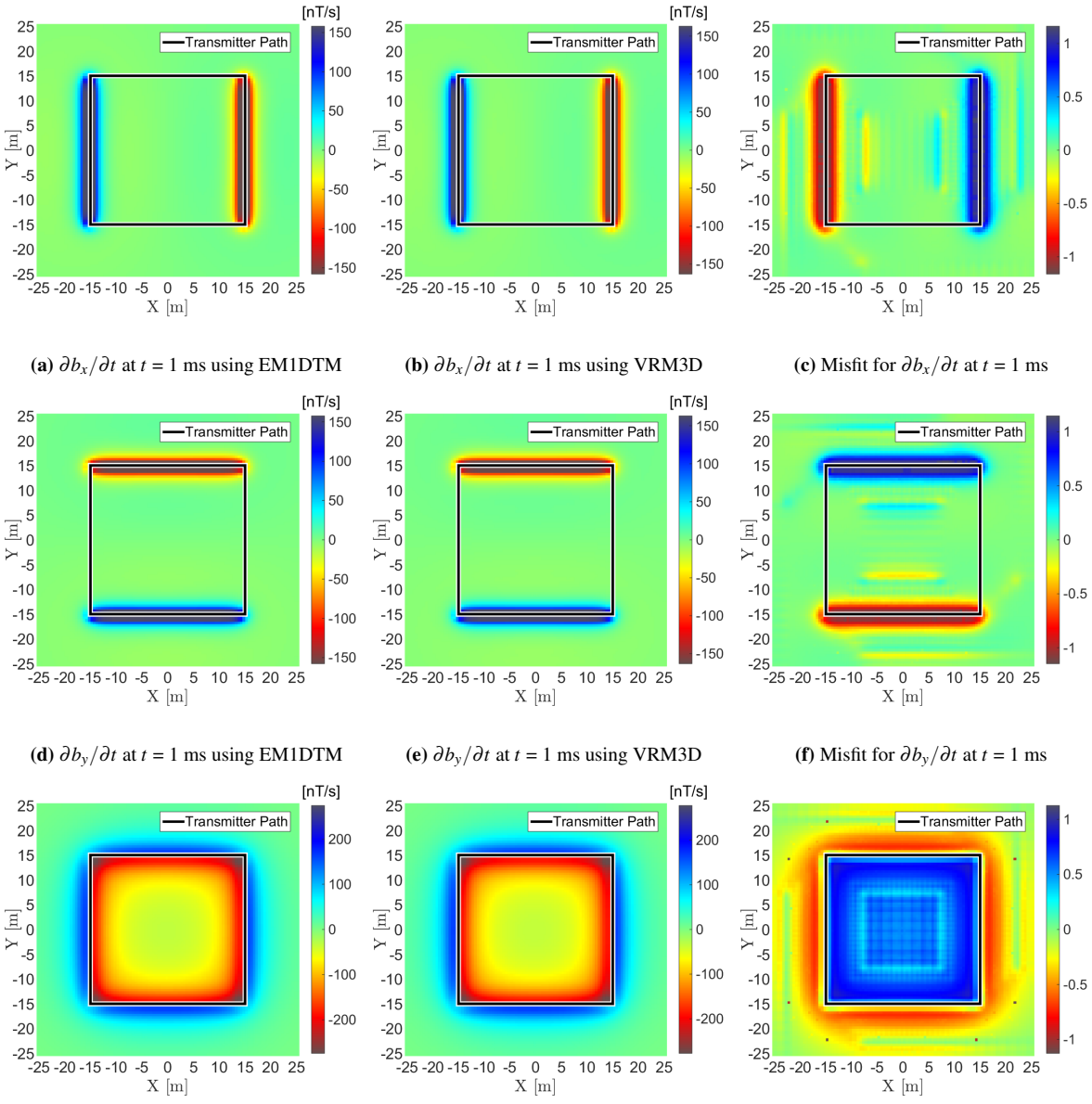

(a) $\partial b_x/\partial t$ at t = 1 ms using EM1DTM

(b) $\partial b_x/\partial t$ at t = 1 ms using VRM3D

(c) Misfit for $\partial b_x/\partial t$ at t = 1 ms

(d) $\partial b_y/\partial t$ at t = 1 ms using EM1DTM

(e) $\partial b_y/\partial t$ at t = 1 ms using VRM3D

(f) Misfit for $\partial b_y/\partial t$ at t = 1 ms

(g) $\partial b_z/\partial t$ at t = 1 ms using EM1DTM

(h) $\partial b_z/\partial t$ at t = 1 ms using VRM3D

(i) Misfit for $\partial b_z/\partial t$ at t = 1 ms

Figure 4.8: Components of $\partial \vec{b}/\partial t$ at t = 1 ms, predicted by both the EM1DTM and VRM3D codes. Also included are the relative data misfits for each component according to Eq. (4.63). Uncertainties were determined by using a 2 % error on data predicted by the EM1DTM code, and a floor of ε_{floor} = 1.818 nT/s.

To compare the relative data misfit between the VRM3D and EM1DTM codes, data were predicted at t = 1 ms, 1 m above the ground, using 0.5 m spacing within $X \in$ [-25 m, 25 m] and $Y \in$ [-25 m, 25 m]. For the numerical experiment, the relative data misfit for datum i was defined by:

$$\phi_i = \frac{d_i^{(1D)} - d_i^{(3D)}}{\varepsilon_i} \tag{4.63}$$

where $d_i^{(1D)}$ represents a datum predicted by EM1DTM, $d_i^{(3D)}$ represents a datum predicted by VRM3D, and ε_i is the uncertainty value for datum i. The uncertainty for datum i is defined by the following expression:

$$\varepsilon_i = C\left|d_i^{(1D)}\right| + \varepsilon_{floor} \tag{4.64}$$

where $0 \leq C \leq 1$ is a fractional percent, and ε_{floor} is a floor uncertainty value. Using EM1DTM, the floor uncertainty was obtained by calculating the magnitude of the total horizontal response $\left(=\sqrt{|\partial B_x/\partial t|^2 + |\partial B_y/\partial t|^2}\right)$. ε_{floor} is the threshold value for the smallest 2%, and is equal to 1.818 nT/s (Figure 4.7b). C = 0.02 was used to represent a percent error of 2%. Thus, if data predicted using the EM1DTM and VRM3D codes vary by 2%, I expect the associated data misfit to provide values of $\phi_i = \pm 1$. For misfit values which lie within $\phi_i \in (-1, 1)$, VRM3D was able to predicted the VRM response within a 2% error.

Figure 4.8 shows predicted data at 1 ms using each code, as well as the data misfits at all locations. When compared to EM1DTM, the VRM3D code appears to underestimate the magnitude of the VRM response slightly. For reasons demonstrated in Section 4.3.2, the areas of largest misfit are near the transmitter wire. However, as long as the response is being predicted at least 2 m from the transmitter wire, the uncertainty will fall within $\pm$ 0.5. Therefore, the VRM3D code is capable of accurately predicting the VRM response at practically all locations.

4.5 Summary

In this chapter, I presented a linear forward modeling scheme for predicting the VRM response from three dimensional bodies. This was accomplished by summing the contributions made by a discrete set of homogeneously magnetized rectangular cells. By approximating the characteristic decay of the VRM response, I was able to predict the off-time VRM response using a compact linear system. I showed that an increase in numerical accuracy could be obtained using a geometric sensitivity refinement strategy which does not increase the size of the model space. Numerical tests showed excellent agreement between EM1DTM and VRM3D, so long as observations are made over an appropriate interval of times. Now that I have constructed a forward model for predicting the VRM response, I can turn my attention towards recovering the distribution of magnetically viscous bodies through geophysical inversion.

Chapter 5

Inverting VRM Data

5.1 Introduction

Inversion has becomes an important tool for solving many geophysical problems. Using this technique, the distribution of physical properties characterizing a geological region can be obtained from a set of TEM survey measurements. If required, the recovered physical property distribution can then be used to predict the Earth's TEM response at other locations or time channels. In this thesis, I develop an inversion methodology for the off-time VRM response for two reasons. First, I am interested in recovering the distribution of magnetically viscous materials within a lateritic topsoil. More importantly however, I am interested in using the predicted data from a recovered model to remove the contaminating VRM signal from a set of TEM data.

Following the work of Tikhonov and Arsenin (1977), I formulate the VRM inversion as a regularized least-squares (RLSQ) optimization problem. The inversion methodology is then used to recover the amalgamated magnetic property distribution for a viscous topsoil. Here, I assume that data being inverted are at sufficiently late times, and that I may the neglect any contribution by the Earth's inductive response. The inversion methodology is tested for several transmitter-receiver configurations. Finally, I describe a workflow for removing the VRM signal from a set of TEM data.

5.2 Least-Squares Inversion Approach

5.2.1 Introduction to Regularized Least-Squares Inversion

In Chapter 4, I presented a linear forward modeling operator for predicting the off-time VRM response from a collection of remanently magnetized cubic volumes. More generally, the forward problem may be expressed as follows:

$$\mathbf{d} = \mathbb{F}[\mathbf{m}] \tag{5.1}$$

where $\mathbb{F}$ defines an explicit relationship between the geophysical data $\mathbf{d}$, and the set of model parameters $\mathbf{m}$ for a physical system. When considering viscous remanent magnetization, elements of $\mathbf{m}$ represent the amalgamated

magnetic property for each cell. Frequently, we are interested in solving the inverse problem:

$$\mathbf{m} = \mathbb{F}^{-\mathbf{1}}[\mathbf{d}] \tag{5.2}$$

wherein we attempt to recover the model parameters which are responsible for a set of field observations. Obtaining a solution to the inverse problem is non-trivial, as the problem is frequently ill-posed. In most geophysical applications, the number of model parameters far exceeds the number of field observations. This results in a solution which is highly non-unique. In addition, field data are generally impacted by random noise $\mathbf{e}$ from unknown sources. Thus, it may be more appropriate to represent the forward problem as follows:

$$\begin{aligned} \mathbf{d}^{\mathbf{obs}} &= \mathbb{F}[\mathbf{m}] \\ \mathbf{d}^{\mathbf{obs}} &= \mathbf{d} + \mathbf{e} \end{aligned} \tag{5.3}$$

where $\mathbf{d}^{\mathbf{obs}}$ represents a set of field observations. Consider the case where $\mathbb{F}$ is a linear operator. Even if the matrix is full-rank and invertible, the inverse problem may still be ill-conditioned. For many geophysical problems, solutions to Eq. (5.2) are unstable. Thus, small changes in the noise may produce large changes in the values of recovered model parameters.

Solutions to Eq. (5.2) are likely to produce an infinite set of models which are both geologically unrealistic, and unstable with respect to the observed data. Following the method proposed by Tikhonov and Arsenin (1977), the inverse problem may be formulated in terms of a regularized least-squares problem:

$$\begin{aligned} \min_{\mathbf{m}} \phi(\mathbf{m}) \\ \phi(\mathbf{m}) &= \phi_d + \beta \phi_m \\ \phi_d &= \left\| \mathbf{W_d} \left(\mathbb{F}[\mathbf{m}] - \mathbf{d}^{\mathbf{obs}} \right) \right\|_2^2 \\ \phi_m &= \left\| \mathbf{Rm} \right\|_2^2 \end{aligned} \tag{5.4}$$

where the optimum solution minimizes a global object function $\phi(\mathbf{m})$. The data misfit ϕ_d quantifies a scaled residual between the predicted data for a given model $\mathbb{F}[\mathbf{m}]$ and the observed data $\mathbf{d}^{\mathbf{obs}}$. By assuming the noise are normally distributed and uncorrelated for each datum, $\mathbf{W_d}$ is defined as follows:

$$\mathbf{W_d} = \begin{bmatrix} 1/\sigma_1 & 0 & \dots & 0 \\ 0 & 1/\sigma_2 & & \vdots \\ \vdots & & \ddots & 0 \\ 0 & \dots & 0 & 1/\sigma_N \end{bmatrix} \tag{5.5}$$

where σ_i is an estimate of the standard deviation, or uncertainty, for datum i. The data misfit therefore follows a chi-squared distribution with an expected value of N; where N is the number of data.

The model objective function ϕ_m stabilizes the inverse problem and constrains the solution. Constraints and a-priori information may be implemented by adapting the regularization term $\mathbf{R}$. The trade-off parameter β bal-

ances the relative contributions made by the data misfit and the model objective function. Designing a model objective function for the VRM problem is discussed in Section 5.2.3.

The solution to the least-squares problem occurs when all partial gradients of the global objective function are zero:

$$\nabla\phi(\mathbf{m}) = \mathbf{0} \tag{5.6}$$

By taking the gradient of Eq. (5.4) with respect to the model parameters:

$$\mathbf{J^T W_d^T W_d}\left[\mathbb{F}[\mathbf{m}] - \mathbf{d^{obs}}\right] + \beta\mathbf{R^T R m} = \mathbf{0} \tag{5.7}$$

where $\mathbf{J}$ is the Jacobian of the forward modeling operator:

$$\mathbf{J} = \frac{\partial\mathbb{F}[\mathbf{m}]}{\partial\mathbf{m}} \tag{5.8}$$

The Jacobian represents the sensitivity of the data to changes in the model parameters. For unbounded, linear least-squares problems, the solution to Eq. (5.4) may be obtained directly by solving Eq. (5.7). However, when bound constraints are added to the model, the problem becomes non-linear. For a more general approach, second-order methods can be used to obtain the solution iteratively. Newton's method updates the set of model parameters by solving the following linear system at each iteration j:

$$\mathbf{H}\,\delta\mathbf{m} = -\nabla\phi(\mathbf{m^{(j)}}) \tag{5.9}$$

where $\mathbf{H}$ is the Hessian, or second order derivative, of the global objective function:

$$\mathbf{H} = \frac{\partial^2\phi}{\partial\mathbf{m}^2} \tag{5.10}$$

and $\delta\mathbf{m}$ defines the model update direction. The model is updated at each iterations as follows:

$$\mathbf{m^{(j+1)}} = \mathbf{m^{(j)}} + \alpha\delta\mathbf{m} \tag{5.11}$$

where α is a step-length which scales the model perturbation $\delta\mathbf{m}$. Using the linear forward modeling operator given by Eq. (4.38), the model update direction corresponding to Eq. (5.4) is given by:

$$\left[\mathbf{A^T T^T W_d^T W_d T A} + \beta\mathbf{R^T R}\right]\delta\mathbf{m} = -\mathbf{A^T T^T W_d^T W_d}(\mathbf{T A\,m} - \mathbf{d^{obs}}) - \beta\mathbf{R^T R m} \tag{5.12}$$

where superscript j has been suppressed. Iterative methods such as Newton's method are typically carried out until a stopping criteria is reached. Note that computation of the gradient and Hessian depend on the characteristic decay matrix $\mathbf{T}$; which was defined in Eq. (4.38). The number of rows in $\mathbf{T}$ increases linearly in proportion to the number of time channels. Eq. (5.12) results directly from the definition of the data misfit. A more appropriate measure of a model's ability to fit the set of field observations is presented in Section 5.2.2. An approach for computing the model update and step-length for a given β is presented in Section 5.2.4.

5.2.2 Collapsed Data Misfit for the VRM Inverse Problem

The data misfit provides a measure of how well a particular model is able to reproduce a set of field observations. For RLSQ inverse problems, a widely accepted representation of the data misfit was proposed in Section 5.2 (Tikhonov and Arsenin, 1977). In this thesis however, I explore a misfit which is formulated by collapsing the observed data vector into a more compact representation. By implementing a collapsed data misfit, I intend to render the problem less over-determined and reduce memory requirements associated with the inverse problem.

According to Eqs. (4.33) and (4.38), the predicted VRM response at time t is given by:

$$\mathbf{d}(t) = \eta(t)\mathbf{A}\,\mathbf{m} \tag{5.13}$$

where $\eta(t)$ is the characteristic decay function and $\mathbf{d}(t)$ represents predicted data at time t. Therefore, the VRM response at time t is predicted by scaling the product of $\mathbf{Am}$ by the characteristic decay function. Over the range of times in which $\eta(t)$ accurately characterizes the decay of the VRM response:

$$\frac{\mathbf{d}(t_1)}{\eta(t_1)} = \frac{\mathbf{d}(t_2)}{\eta(t_2)} = \mathbf{A}\mathbf{m} \tag{5.14}$$

Eq. (5.14) implies that predicted data at t_1 can be used directly to predict data at time t_2, and visa versa. Therefore, data at t_1 and t_2 provide identical information pertaining to the model I hope to recover. For M time channels, I define the following vector:

$$\mathbf{q} = \frac{1}{M}\sum_{m=1}^{M}\frac{\mathbf{d}(t_m)}{\eta(t_m)} = \mathbf{A}\,\mathbf{m} \tag{5.15}$$

where $\mathbf{q}$ is a time-weighted average of the predicted data for all locations. As I mentioned in Section 5.2.1, field observations are generally impacted by random noise from unknown sources. Where $\mathbf{e}(t)$ is a vector representing the data errors for all locations at time t:

$$\mathbf{q}^{\mathbf{obs}} = \frac{1}{M}\sum_{m=1}^{M}\frac{\mathbf{d}^{\mathbf{obs}}(t_m)}{\eta(t_m)} = \frac{1}{M}\sum_{m=1}^{M}\frac{\mathbf{d}(t_m)+\mathbf{e}(t_m)}{\eta(t_m)} = \mathbf{q} + \frac{1}{M}\sum_{m=1}^{M}\frac{\mathbf{e}(t_m)}{\eta(t_m)} \tag{5.16}$$

where $\mathbf{q}^{\mathbf{obs}}$ is a time-weighted average of the observed data for all locations, and $\widetilde{\mathbf{e}}$ is the time-weighted average of the data errors for all locations:

$$\widetilde{\mathbf{e}} = \frac{1}{M}\sum_{m=1}^{M}\frac{\mathbf{e}(t_m)}{\eta(t_m)} \tag{5.17}$$

In Section 5.2.1, I assumed the data errors associated with each individual datum $d_i(t_m)$ were uncorrelated and normally distributed; where i refers to an observation location and m refers to a specific time channel. As a result, the time-weighted average of data errors $\widetilde{e}_i \in \widetilde{\mathbf{e}}$ at location i must also belong to a normal distribution. Let $\sigma_i(t_m)$ represents the standard deviation corresponding to the data error $e_i(t_m)$ at location i and time t_m. The standard

deviation corresponding to time-weighting average error $\widetilde{e}_i$ is given by:

$$\widetilde{\sigma}_i = \frac{1}{M}\left[\sum_{m=1}^{M}\left(\frac{\sigma_i(t_m)}{\eta(t_m)}\right)^2\right]^{1/2} \tag{5.18}$$

where $\widetilde{\sigma}_i$ is defined as the time-weighted standard deviation at location i. In examining Eq. (5.18), there are several interesting cases:

• *Case 1*: The data errors at each time channel impact $\mathbf{q}^{\mathbf{obs}}$ to roughly the same degree; i.e. $\sigma_i(t_m) \approx \eta(t_m)\bar{\sigma}$, and:

$$\widetilde{\sigma}_i \approx \frac{\bar{\sigma}}{\sqrt{M}} \tag{5.19}$$

Therefore, the time-weighted standard deviation at each location decreases proportional to $\sqrt{M}$. This implies that uncertainties on $\mathbf{q}^{\mathbf{obs}}$ can be reduced by using more time channels.

• *Case 2*: The data errors at each time channel have roughly the same standard deviation; i.e. $\sigma_i(t_m) \approx \bar{\sigma} \ \forall \ m$, and:

$$\widetilde{\sigma}_i \approx \frac{\bar{\sigma}}{M}\left[\sum_{m=1}^{M}\left(\frac{1}{\eta(t_m)}\right)^2\right]^{1/2} \leq \frac{\bar{\sigma}}{\sqrt{M}}\max\left(\frac{1}{\eta(t_m)}\right) \tag{5.20}$$

In this case, the time-weighted standard deviation is most impacted by time channels in which $1/\eta(t_m)$ is very large. However, the time-weighted standard deviation is bounded by a value inversely proportional to $\sqrt{M}$. Therefore, I expect to see a reduction in data uncertainty on $\mathbf{q}^{\mathbf{obs}}$ as the number of time channels is increased; provided $\eta(t_m)$ are all within an acceptable range of values.

• *Case 3*: Errors corresponding to a single time channel impact $\mathbf{q}^{\mathbf{obs}}$ much more than any other time channel; i.e. $\sigma_i(t_k)/\eta(t_k) \gg \sigma_i(t_m)/\eta(t_m)$ for some k and all other m, and:

$$\widetilde{\sigma}_i \approx \frac{\sigma_i(t_k)}{M\eta(t_k)} \tag{5.21}$$

In this case, the standard deviation associated with vector $\mathbf{q}^{\mathbf{obs}}$ is strongly dependent on errors associated with a specific time channel. In practice, I would suggest not using data at this time channel.

We can measure a model's ability to fit a set of field observations by examining the misfit of vector $\mathbf{q}$; resulting in a less over-determined problem. For this, I define the collapsed data misfit:

$$\phi_c = \left\|\mathbf{W_c}\left(\mathbf{Am} - \mathbf{q}^{\mathbf{obs}}\right)\right\|_2^2 \tag{5.22}$$

Similarly to the data misfit, matrix $\mathbf{W_c}$ weights the residual between $\mathbf{Am}$ and $\mathbf{q^{obs}}$. Given that all data errors are uncorrelated and normally distributed:

$$\mathbf{W_c} = \begin{bmatrix} 1/\widetilde{\sigma}_1 & 0 & \dots & 0 \\ 0 & 1/\widetilde{\sigma}_2 & & \vdots \\ \vdots & & \ddots & 0 \\ 0 & \dots & 0 & 1/\widetilde{\sigma}_N \end{bmatrix} \tag{5.23}$$

where $\widetilde{\sigma}_i$ represents an estimate of the time-weighted standard deviation, or uncertainty, for location i. According to Eq. (5.18), $\widetilde{\sigma}_i$ may be computed using the estimates of the data standard deviations $\sigma_i(t_m)$. Similarly to the data misfit in Eq. (5.4), the collapsed data misfit also follows a chi-squared distribution with an expected value of N; where N is now the number of observation locations. It should be noted that if data are only collected at a single time channel, $\eta(t)$ may be factored out, and ϕ_c becomes equivalent to the data misfit ϕ_d.

5.2.3 Designing a Model Objective Function for the VRM Inversion

It is important to design a model objective function which stabilizes the inversion and recovers geologically reasonable models. A robust and effective model objective function for magnetic problems was proposed by Li and Oldenburg (1996):

$$\phi_m = \alpha_s \int_V w_s(r) \left| m(r) - m^{ref} \right|^2 dV + \sum_{i=x,y,z} \alpha_i \int_V w_i(r) \left| \frac{\partial m(r)}{\partial x_i} \right|^2 dV \tag{5.24}$$

where α_s, α_x, α_y and α_z are adjustable parameters which balance contributing terms in the model objective function. Deviations between a given model $m(r)$ and some reference model m^{ref} are measured in the first integral. The latter three integrals contain spatial gradients of the model along Cartesian directions $\hat{x}$, $\hat{y}$ and $\hat{z}$. Weighting functions $w_s(r)$, $w_x(r)$, $w_y(r)$ and $w_z(r)$ are used to reflect additional characteristics I hope to retain in the recovered model.

For certain problems, especially when dealing with potential fields, sensitivity weighting is used to compensate for natural decays in the kernel function. This weighting may be applied directly to the sensitivity matrix (Li and Oldenburg, 1996, 2000), or as part of the regularization (Fournier, 2015). When applied to the regularization, weighting functions in Eq. (5.24) are expressed as:

$$\begin{aligned} w_s(r) &= \widetilde{w}_s(r) w_r(r) \\ w_i(r) &= \widetilde{w}_i(r) w_r(r) \quad \text{for } i = x,y,z \end{aligned} \tag{5.25}$$

where $w_r(r)$ is the sensitivity weighting function, and $\widetilde{w}_s(r)$, $\widetilde{w}_x(r)$, $\widetilde{w}_y(r)$ and $\widetilde{w}_z(r)$ represent customizable weights based on a-priori information. When discretized onto a mesh, the model objective function takes the following form:

$$\phi_m = \alpha_\mathbf{s} \left\| \widetilde{\mathbf{W}}_\mathbf{s} \mathbf{W_r} (\mathbf{m} - \mathbf{m^{ref}}) \right\|_\mathbf{2}^\mathbf{2} + \sum_{\mathbf{i=x,y,z}} \alpha_\mathbf{i} \left\| \widetilde{\mathbf{W}}_\mathbf{i} \mathbf{W_r}\, \mathbf{G_i}\, \mathbf{m} \right\|_\mathbf{2}^\mathbf{2} \tag{5.26}$$

where $\mathbf{W_r}$ represents the application of cell-based sensitivity weighting at either the cell centers or cell faces. $\widetilde{\mathbf{W}}_\mathbf{s}$, $\widetilde{\mathbf{W}}_\mathbf{x}$, $\widetilde{\mathbf{W}}_\mathbf{y}$ and $\widetilde{\mathbf{W}}_\mathbf{z}$ are diagonal matricies containing customizable cell-based weights. $\mathbf{G_x}$, $\mathbf{G_y}$ and $\mathbf{G_z}$ are used to represent sparse discretized gradient operators.

A general approach for obtaining cell-based sensitivity weighting has been proposed by Li and Oldenburg (2000). Provided the problem has been discretized, the root mean squared sensitivity S_j of cell j to the entire dataset is defined by:

$$S_j = \left(\sum_{i=1}^{N} A_{ij}^2 \right)^{1/2}, \quad j = 1, ..., K \tag{5.27}$$

where A_{ij} are elements of the geometric sensitivity matrix, N is the number of data and K is the number of cells in the discretized model. I expect S_j to be small for cells which are far away from the receivers and larger for cells which are close. The largest values correspond to cells which are very near one or more receivers. Using the root mean squared sensitivity, a general form for the sensitivity weighting on each cell is given by:

$$w_j = \left(\sum_{i=1}^{N} A_{ij}^2 \right)^{\gamma/4}, \quad 0.5 \leq \gamma \leq 1.5 \tag{5.28}$$

where w_j are the diagonal elements of $\mathbf{W_r}$ and γ adjusts the strength of the sensitivity weighting. Larger values of γ correspond to stronger weightings and generally result in recovered models with deeper structures. For most problems however, γ should be close to 1.

5.2.4 Iterative Solver

Here, I propose a method for computing the model update direction and step length for the VRM inverse problem. Using the collapsed data misfit from Section 5.2.2 and the model objective function from Section 5.2.3, the regularized least-squares problem is expressed as follows:

$$\begin{aligned} \min_{\mathbf{m}} \phi(\mathbf{m}) \\ \phi(\mathbf{m}) &= \phi_c + \beta \phi_m \\ \phi_c &= \left\| \mathbf{W_c} \left(\mathbf{Am} - \mathbf{q^{obs}} \right) \right\|_2^2 \\ \phi_m &= \alpha_\mathbf{s} \left\| \widetilde{\mathbf{W}}_\mathbf{s} \mathbf{W_r} (\mathbf{m} - \mathbf{m^{ref}}) \right\|_\mathbf{2}^\mathbf{2} + \sum_{\mathbf{i}=\mathbf{x},\mathbf{y},\mathbf{z}} \alpha_\mathbf{i} \left\| \widetilde{\mathbf{W}}_\mathbf{i} \mathbf{W_r} \mathbf{G_i} \mathbf{m} \right\|_\mathbf{2}^\mathbf{2} \end{aligned} \tag{5.29}$$

Written in compact form, the model objective function may be expressed as:

$$\phi_m = \| \mathbf{W_m} (\Delta \mathbf{m}) \|_\mathbf{2}^\mathbf{2} \tag{5.30}$$

where

$$\mathbf{W_m^T W_m} = \alpha_s \mathbf{W_r^T} \widetilde{\mathbf{W}}_\mathbf{s}^\mathbf{T} \widetilde{\mathbf{W}}_\mathbf{s} \mathbf{W_r} + \sum_{i=x,y,z} \alpha_i \mathbf{G_i^T W_r^T} \widetilde{\mathbf{W}}_\mathbf{i}^\mathbf{T} \widetilde{\mathbf{W}}_\mathbf{i} \mathbf{W_r G_i} \tag{5.31}$$

and

$$\Delta \mathbf{m} = \mathbf{m} - \mathbf{m^{ref}} \tag{5.32}$$

To obtain the step directions for Newton's method, I require expressions for the gradient and Hessian of the global objective function at each iteration. From Eq. (5.29), the gradient of the global objective function is given by:

$$\nabla\phi(\mathbf{m}) = \mathbf{A}^{\mathbf{T}}\mathbf{W}_{\mathbf{c}}^{\mathbf{T}}\mathbf{W}_{\mathbf{c}}(\mathbf{Am} - \mathbf{q}^{\mathbf{obs}}) + \beta\mathbf{W}_{\mathbf{m}}^{\mathbf{T}}\mathbf{W}_{\mathbf{m}}(\Delta\mathbf{m}) \tag{5.33}$$

and the Hessian is given by:

$$\mathbf{H} = \mathbf{A}^{\mathbf{T}}\mathbf{W}_{\mathbf{c}}\mathbf{W}_{\mathbf{c}}\mathbf{A} + \beta\mathbf{W}_{\mathbf{m}}^{\mathbf{T}}\mathbf{W}_{\mathbf{m}} \tag{5.34}$$

Note that expressions for the gradient and Hessian no longer depend on the number of time channels. By suppressing superscript j in Eq. (5.9), the model perturbation $\delta\mathbf{m}$ is obtained by solving the following linear system at each iteration:

$$\left[\mathbf{A}^{\mathbf{T}}\mathbf{W}_{\mathbf{c}}\mathbf{W}_{\mathbf{c}}\mathbf{A} + \beta\mathbf{W}_{\mathbf{m}}^{\mathbf{T}}\mathbf{W}_{\mathbf{m}}\right]\delta\mathbf{m} = -\mathbf{A}^{\mathbf{T}}\mathbf{W}_{\mathbf{c}}^{\mathbf{T}}\mathbf{W}_{\mathbf{c}}(\mathbf{Am} - \mathbf{q}^{\mathbf{obs}}) - \beta\mathbf{W}_{\mathbf{m}}^{\mathbf{T}}\mathbf{W}_{\mathbf{m}}(\Delta\mathbf{m}) \tag{5.35}$$

For the VRM inverse problem, the Hessian may be considered symmetric positive-definite. Thus, Eq. (5.35) produces a unique solution at every iteration. In general, construction of the Hessian is avoided when solving for the Newton step. Because the geometric forward modeling operator is dense, temporary memory requirements needed to store the Hessian are only possible for very small problems. In addition, the computational cost of a direct solve for Eq. (5.35) requires $O(K^3)$ operations for dense matricies; where K is the number of model parameters.

In this thesis, Eq. (5.35) at each Newton step is solved iteratively using the conjugate gradient method (CG). The CG method employs a set of A-conjuate search directions to minimize the residual of a linear system $\mathbf{r} = \mathbf{b} - \mathbf{Mx}$; where $\mathbf{r}$ is the residual and $\mathbf{M}$ is symmetric positive definite. The CG algorithm is presented in Table 5.1. For a comprehensive review of the conjugate gradient method, see Shewchuk (1994). Convergence for

Initialize: $\mathbf{d}_{(\mathbf{0})} = \mathbf{r}_{(\mathbf{0})} = \mathbf{b} - \mathbf{Mx}_{(\mathbf{0})}$

while: $\|r\| > \delta$

$$\alpha_{(\mathbf{i})} = \frac{\mathbf{r}_{(\mathbf{i})}^{\mathbf{T}}\mathbf{r}_{(\mathbf{i})}}{\mathbf{d}_{(\mathbf{i})}^{\mathbf{T}}\mathbf{Md}_{(\mathbf{i})}}$$

$$\mathbf{x}_{(\mathbf{i+1})} = \mathbf{x}_{(\mathbf{i})} + \alpha_{(\mathbf{i})}\mathbf{d}_{(\mathbf{i})}$$

$$\mathbf{r}_{(\mathbf{i+1})} = \mathbf{r}_{(\mathbf{i})} - \alpha_{(\mathbf{i})}\mathbf{Md}_{(\mathbf{i})}$$

$$\beta_{(\mathbf{i+1})} = \frac{\mathbf{r}_{(\mathbf{i+1})}^{\mathbf{T}}\mathbf{r}_{(\mathbf{i+1})}}{\mathbf{r}_{(\mathbf{i})}^{\mathbf{T}}\mathbf{r}_{(\mathbf{i})}}$$

$$\mathbf{d}_{(\mathbf{i+1})} = \mathbf{r}_{(\mathbf{i+1})} + \beta_{(\mathbf{i+1})}\mathbf{d}_{(\mathbf{i})}$$

end

Table 5.1: Algorithm for the conjugate gradient method.

Initialize: $\alpha = 1$, $\hat{\mathbf{m}} = \mathbf{m}^{(\mathbf{j})}$

while: $\phi(\hat{\mathbf{m}}) \geq \phi(\mathbf{m}^{(\mathbf{j})})$
$\alpha = \alpha/2$
$\hat{\mathbf{m}} = \mathbf{m}^{(\mathbf{j})} + \alpha\delta\mathbf{m}$
end

$\mathbf{m}^{(\mathbf{j+1})} = \hat{\mathbf{m}}$

Table 5.2: Line-search algorithm for determining model update step-length

the CG method is generally faster than simpler gradient descent methods, as similar search directions are not re-used at later iterations. Provided the system is symmetric positive definite, CG will obtain a unique solution after at most K iterations. CG is rarely used to solve the linear system exactly. Instead, CG iterations are performed until a stopping criteria is reached. For the VRM inversion, the Newton step direction $\delta\mathbf{m}$ is returned when the L_2-norm of the residual is less than $\delta = 10^{-4}$. Once the Newton step direction has been returned, a step-length α is calculated using the line-search algorithm in Table 5.2. Newton updates are repeated until changes in the model becomes sufficiently small (i.e. $|\alpha\delta m| < \gamma$ where γ is small). According to Fournier (2015), a fixed value of $\gamma = 10^{-4}$ offers a good compromise between computational cost and accuracy.

For the CG algorithm, $\mathbf{M}$ represents the Hessian of the global objective function. To avoid construction of the Hessian, I factor Eq. (5.35) as follows:

$$(\mathbf{B^T B})\delta\mathbf{m} = \mathbf{B^T y} \tag{5.36}$$

such that:

$$\mathbf{B} = \begin{bmatrix} \mathbf{W_c A} \\ \sqrt{\alpha_s\beta}\,\widetilde{\mathbf{W}}_\mathbf{s}\mathbf{W_r} \\ \sqrt{\alpha_s\beta}\,\widetilde{\mathbf{W}}_\mathbf{x}\mathbf{G_x}\mathbf{W_r} \\ \sqrt{\alpha_s\beta}\,\widetilde{\mathbf{W}}_\mathbf{y}\mathbf{G_y}\mathbf{W_r} \\ \sqrt{\alpha_s\beta}\,\widetilde{\mathbf{W}}_\mathbf{z}\mathbf{G_z}\mathbf{W_r} \end{bmatrix} \quad \text{and} \quad \mathbf{y} = -\begin{bmatrix} \mathbf{W_c}\left(\mathbf{Am} - \mathbf{q^{obs}}\right) \\ \sqrt{\alpha_s\beta}\,\widetilde{\mathbf{W}}_\mathbf{s}\mathbf{W_r}(\Delta\mathbf{m}) \\ \sqrt{\alpha_s\beta}\,\widetilde{\mathbf{W}}_\mathbf{x}\mathbf{G_x}\mathbf{W_r}(\Delta\mathbf{m}) \\ \sqrt{\alpha_s\beta}\,\widetilde{\mathbf{W}}_\mathbf{y}\mathbf{G_y}\mathbf{W_r}(\Delta\mathbf{m}) \\ \sqrt{\alpha_s\beta}\,\widetilde{\mathbf{W}}_\mathbf{z}\mathbf{G_z}\mathbf{W_r}(\Delta\mathbf{m}) \end{bmatrix} \tag{5.37}$$

Therefore, matrix-vector products involving the Hessian can be replaced by matrix-vector products using $\mathbf{B}$. Had I not defined the collapsed data misfit in Section 5.2.2, $\mathbf{A}$ in Eq. (5.37) would be replaced by $\mathbf{TA}$ and $\mathbf{W_c}$ by $\mathbf{W_d}$; where $\mathbf{T}$ is the characteristic decay matrix and $\mathbf{W_d}$ contains the data uncertainties. Because $\mathbf{A}$ is dense, memory requirements to store $\mathbf{TA}$ increase proportional to the number of time channels. For a small number of time channels, this may not be problematic. However, for many time channels, the problem become prohibitively large. Methods exist for performing the necessary matrix-vector products in parts, however, I will not cover them here. Because the speed of the CG method depends on many rapid computations of matrix-vector products, utilization of the collapsed data misfit ultimately leads to a more efficient approach.

5.2.5 Preconditioner

Using the conjugate gradient method, I hope to solve a linear system of the form $\mathbf{Mx} = \mathbf{b}$ at each Newton iteration; where $\mathbf{M}$ is symmetric positive definite. For many iterative solvers, performance frequently depends on the condition number κ:

$$\kappa = \frac{\lambda_{max}}{\lambda_{min}} \tag{5.38}$$

where λ_{max} and λ_{min} are the largest and smallest eigenvalues of $\mathbf{M}$. For the conjugate gradient method, the number of steps required to obtain the analytic solution depends on the number of distinct eigenvalues. When solved to within a small tolerance value however, the speed at which an approximate solution may be obtained depends on how broadly the eigenvalues of matrix $\mathbf{M}$ are distributed (Shewchuk, 1994). When the eigenvalues form a compact distribution, and the condition number close to 1, convergence to an approximate solution occurs quickly. If the distribution of the eigenvalues is broad, efficiency of the conjugate gradient method can be improved by multiplying the system by a preconditioner $\mathbf{P}$:

$$\mathbf{PMx} = \mathbf{Pb} \tag{5.39}$$

Preconditioners are designed such that $\mathbf{PA}$ has a much smaller condition number than $\mathbf{M}$; thus guaranteeing a more compact distribution of eigenvalues. A solution to the original linear system is obtained by applying the CG method to Eq. (5.39). If $\mathbf{M}$ is invertible, the ideal preconditioner is its inverse $\mathbf{M^{-1}}$, since $\mathbf{M^{-1}M}$ produces the identity matrix. In this case however, implementation of the CG method would be redundant, as Eq. (5.39) provides a direct solution if $\mathbf{M^{-1}}$ is available.

For the VRM inversion, a simple and effective choice for $\mathbf{P}$ is given by the Jacobi preconditioner. To obtain the Jacobi preconditioner, I decompose $\mathbf{M}$ as follows:

$$\mathbf{M} = \mathbf{L} + \mathbf{D} + \mathbf{L^T} \tag{5.40}$$

where $\mathbf{D}$ is the diagonal of the Hessian in Eq. (5.36). $\mathbf{L}$ and $\mathbf{L^T}$ are lower and upper triangular matricies, respectively. The Jocobi preconditioner is given by $\mathbf{P} = \mathbf{D^{-1}}$. Because the Hessian for the VRM problem is symmetric positive definite, it follows that diagonal elements of $\mathbf{P}$ are strictly positive numbers. Since the preconditioner does not depend on the model, it must only be generated once. Also, because $\mathbf{P}$ is very sparse, products involving the preconditioner are computed very rapidly.

5.2.6 Bound Constraints

For many problems, it is common to expect elements within the true model $\mathbf{m}$ to lie within a specified range of values. Where model parameters are used to represent physical properties, the recovered model must ultimately contain values which are physically appropriate. According to the definition of the amalgamated magnetic property in Section 2.4, elements within $\mathbf{m}$ are strictly positive. By introducing bound constraints, the least-squares inverse problem becomes non-linear. This necessitated the implementation of Newton's method.

In this thesis, bound constraints are enforced using the approach found in Fournier (2015). At each Newton iteration, the step direction ($\delta\mathbf{m_1}$) is only computed for an active subset of the model parameters. The active

set represents the model parameters which did not require a projection onto the bounded set after the previous Newton update. The update direction ($\boldsymbol{\delta}\mathbf{m_2}$) for the set of inactive cells is obtained by computing their gradient descent direction (i.e. the right-hand side of Eq. 5.35), and scaling it if necessary. The model update direction $\boldsymbol{\delta}\mathbf{m}$ is the union of $\boldsymbol{\delta}\mathbf{m_1}$ and $\boldsymbol{\delta}\mathbf{m_2}$. While the model update is being performed, values outside the bounds are projected inside and set as inactive for the following Newton step. By updating the set of inactive cells in this fashion, I avoid reducing the active model space at each Newton iteration. This algorithm is shown in Table 5.3.

Initialize: $\mathbf{m} = \mathbf{m_0}$

while: $|\alpha\boldsymbol{\delta}\mathbf{m}| > tol$

Compute $\boldsymbol{\delta}\mathbf{m_1}$ (active cells)
Compute the gradient descent direction for inactive cells and set as $\boldsymbol{\delta}\mathbf{m_2}$

if: $max(|\boldsymbol{\delta}\mathbf{m_1}|) \leq max(|\boldsymbol{\delta}\mathbf{m_2}|)$

$$\boldsymbol{\delta}\mathbf{m_2} = C\left[\frac{max(|\boldsymbol{\delta}\mathbf{m_1}|)}{max(|\boldsymbol{\delta}\mathbf{m_2}|)}\right]\boldsymbol{\delta}\mathbf{m_2} \text{ where } C \sim 0.2$$

end

Get Newton step $\boldsymbol{\delta}\mathbf{m} = \boldsymbol{\delta}\mathbf{m_1} \cup \boldsymbol{\delta}\mathbf{m_2}$
Set $\alpha = 1$, $\hat{\mathbf{m}} = \mathbf{m}^{(\mathbf{j})}$

while: $\phi(\hat{\mathbf{m}}) \geq \phi(\mathbf{m})$

$\alpha = \alpha/2$
$\hat{\mathbf{m}} = \mathbf{m} + \alpha\boldsymbol{\delta}\mathbf{m}$
Obtain new inactive cells
Project onto bounding interval: $\hat{\mathbf{m}} = \mathbf{P}(\hat{\mathbf{m}})$

end

$\mathbf{m}^{(\mathbf{j+1})} = \hat{\mathbf{m}}$

end

Table 5.3: Algorithm for upper and lower bound constraints.

5.3 Synthetic Example

Here, the inversion methodology presented in Section 5.2 is used to recover the viscous magnetic properties of a lateritic topsoil. For this exercise, a synthetic model and synthetic data are used. The synthetic model consists of a magnetically viscous topsoil which extends roughly 10 m below the Earth's surface and displays significant inhomogeneity (Figure 5.1). For this example, I will neglect the Earth's inductive response by assuming the background is sufficiently resistive. Recovery of the model using several transmitter-receiver configurations are tested.

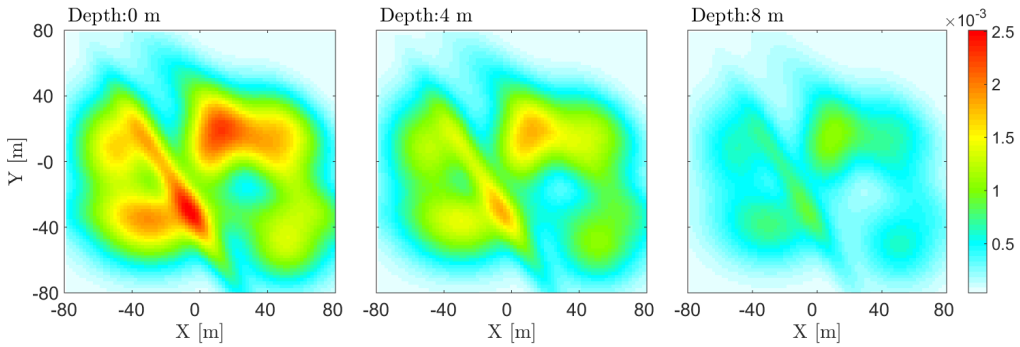

Figure 5.1: True model for the synthetic topsoil layer. This figure shows the amalgamated magnetic property at several depths.

For each transmitter-receiver configuration, the Earth's VRM response is predicted using the forward modeling scheme from Chapter 4. Synthetic data are generated by corrupting these values with Gaussian noise. The standard deviation for the noise added to each individual datum is equal to 5% of that datum's absolute value plus a small floor value. For this exercise, I will only consider the $\partial b/\partial t$ response to a unit step-off excitation. Data are predicted for 11 logarithmically spaced time-channels between 0.1 ms and 10 ms. All time channels are used in each inversion.

5.3.1 A Large Square Transmitter Loop

As a primary example, I show how data collected about a large square transmitter loop can be inverted to recover the synthetic model. Here, the transmitter loop is given a side length of 80 m and placed on the Earth's surface. The synthetic data includes all three cartesian components of the $\partial \vec{b}/\partial t$ response for a unit step-off excitation. All field observations are made 1 m above the Earth's surface using a horizontal spacing of 5 m. For this example, no observations are made within 5 m of the transmitter wire. Locations for the transmitter and the receivers are illustrated in Figure 5.2. The Earth's true response and the Gaussian noise added at $t = 1$ ms are shown in Figure 5.3.

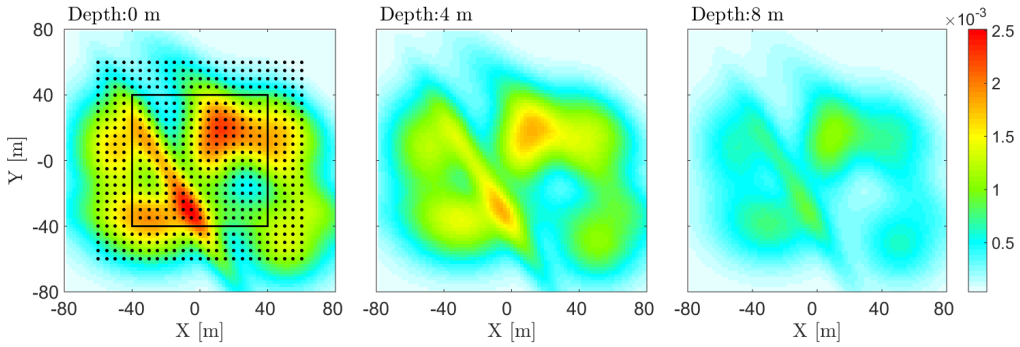

Figure 5.2: Transmitter and receiver locations for data collected about a large square transmitter loop. These locations are layed over the true model to illustrate the data coverage.

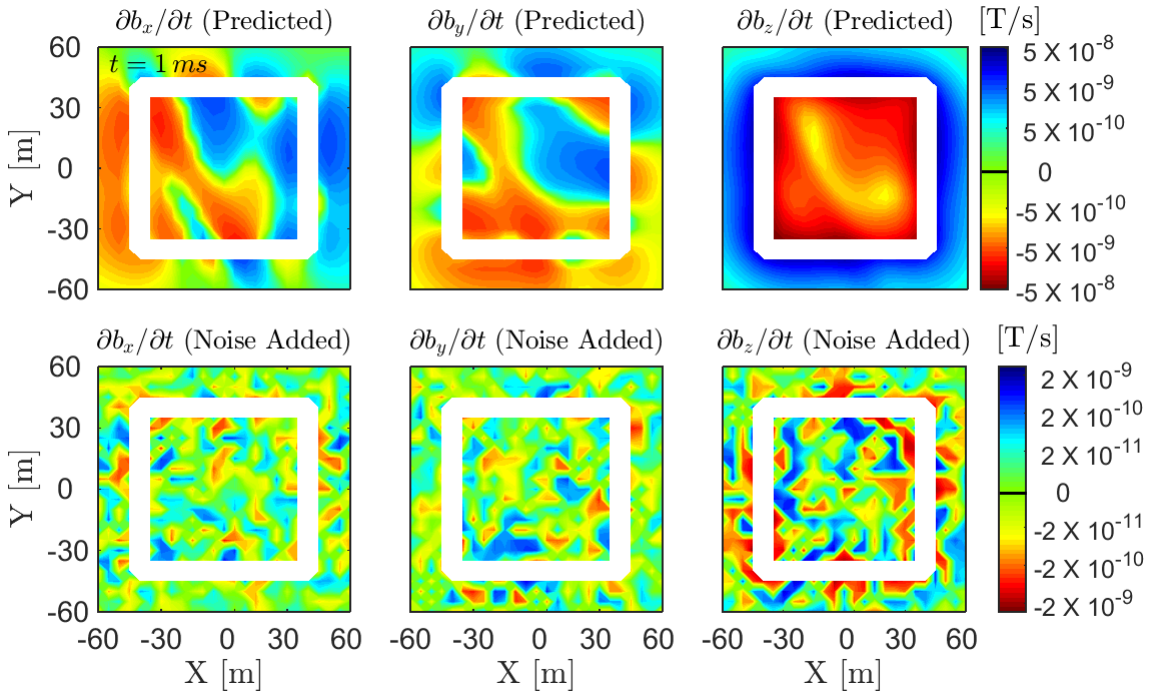

Figure 5.3: Data predicted by the VRM3D forward modeling code at $t = 1$ ms and the corresponding noise added. Data and noise are represented using a bi-log plot in order to accentuate features in the x and y components which would be difficult to see using conventional scaling. Data below a threshold value of 5×10^{-11} T/s and noise below a threshold value of 2×10^{-13} T/s are plotted as zero.

Parameters used to invert for the magnetically viscous topsoil are summarized in Table 5.5. The data uncertainties for each individual datum were obtained by taking 5% of their absolute value and adding it to a small floor value; uncertainties were estimated based on approximating the standard deviation of Gaussian noise added to generate the synthetic data. Parameters α_s, α_x, α_y and α_z were chosen such that the recovered model would be horizontally smooth. As suggested by Li and Oldenburg (2002), a sensitivity weighting parameter $\gamma = 1$ was used. The lower bound was chosen to assure the recovered model contains strictly positive values.

To recover a model for the topsoil, data were collapsed according to Eq. (5.16). Uncertainties for the collapsed data vector were obtained from the assigned data uncertainties using Eq. (5.18). The collapsed data vector and its associated uncertainties were used solve the regularized least-squares (RLSQ) problem according to Eq. (5.29). A cooling schedule was used to determine an appropriate trade-off parameter β; which balances the relative contributions of the regularization and the collapsed data misfit ϕ_c. For this approach, the RLSQ problem is solved initially using a large β value. β is then reduced and the RLSQ problem is solved again. This process is repeated until the collapsed data misfit is equal to the number of receivers; indicating a model which explains the data but does not overfit the observations. Convergence towards a final model as a function of the trade-off parameter β is shown in Figure 5.4. Experimental results indicate that models can be recovered which over-fit the data. As a result, the Tikhonov curve in Figure 5.4 does not show convergence towards the target misfit. The recovered model at several depths is shown in Figure 5.5. In general, the recovered model and the true model

Domain Size	160 m × 160 m × 50 m
Cell Width	2 m × 2 m × 2 m
Total # Cells	160,000
Total # Receivers	1,683
Data Uncertainties	5 % + 10^{-12} T/s
α_s, α_x, α_y, α_z	0.0001, 4, 4, 0.4
$\widetilde{w}_s$, $\widetilde{w}_x$, $\widetilde{w}_y$, $\widetilde{w}_z$	1, 1, 1, 1
Sensitivity Weighting	$\gamma = 1$
m_{lower}, m_{upper}	10^{-7}, $^*None$

Table 5.4: Parameters for the VRM inversion (Large Loop).

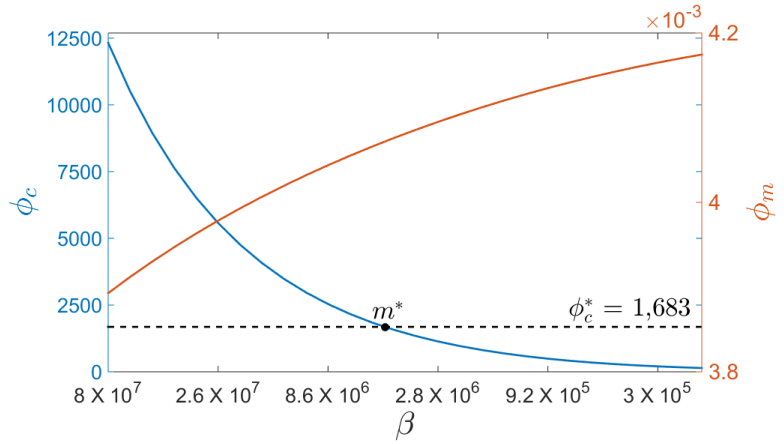

Figure 5.4: The collapsed data misfit ϕ_c and the model objective function ϕ_m as a function of the trade-off parameter β. The recovered model m^* is chosen when the collapsed data misfit reaches the expected value ϕ_c. The target value represents a model which explains the data but does not fit the noise. As β is reduced and models fit the data increasingly well, less structure is imposed on the model and ϕ_m increases.

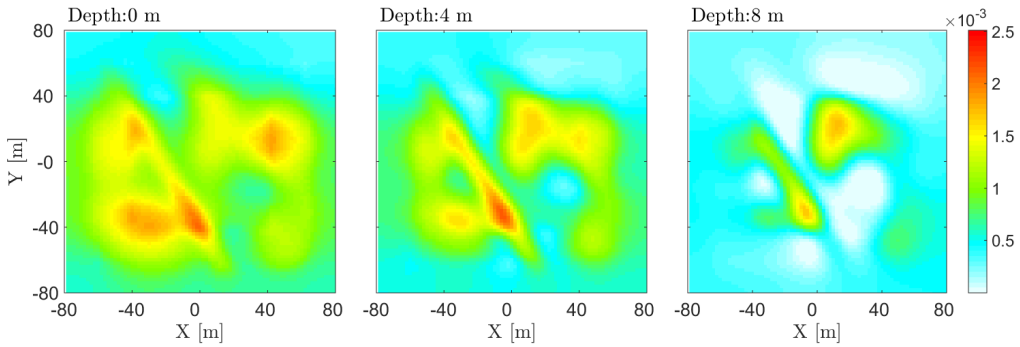

Figure 5.5: Recovered model for the topsoil layer. This figure shows the amalgamated magnetic property at several depths.

are very similar. However, the inversion does place a slight excess of magnetically viscous materials at depth. Furthermore, a significant portion of magnetically viscous material is under-represented near (X = 20 m, Y = 20 m).

The data misfit defined in Section 5.2.1 can be used to measure a model's ability to reproduce the observed data. The data misfit should not be confused with the collapsed data misfit ϕ_c which is used to solve the RLSQ problem. The data misfit was calculated according to the following expression:

$$\phi_i = \frac{d_i^{pre} - d_i^{obs}}{\varepsilon_i} \tag{5.41}$$

where ϕ_i represents the misfit for a specific datum, d_i^{pre} are data predicted using the recovered model, d_i^{obs} are observed data, and ε_i are the corresponding data uncertainties. The observed data, predicted data and data misfit at $t = 1$ ms are represented using a bi-log in Figure 5.6. Results indicate the recovered model is capable of reproducing the observed data fairly well at all times. In addition, the inversion generally avoids over-fitting the data at certain locations at the expense of others.

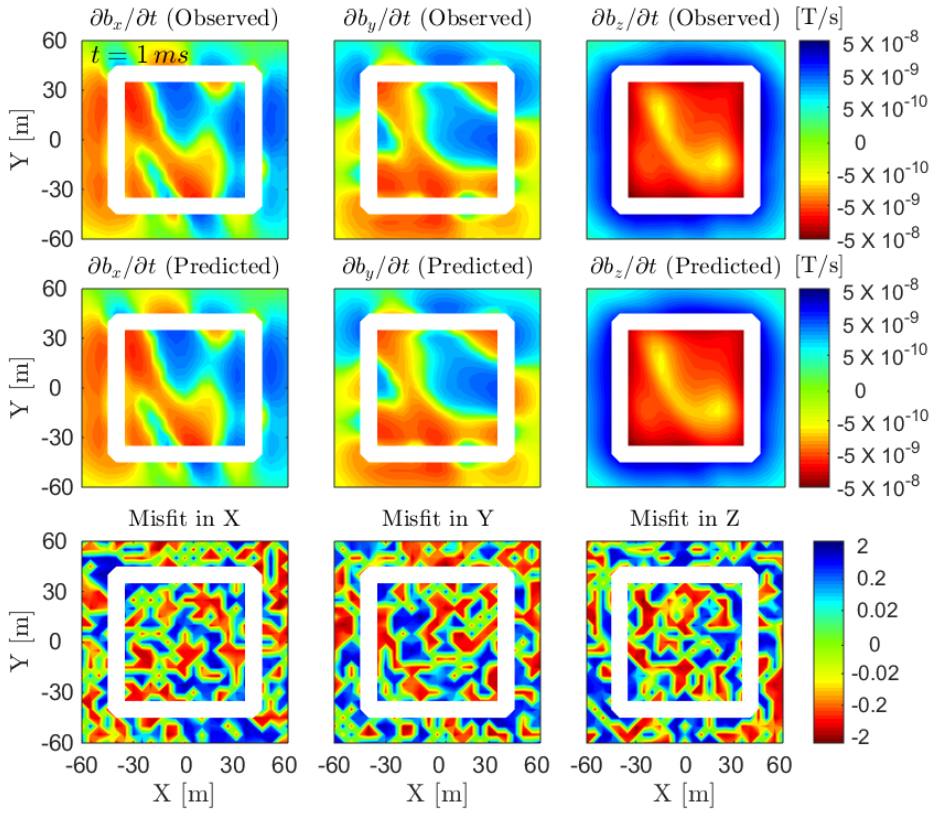

Figure 5.6: Observed data, predicted data, and data misfit a $t = 1$ ms. The data and misfit are represented using a bi-log plot in order to accentuate features in the x and y components which would be difficult to see using conventional scaling. Data below a threshold value of 5×10^{-11} T/s and data misfits below a threshold value of 0.002 are plotted as zero.

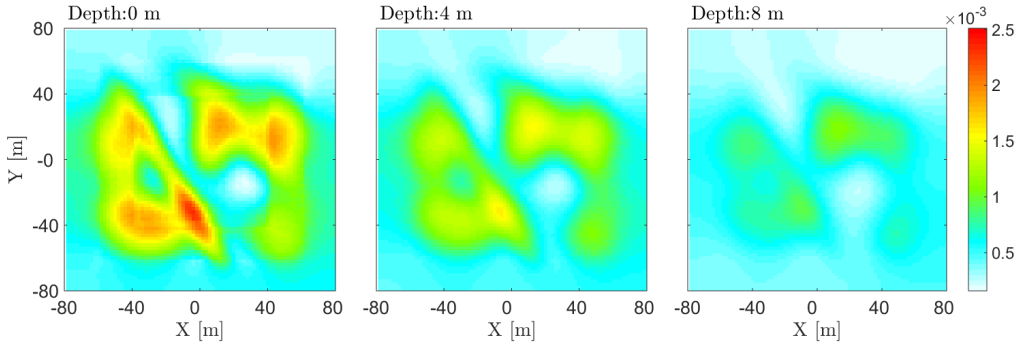

Figure 5.7: Model recovered using weighting parameters $\alpha_s = 0.0001$, $\alpha_x = \alpha_y = 4$ and $\alpha_z = 0.4$. No sensitivity weighting was used in this inversion ($\gamma = 0$). Recovered model shows artifacts on the topmost layer associated with the location of the transmitter.

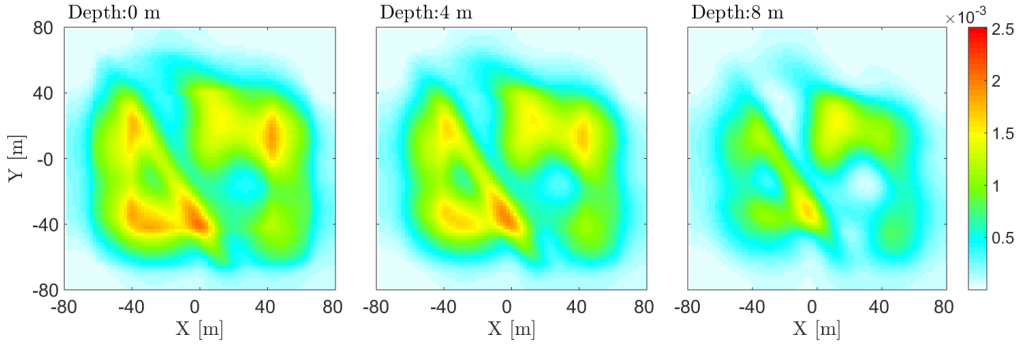

Figure 5.8: Model recovered using weighting parameters $\alpha_s = 0.0001$ and $\alpha_x = \alpha_y = \alpha_z = 4$, and a sensitivity weighting of $\gamma = 1$. Recovered model shows a significant placement of magnetically viscous materials along the path of the transmitter.

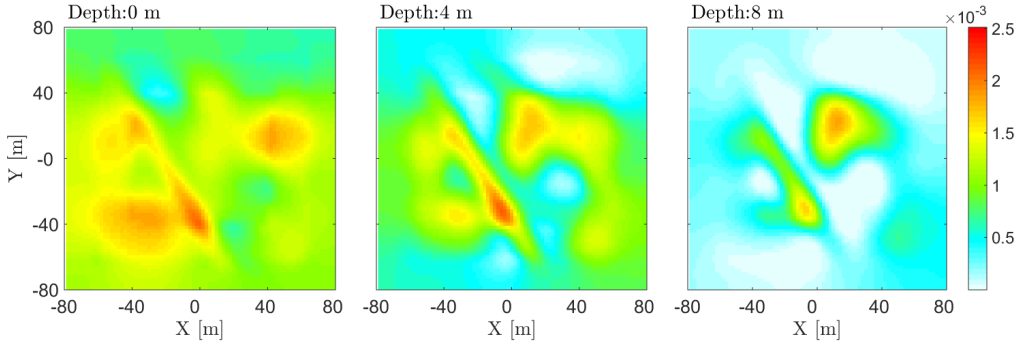

Figure 5.9: Model recovered using weighting parameters $\alpha_s = 0.0001$, $\alpha_x = \alpha_y = 4$ and $\alpha_z = 0.004$, and a sensitivity weighting of $\gamma = 1$. Recovered model shows significant smoothing in the x and y direction.

The choice in inversion parameters is important when attempting to recover reasonable geological models. By manipulating these parameters, characteristics of the recovered model can be altered. However, recovery of the most prevalent geological structures should be relatively robust to changes in the inversion parameters. To test this, parameters summarized in Table 5.5 were altered and subsequent inversions were run. To exemplify the importance of the sensitivity weighting, an inversion was run with $\gamma = 0$. The recovered model is shown in Figure 5.7. Unlike the previously recovered model, the majority of magnetically viscous material is placed near the surface; which is to be expected as the data are more sensitive to these cells. In addition, the recovered model shows distinct artifacts on the topmost layer of cells which correspond to the location of the transmitter. Many of the characteristics of the recovered model are dictated by relative weighting parameters α_s, α_x, α_y and α_z. In Figure 5.9, I show a recovered model where penalties on the gradient are the same ($\alpha_s = 0.0001$ and $\alpha_x = \alpha_y = \alpha_z = 4$). Using these parameters, I noticed that features in the recovered model are much more compact in x and y. Despite showing no obvious artifacts, the recovered model placed magnetically viscous materials along the transmitter wire's path. A recovered model with significant gradient penalties in x and y ($\alpha_s = 0.0001$, $\alpha_x = \alpha_y = 4$ and $\alpha_z = 0.004$) is shown in Figure 5.9. Here, the inversion has smoothed horizontally over regions of high and low magnetic viscosity. As a result it places a significant portion of magnetically viscous material at depth. Despite showing some minor variations, all of the models recovered in this section contain the topsoil's most prevalent geological structures; indicating the inversion is robust.

5.3.2 A Large Square Transmitter Loop (Random Locations)

Here, I alter the previous example. Instead of using a uniform receiver spacing, the observation locations are now random (Figure 5.10); with receiver heights varying between 0.5 m and 1.5 m. I show the results of an inversion which uses all three cartesian components of the $\partial b/\partial t$ response. Then, to assess whether three component data are always needed, an inversion is performed using only the vertical component. Parameters used in the inversion are summarized in Table 5.5. For the vertical component, the target misfit is reduced by a factor of 3 to account for the reduction in the number of receivers.

The recovered model at several depths using three-component data is shown in Figure 5.11. The recovered model and the true model show excellent agreement. By avoiding gaps in the data near the transmitter loop, I have recovered a better model. This is evident when examining the region near (X = 20 m, Y = 20 m). Furthermore, the decrease in magnetically viscous materials with respect to depth is much more accurate. The recovered model at several depths using only the vertical response is shown in Figure 5.12. The recovered model and the true model show good agreement, however, it is evident that a better model may be recovered using three-component data.

5.3.3 4 Large Transmitter Loops

In sections 5.3.1 and 5.3.2, data collected about a single transmitter loop were inverted. Here, data are inverted for a four transmitter array. If successful, this approach may be used to invert data collected as part of an UltraTEM survey. The transmitter and receiver locations for this survey are shown in Figure 5.13. Like in Section 5.3.2, observation locations are random; with observation heights being between 0.5 m and 1.5 m above the Earth's surface. The average horizontal spacing between observations is approximately 4 m. Parameters used in the inversion are summarized in Table 5.5.

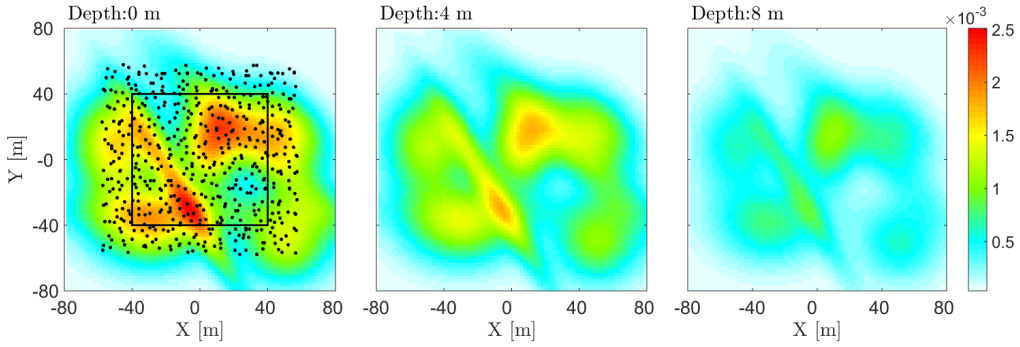

Figure 5.10: Transmitter and receiver locations for data collected about a large square transmitter loop. These locations are layed over the true model to demonstrate the data coverage.

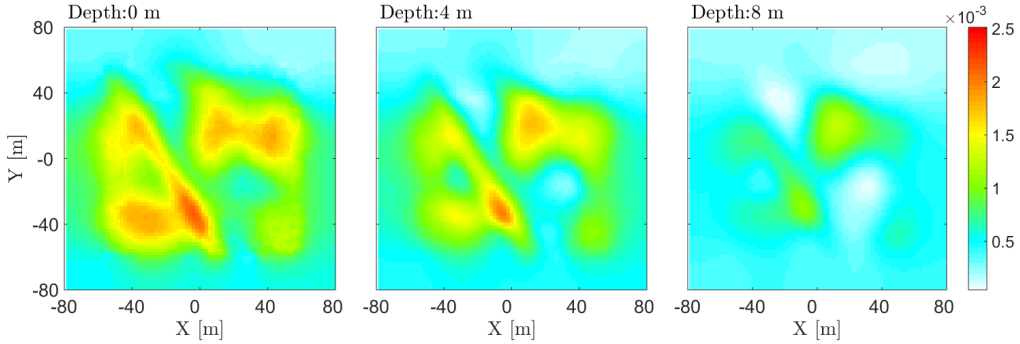

Figure 5.11: Recovered model using three-component data with $\alpha_s = 0.0001$, $\alpha_x = \alpha_y = 4$, $\alpha_z = 0.4$ and $\gamma = 1$. Recovered model and true model show excellent agreement.

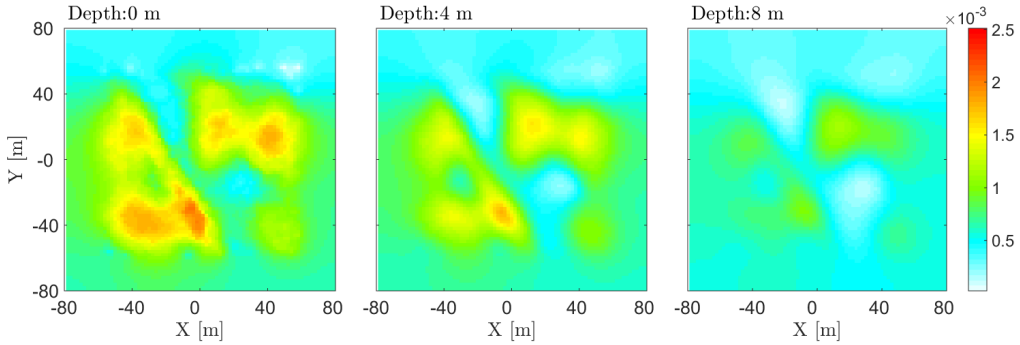

Figure 5.12: Recovered model using the Earth's vertical response with $\alpha_s = 0.0001$, $\alpha_x = \alpha_y = 4$, $\alpha_z = 0.4$ and $\gamma = 1$. Recovered model and true model show good agreement.

The recovered model at several depths using three-component data is shown in Figure 5.14. The recovered model and the true model show excellent agreement. The inversion does place a significant portion of magnetically viscous materials near the outside edges of the domain. However, this likely result from the choice in penalty parameters on the gradient.

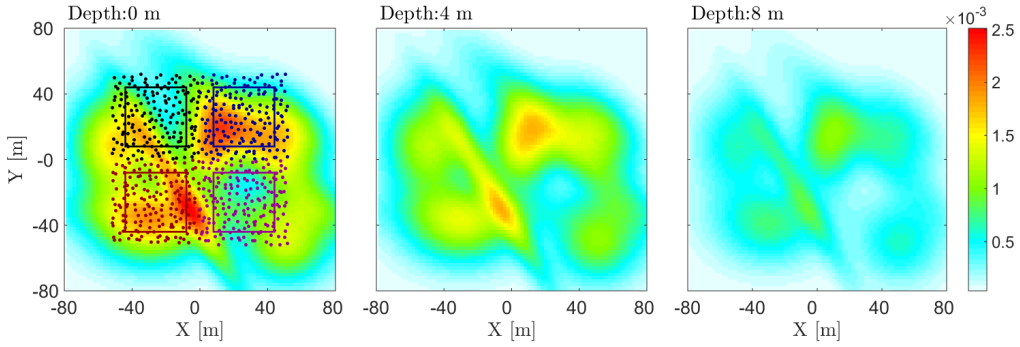

Figure 5.13: Transmitter and receiver locations for data collected about 4 large square transmitter loops. The receivers corresponding to each transmitter are distinguished by colour. Observation locations are layed over the true model to demonstrate the data coverage.

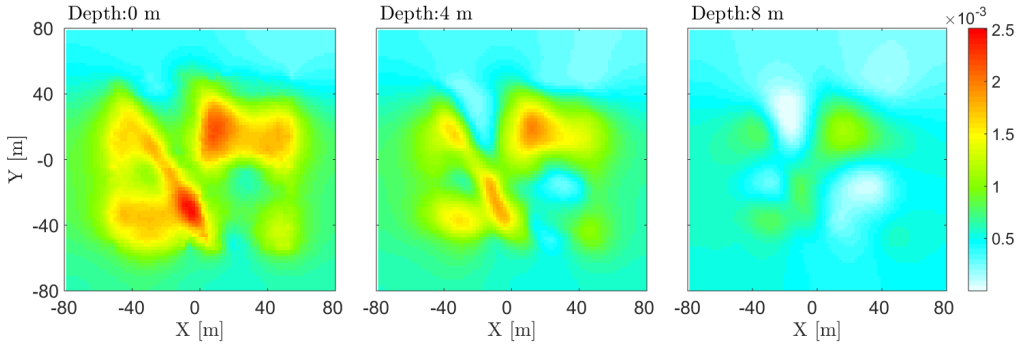

Figure 5.14: Recovered model using inversion parameters $\alpha_s = 0.0001$, $\alpha_x = \alpha_y = 4$, $\alpha_z = 0.4$ and $\gamma = 1$. Recovered model and true model show excellent agreement.

5.3.4 A Mobile Transmitter-Receiver Pair

Here, I invert data collected by a mobile transmitter-receiver pair. For this exercise, the transmitter-receiver pair was given a horizontal co-planar geometry. For all measurements, the transmitter and receiver were oriented East-West, separated by 2 m, and held 1 m above the Earth's surface; with the transmitter being located on the West. The transmitter loop was square and had a side length of 0.40 m. Data were collected using a horizontal spacing of 4 m. The location of the receiver at the time each measurement was made is shown in Figure 5.15.

Parameters used in the inversion are shown in Table 5.13. Here, weighting for the smallness component of the model objective function was increased ($\alpha_s = 0.01$, $\alpha_x = \alpha_y = 4$ and $\alpha_z = 0.4$). The inversion was also constrained using a small reference model. The reference model consisted of a half-space with physical property value 10^{-6}. Because the predicted data values were smaller for this survey configuration, a smaller floor value was used in the standard deviation when adding Gaussian noise. Therefore, it follows that a smaller floor value is to be used for the inversion. First, an inversion was run using conventional sensitivity weighting $\gamma = 1$. The results of this inversion are shown in Figure 5.16. The inversion does a very good job of locating the horizontal distribution of magnetically viscous materials. However, the inversion places a significant abundance of magnetically viscous

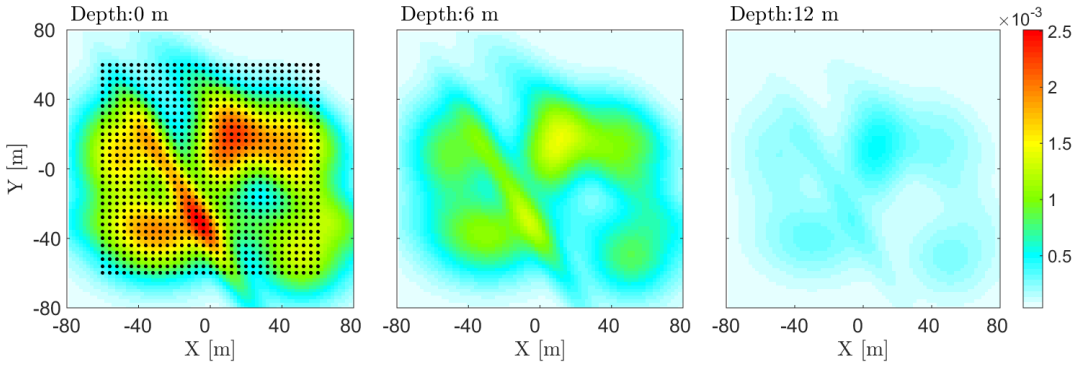

Figure 5.15: Receiver location for each measurement using the mobile transmitter-receiver configuration. Locations are layed over the true model to demonstrate the data coverage.

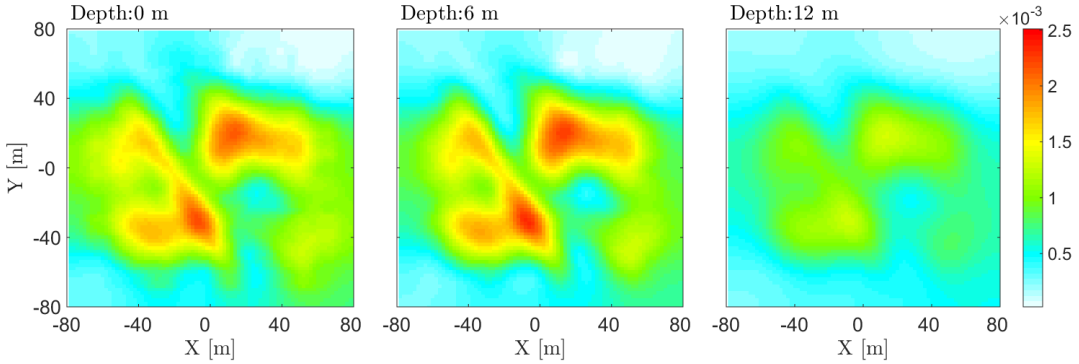

Figure 5.16: Recovered model using inversion parameters $\alpha_s = 0.01$, $\alpha_x = \alpha_y = 4$, $\alpha_z = 0.4$ and $\gamma = 1$. A reference model consisting of a half-space with physical property value $m_{ref} = 10^{-6}$ was used to constrain the inversion.

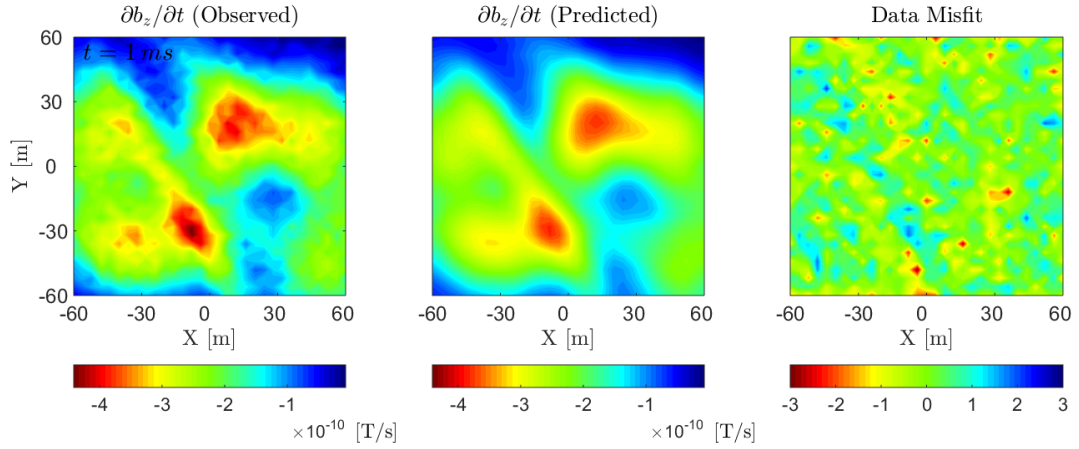

Figure 5.17: Observed data, predicted data and the data misfit at t = 1 ms. Predicted data matches the observed anomaly fairly well; as indicated by the data misfit.

materials at depth. The inversion was run with a lower sensitivity weighting ($\gamma = 0.5$) and showed similar results. This may indicate the need to have 3-component data when using a mobile source. Using Eq. (5.41), the corresponding data misfit was calculated for the recovered model. Observed data, predicted data and the data misfit at t = 1 ms are shown in Figure 5.17. Ultimately, the recovered model is able to accurately reproduce the observed anomaly. The data misfit indicates that I do not over-fit data in certain regions at the expense of others. However, sporadic locations did show elevated data misfits ($|\phi_d| > 1$).

Domain Size	160 m $\times$ 160 m $\times$ 50 m
Cell Width	2 m $\times$ 2 m $\times$ 2 m
Total # Cells	160,000
Total # Receivers	961
Data Uncertainties	5 % + 10^{-14} T/s
α_s, α_x, α_y, α_z	0.01, 4, 4, 0.4
$\widetilde{w}_s$, $\widetilde{w}_x$, $\widetilde{w}_y$, $\widetilde{w}_z$	1, 1, 1, 1
Sensitivity Weighting	$\gamma = 1$
m_{lower}, m_{upper}	10^{-7}, $^*None$
m_{ref}	10^{-6}

Table 5.5: Parameters for the VRM inversion (Mobile Transmitter-Receiver Pair).

5.4 A Workflow for Removing the VRM Response

When the TEM response from a geophysical target is contaminated by a VRM response, conventional analysis and inversion algorithms may become ineffective. However, this problem can be resolved if adequate methods are developed for removing the VRM signal and isolating the target's response. Here, I propose a general workflow for identifying and removing the VRM response from a set of TEM data. The application of the workflow to an applied problem is not carried out in this thesis. However, it remains an important area of future research. A diagram illustrating the proposed workflow is shown in Figure 5.18. Each step is summarized below:

1. Determine the Characteristic Decay Function $\eta(t)$: As a first step, the characteristic decay function for the transmitter waveform is determined according Section 4.2.2. For a step-off or square-pulse excitation, analytic expressions for the characteristic decay function are available. For an arbitrary excitation however, the transmitter waveform must be approximated by a set of square-pulses. The characteristic decay function is used as a data analysis tool in the following step and is required for the VRM inversion.

2. Identifying the Characteristic Decay in the Observed TEM Data: Using the characteristic decay function, TEM data showing comparable decays are identified. This is done in order to isolate the set of TEM data which can be attributed exclusively to the VRM response; implying these data can be reproduced using an amalgamated magnetic property model.

3. Invert the Isolated VRM Response: For this step, data attributed exclusively to the VRM response are inverted using the methodology presented in Section 5.2. In doing so, I recover an amalgamated magnetic property model which is used in the following step.

4. Predict the VRM Response at Contaminated Times/Locations: Using the recovered amalgamated magnetic property model and the characteristic decay function, the VRM response is predicted at other times and locations within the survey region. This includes times and locations where the observed TEM data are contaminated by the VRM response.

5. Subtract the Predicted VRM Response from the Observed TEM Data: The contaminating VRM signal is removed by subtracting the predicted VRM response from the set of TEM data. If successful, we are left with an electromagnetic response which can be more effectively used to obtain information about a buried target.

6. Analyze and/or Invert the Remaining TEM Signal: This step is a placeholder for the host of data analysi and inversion methods which can now be applied to the set decontaminated TEM data.

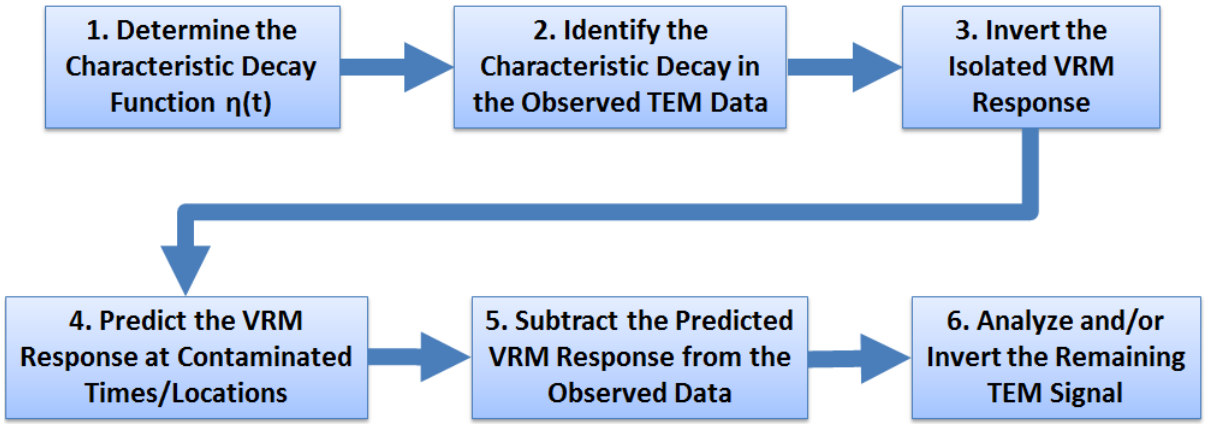

Figure 5.18: Proposed workflow for identifying and removing the contaminating VRM signal from a set of TEM data.

5.5 Summary

In this chapter, I presented an inversion methodology for recovering the distribution of magnetically viscous materials within a topsoil. By assuming the inductive and VRM responses are separable, data predicted using the recovered model can be used to remove the VRM response from contaminated TEM data. Results show that the sensitivity weighting proposed by Li and Oldenburg (2000) is capable of counteracting natural decays in the kernel function. In general, the inversion is robust to reasonable changes in the relative weighting parameters α_s, α_x, α_y and α_z; as it easily recovers the most prominent geological features. In order to recover models which do not place magnetically viscous materials along the transmitter wire, it is important to have sufficient data coverage in proximity of the transmitter. Although 3-component data are preferred, reasonable geological models can be

recovered using a single cartesian component of the Earth's VRM response. Ultimately, the inversion methodology was shown to recover appropriate geological models for a variety of transmitter-receiver configurations. These models were able to reproduce the observed data accurately and characterize the distribution of magnetically viscous materials within the topsoil. To conclude this chapter, I presented a workflow for using geophysical inversion to remove the contaminating VRM response from a set of TEM data. The application of the workflow to a particular problem will not be presented in this thesis and will instead act as a gateway to future research.

Chapter 6

Conclusion

Despite many advances since the 1980s, aspects of the viscous remanent magnetization (VRM) response and its impact on TEM sensors have remained elusive. In this thesis, I developed forward modeling and inversion methods for better characterizing VRM responses in the time-domain. I began in Chapter 2 by parameterizing the off-time VRM response in terms of an amalgamated magnetic parameter. I showed how the amalgamated magnetic parameter could be obtained easily using dual-frequency susceptibility measurements. To fill gaps left by previous analytical studies, a set of empirical expressions were derived in order to directly relate vertical and horizontal components of the VRM response to the survey geometry (Chapter 3). In Chapter 4, a linear 3D forward modeling operator was developed for predicting the off-time VRM response caused by an arbitrary excitation. This was accomplished by discretizing the Earth into a set of voxel cells and implementing the parameterization of the off-time viscous remanent magnetization. Finally in Chapter 5, I developed an inversion approach for recovering the distribution of magnetically viscous materials from a set of TEM observations. The chapter was concluded by presenting a workflow for removing the VRM response from a set of TEM data.

The amalgamated magnetic property defined in Chapter 2 is not a purely abstract quantity, as it can be measured for a given sample. Using a database of dual-frequency measurements on lateritic soil samples, I was able to obtain upper and lower physical bounds for the amalgamated magnetic property. Thus, I was able to define upper and lower bounds for the strength of the viscous remanent magnetization lateritic soils exhibit. The ability to define a soil's viscous remanent magnetization using simple laboratory measurements ultimately benefits the inversion process. By measuring the amalgamated magnetic property for samples within a particular region, we can constrain the VRM inversion via bound constraints and/or a reference model. This aids in the recovery of models which are physically plausible, geologically accurate and fit the data more easily.

For a half-space model, I was successful in deriving analytic expressions which directly relate the VRM response to the survey geometry (Chapter 3), most notably, the radius of a circular transmitter loop. Unlike the final analytic results derived by others, expressions derived in this thesis do not require the numerical integration of one or more elementary integrals. In addition, I consider both the vertical and horizontal components of the VRM response and its time-derivative, whereas others generally do not. With continual development of tri-axial sensors, a better understanding of the horizontal response is increasingly important. By considering the inductive

and VRM responses as being separable, I was able to determine the cross-over time at which the observed TEM response within a transmitter loop became dominated by the VRM signal. As a result, expressions derived in this chapter can be used to choose the optimal loop size for a particular survey and determine the range of time channels which are most impacted by the VRM response.

The 3D forward model constructed in Chapter 4 allows for rapid computation of the VRM response for an arbitrary number of time channels. This was made possible by the parameterization of the off-time viscous remanent magnetization within each cell. Using a sensitivity refinement algorithm, we are now able to accurately predict the VRM response near the transmitter without increasing the size of the forward modeling operator. By constructing a 3D forward model, we are no longer limited to understanding the VRM response through layered Earth models. Additionally, we have another tool for investigating the relationship between the survey geometry and VRM response for an inductive source.

In Chapter 5, I demonstrated how geophysical inversion could be used to recover the distribution of magnetic viscous materials from a set of TEM data. By using the amalgamated magnetic property to define the magnetic viscosity within each cell, I was able to invert for a single model parameter for each cell. I was able to show that the uncertainties corresponding to the collapsed data could be reduced by making observations at more time channels. Examples were used to show that the inversion was robust and could be applied for a multitude of survey geometries. Using recovered models, we can now start to answer questions regarding the depth and horizontal distribution of magnetically viscous soils within a region. More importantly, these models can be used to predict VRM responses at other times and locations within the survey region. Assuming the inductive and VRM responses are separable, the predicted data from recovered models can be used to remove the VRM signal from a set of field observations. The workflow for this process was presented at the end of Chapter 5.

Ultimately, the results presented in this thesis were able to address nearly all of the problems described in the introduction. Using newly obtained forward modeling and inversion algorithms, we can answer more complex questions about the impact of magnetically viscous soils on TEM instruments, consider the VRM responses exhibited by 3D distributions of magnetically viscous materials, and have an approach for removing the contaminating VRM signal from a set of TEM data.

6.1 Future Research

Despite providing a significant advancement in our understanding of the VRM response, there are several details in the thesis work which may require additional attention. Here, I discuss these details in the context of future research projects.

I ended Chapter 5 by proposing a workflow for removing the VRM response from a set of TEM data. In the future, I intend to validate the workflow by applying it to a set of synthetic problems. Once validated, I can begin to apply this approach to field acquired data.

The magnetic viscosity exhibited by most lateritic soils can be fit adequately by assuming a log-uniform distribution of time-relaxation constants bounded by a set of finite limits. These limits determine the range of times in which our parameterization of the soil's off-time VRM is accurate, thus determining the times when our numerical forward modeling and inversion codes are valid. For most practical cases, it can be assumed that the log-uniform distribution of time-relaxation constants is sufficiently broad; thus, I expect the parameterization of the off-time viscous remanent magnetization to be valid over a broad range of times. To verify this assumption however, upper and lower bounds should be determined for a diverse set of soil samples by fitting full-spectrum magnetic susceptibility measurements. Ultimately, this would allow us to define the typical range of time-channels in which our current forward modeling and inversion codes are valid.

In this thesis, I assumed that inductive and VRM responses were approximately separable to first order. This assumption was made according to field experiments, physical property measurements, and numerical modeling results found in the literature. Presently, the coupling between the inductive and VRM responses is poorly understood, as numerical validation of their separation is done almost entirely with half-space or layered Earth models. In the future, I may consider developing numerical modeling codes which do not rely on the separation of the inductive and VRM responses. These codes could be used to better understand the coupling between both responses and validate their separation for a more diverse set of geological scenarios.

Bibliography

Austin, J., S. Geuna, D. Clark, and D. Hillan, 2014, Remanence, self-demagnetization and their ramifications for magnetic modelling of iron oxide copper-gold deposits: An example from Candelaria, Chile: Journal of Applied Geophysics, **109**, 242–255. → pages 20

Barsukov, P., and E. Fainberg, 2001, Superparamagnetic effect over gold and nickel deposits: European Journal of Environmental and Engineering Geophysics, **72**, 61–72. → pages 2, 13, 20, 35, 36, 40, 41

Bhattacharyya, B. K., 1964, Magnetic anomalies due to prism-shaped bodies with arbitrary polarization: Geophysics, **29**, 517. → pages 43, 48, 49

Billings, S. D., L. R. Pasion, D. W. Oldenburg, and J. Foley, 2003, The influence of magnetic viscosity on electromagnetic sensors: EUDEM – SCOT2, Int. Conf. on Requirements and Technologies for the Detection,Removal and Neutralization of Landmines and UXO, Brussels. → pages vii, 2, 6, 7, 8, 15, 20, 25, 38, 41, 90

Blakely, R. J., 1996, Magnetization, *in* Potential Theory in Gravity and Magnetic Applications, 1 ed.: Cambridge University Press, 5, 82–83. → pages 29, 43

Buselli, G., 1982, The effect of near-surface superparamagnetic material on electromagnetic measurements: Geophysics, **47**, 1315–1324. → pages 2, 6, 7, 13, 20, 25, 26, 35, 36, 37, 38, 40, 41

C. P. B., 1977, Soil Taxonomy. A Basic System of Soil Classification for Making and Interpreting Soil Surveys. 1975. 754 pp., 12 coloured plates. Agriculture Handbook No. 436. Soil Conservation Service, U.S. Department of Agriculture. From Superintendent of Documents, U.S. Government Printing Office, Washington, D.C. 20402. Price $17.50.F. D. Hole 1976. Soils of Wisconsin. xvi + 223 pp., 8 pls, 151 figs, 26 tables. University of Wisconsin Press, Madison. Price $15.00. ISBN 0 299 06830 7., **114**. → pages 2

Clark, D. A., and D. W. Emerson, 1991, Notes on rock magnetization characteristics in applied geophysical studies: Exploration Geophysics, **22**, 547. → pages ix, 19

Colani, C., and M. J. Aitken, 1966, Utilization of magnetic viscosity effects in soils for archaeological prospection: Nature, **212**, 1446–1447. → pages 25

Corless, R. M., G. H. Gonnet, D. E. G. Hare, D. J. Jeffrey, and D. E. Knuth, 1996, On the Lambert-W function: Advances in Computational Mathematics, **5**, 329–359. → pages 39, 93, 94

Dabas, M., A. Jolivet, and A. Tabbagh, 1992, Magnetic-susceptibility and viscosity of soils in a weak time-varying field: Geophysical Journal International, **108**, 101–109. → pages 6, 7, 8, 9, 12, 13, 19, 20, 21, 90, 91

Dabas, M., and J. R. Skinner, 1993, Time-domain magnetization of soils (VRM), experimental relationship to quadrature susceptibility: Geophysics, **58**, 326. → pages 13

Das, Y., 2004, A preliminary investigation of the effects of soil electromagnetic properties on metal detectors: Detection and Remediation Technologies for Mines and Minelike Targets IX, 677–690. → pages 2

———, 2006, Effects of soil electromagnetic properties on metal detectors: IEEE Transactions on Geoscience and Remote Sensing, **44**, 1444–1453. → pages 2, 8, 22, 25, 38

Dearing, J. A., R. J. L. Dann, K. Hay, J. a. Lees, P. J. Loveland, B. a. Maher, and K. O'Grady, 1996, Frequency-dependent susceptibility measurements of environmental materials.: Geophysical Journal International, **124**, 228–240. → pages 6, 20

Druyts, P., Y. Das, C. Craeye, and M. Acheroy, 2009, Modeling the response of electromagnetic induction sensors to inhomogeneous magnetic soils with arbitrary relief: IEEE Transactions on Geoscience and Remote

Sensing, **47**, 2627–2638. → pages 2, 19, 26, 38
Dunlop, D. J., and Ö. Özdemir, 1997, Rock Magnetism. → pages 5, 6, 7, 89
Erdelyi, A., W. Magnus, F. Oberhettinger, and F. G. Tricomi, 1954, Tables of integral transforms: McGraw-Hill Book Company. → pages 31
Fannin, P., and S. Charles, 1995, On the influence of distribution functions on the after-effect function of ferrofluids: Journal of Physics D: Applied Physics, **239**, 1794–1799. → pages 7
Fournier, D., 2015, A cooperative magnetic inversion method with an Lp norm regularization: PhD thesis. → pages 42, 65, 68, 69
Griffiths, D. J., 2007, An Introduction to Electrodynamics, **110**. → pages 6, 23
Igel, J., H. Preetz, and S. Altfelder, 2012, Magnetic viscosity of tropical soils: Classification and prediction as an aid for landmine detection: Geophysical Journal International, **190**, 843–855. → pages 5, 6, 7, 8, 91
Igel, J., H. Preetz, K. Takahashi, and M. Loewer, 2013, Landmine and UXO detection using EMI and GPR -limitations due to the influence of the soil: First Break, **31**, 43–51. → pages 7
Khamvongsa, C., and E. Russell, 2009, LEGACIES OF WAR – Cluster Bombs in Laos: Critical Asian Studies, **41**, 281–306. → pages 1
Kozhevnikov, N. O., and E. Y. Antonov, 2008, The magnetic relaxation effect on TEM responses of a uniform earth: Russian Geology and Geophysics, **49**, 197–205. → pages 2, 22, 41
Krahenbuhl, R. A., and Y. Li, 2007, Influence of self-demagnetization effect on data interpretation in strongly magnetic environments: SEG/San Antonio 2007 Annual Meeting, 713–717. → pages 20
Lee, T., 1984, The effect of a Superparamagnetic Layer: Geophysical Prospecting, **32**, 480–496. → pages 2, 7, 35, 36, 40
Lelièvre, P. G., and D. W. Oldenburg, 2006, Magnetic forward modelling and inversion for high susceptibility: Geophysical Journal International, **166**, 76–90. → pages 20
Li, Y., and D. W. Oldenburg, 1996, 3-D inversion of magnetic data: Geophysics, **61**, 394–408. → pages 65
———, 2000, Joint inversion of surface and three-component borehole magnetic data: Geophysics, **65**, 540 – 552. → pages 65, 66, 81
Li, Y. T., and R. Wong, 2008, Integral and series representations of the Dirac delta function: Communications on Pure and Applied Analysis, **7**, 229–247. → pages 34
Mathematica, W., 2016, Online Integrator. → pages 31
Meglich, T., Y. Li, L. R. Pasion, D. W. Oldenburg, R. L. van Dam, and S. D. Billings, 2008, Characterization of Frequency-Dependent Magnetic Susceptibility in UXO Electromagnetic Geophysics: Society of Exploration Geophysicists Annual Meeting, 1248–1252. → pages 7, 8
Moskowitz, B., 1985, Magnetic viscosity, diffusion after-effect, and disaccommodation in natural and synthetic samples: Geophysical Journal International, **82**, 143–161. → pages 6, 7, 12
Mullins, C. E., and M. S. Tite, 1973, Magnetic viscosity, quadrature susceptibility, and frequency dependence of susceptibility in single-domain assemblies of magnetite and maghemite: Journal of Geophysical Research, **78**, 804–809. → pages 7, 8, 21
Nabighian, M. N., 1979, Quasi-static transient response of a conducting half-space An approximate representation: Geophysics, **44**, 1700–1705. → pages 25, 29, 38
Néel, M. L., 1949, Théorie du traînage magnétique des ferromagnétiques en grains fins avec application aux terres cuites: Annales de Geophysique, **5**, 99–136. → pages 6, 7, 12, 13, 41, 89
Newman, G. A., G. W. Hohmann, and W. L. Anderson, 1986, Transient electromagnetic response of a threedimensional body in a layered earth: Geophysics, **51**, 1608–1627. → pages 23
Olhoeft, G. R., and D. W. Strangway, 1974, Magnetic Relaxation and the Electromagnetic Response Parameter: Geophyics, **39**, 302–311. → pages 9, 19
Pasion, L., 2007, Inversion of time domain electromagnetic data for the detection of unexploded ordnance: PhD thesis. → pages 2, 3, 5, 6, 7, 8, 9, 12, 13, 19, 20, 22, 25, 26, 38, 41, 90, 92
Pasion, L. R., S. D. Billings, and D. W. Oldenburg, 2002, Evaluating the effects of magnetic soils on TEM measurements for UXO detection: Society of Exploration Geophysicists Annual Meeting, 2–5. → pages 2
Peel, M. C., B. L. Finlayson, and T. A. McMahon, 2007, Updated world map of the Koppen-Geiger climate classification: Hydrology and Earth System Sciences, **11**, 1633–1644. → pages viii, 2

Rao, D. B., and N. R. Babu, 1993, A Fortran-77 computer program for three-dimensional inversion of magnetic anomalies resulting from multiple prismatic bodies: Computers & Geosciences, **19**, 781–801. → pages 42

Ratnanather, J. T., J. H. Kim, S. Zhang, A. M. J. Davis, and S. K. Lucas, 2011, IIPBF: a MATLAB toolbox for infinite integrals of product of Bessel functions: ACM Trans. Math. Softw., 11. → pages 23, 33

Sharma, P., 1966, Rapid computation of magnetic anomalies and demagnetization effects caused by bodies of arbitrary shape: Pure and Applied Geophysics PAGEOPH, **64**, 89–109. → pages 42, 43

Shewchuk, J. R., 1994, An Introduction to the Conjugate Gradient Method Without the Agonizing Pain. → pages 67, 69

Thompson, R., and F. Oldfield, 1986, Environmental Magnetism: Allen & Unwin. → pages 6

Tikhonov, A. N., and V. Y. Arsenin, 1977, Solution of Ill-Posed Problems: Winston & Sons. → pages 60, 61, 63

van Dam, R. L., J. B. J. Harrison, J. M. H. Hendrickx, D. A. Hirschfeld, R. E. North, J. E. Simms, and Y. Li, 2005, Mineralogy of Magnetic Soils at a UXO Remediation Site in Kaho'olawe Hawaii: Symposium on the Application of Geophysics to Engineering and Environmental Problems, 666–677. → pages 19, 38

van Dam, R. L., J. M. H. Hendrickx, J. B. J. Harrison, B. Borchers, D. I. Norman, S. Ndur, C. Jasper, P. Niemeyer, R. Nartey, D. Vega, L. Calvo, and J. E. Simms, 2004, Spatial variability of magnetic soil properties: Detection and Remediation Technologies for Mines and Minelike Targets IX, 665–676. → pages 19, 38

van Dam, R. L., J. M. H. Hendrickx, J. B. J. Harrison, and R. S. Harmon, 2008, Towards a model for predicting magnetic susceptibility of bedrock regolith and soils: Detection and Sensing of Mines, Explosive Objects, and Obscured Targets XIII, 69530Z–69530Z–10. → pages ix, 7, 19, 20, 22

Varga, E., H. D. Storzer, and A. Beyer, 1996, A method for the calculation of the field of three-dimensional bodies with a homogeneous magnetization: Electrical Engineering (Archiv fur Elektrotechnik), **80**, 111–114. → pages 42, 43

Ward, S. H., and G. W. Hohmann, 1988, Electromagnetic theory for geophysical applications, *in* Electromagnetic Methods in Applied Geophysics: Theory: Society of Exploration Geophysicists, 131–311. → pages 22, 30

Worm, H., 1998, On the superparamagnetic table single domain transition for magnetite , and frequency dependence of susceptibility: Geophysical Journal International, **133**, 201–206. → pages 8, 91

Zadorozhnaya, V. Y., N. O. Kozhevnikov, and P. Nyabeze, 2012, Superparamagnetic effect, effect provided by red soil in Southern Africa: EM Induction Workshop, 1–4. → pages 2, 20, 41

Appendix A

Dependence of Magnetic Viscosity on the Volume Distribution of SP Grains

Because of thermal fluctuations, superparamagnetic (SP) grains are exposed to a spectrum of thermal activation energies. Spontaneous re-orientation of an SP grain's remanent magnetic moment, occurs when the activation energy is larger than the magnetization's barrier energy E_b. The average time between spontaneous re-orientations is given by the Néel relaxation time (Néel, 1949):

$$\tau = \tau_0 \, exp\left(\frac{E_b}{k_b T}\right) \tag{A.1}$$

where k_b is the Boltzmann constant, T is the temperature, and $\tau_0 \sim 10^{-9}$ s is the "attempt time" (Dunlop and Özdemir, 1997). For a collection of SP grains defined by E_b, τ can be used to represent the rate of magnetic relaxation in response to an applied magnetic field. Néel (1949) modeled the magnetic viscosity by considering a collection of non-interacting single-domain SP grains. If the magnetic anisotropy mechanism is identical for all the SP grains, then (Dunlop and Özdemir, 1997):

$$E_b = KV \tag{A.2}$$

where K is the constant of magnetic anisotropy for the material, and V is the volume of individual grains. Therefore, if a collection of SP grains is defined over a spectrum of energy barriers, the resulting distribution of time-relaxation constants corresponds to a distribution of SP grain volumes. The relationship between V and τ can be obtained by combining Eqs. (A.1) and (A.2):

$$V = \frac{k_b T}{K} ln(\tau/\tau_0) \tag{A.3}$$

Only a small portion of the ferrimagnetic grains within an iron-bearing soil are superparamagnetic; as illustrated in Figure A.1. However, the distribution of SP grain volumes greatly impacts the magnetic relaxation exhibited by the soil. This distribution can be defined using a density function $\rho(V)$. By definition, the density

function integrated over all values, is equal to 1. Thus:

$$\int_0^\infty \rho(V)\,dV \equiv 1 \tag{A.4}$$

Because Eq. (A.3) provides a relationship between V and τ, Eq. (A.4) can be re-expressed in terms of τ by using a change of variables:

$$\int_0^\infty \rho(\tau)\left(\frac{dV}{d\tau}\right)d\tau = \int_0^\infty f(\tau)\,d\tau = 1 \tag{A.5}$$

where $f(\tau)$ is the density function for the distribution of time relaxation constants, commonly referred to as the weighting function (Dabas et al., 1992; Billings et al., 2003; Pasion, 2007).

Consider a broad distribution of ferrimagnetic grain sizes, where SP grains have volumes between V_1 and V_2 (Figure A.2). Ferrimagnetic grains with volumes less than V_1 are still superparamagnetic, but we assume their corresponding magnetic relaxation occurs too quickly and cannot be observed. The distribution of SP grain volumes can be considered approximately uniform if: 1) the interval $[V_1, V_2]$ is sufficiently small, and 2) the

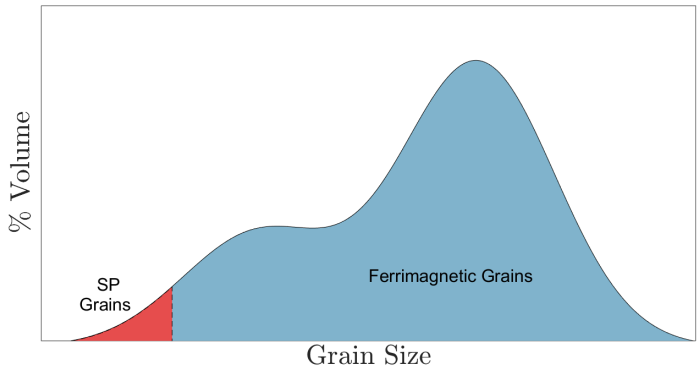

Figure A.1: Grains size distribution for ferrimagnetic grains within a theoretical sample. Blue region shows an arbitrary distribution for all ferrimagnetic grains. Red represents the portion of grains capable of exhibiting superparamagnetism.

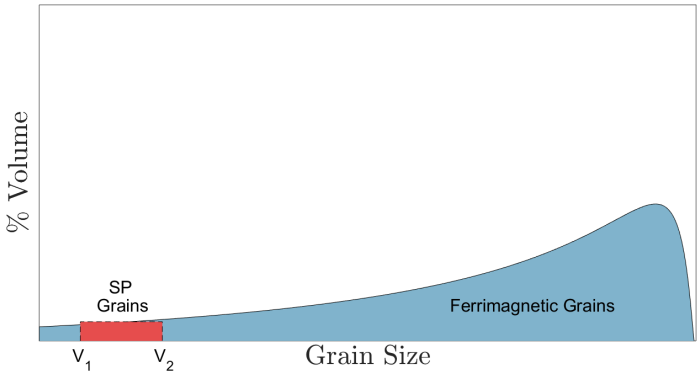

Figure A.2: Flat grain size distribution for ferrimagnetic grains. The distribution of SP grains (red) is approximately uniform between V_1 and V_2.

interval sits within the tail of a broad distribution of ferrimagnetic grain sizes (reference). The density function for a uniform distribution of SP grain size between V_1 and V_2 is given by:

$$\rho(V) = \begin{cases} \dfrac{1}{V_2 - V_1} & \text{for } V_1 \leq V \leq V_2 \\ 0 & \text{otherwise} \end{cases} \tag{A.6}$$

Substituting Eqs. (A.4) and (A.6) into expression (A.5):

$$\int_0^{\infty} f(\tau) d\tau = \int_{\tau_1}^{\tau_2} \frac{1}{\tau \, ln(\tau_2/\tau_1)} d\tau = 1 \tag{A.7}$$

According to the integrand of Eq. (A.7), the weighting function for the corresponding distribution of time-relaxation constants is:

$$f(\tau) = \begin{cases} \dfrac{1}{\tau \, ln(\tau_2/\tau_1)} & \text{for } \tau_1 \leq \tau \leq \tau_2 \\ 0 & \text{otherwise} \end{cases} \tag{A.8}$$

Therefore, a uniform distribution of volumes between V_1 and V_2, corresponds to a log-uniform distribution of time-relaxation constants between τ_1 and τ_2. This distribution can be used to model the magnetic viscosity exhibited in most iron-bearing soil samples (Dabas et al., 1992; Worm, 1998; Igel et al., 2012).

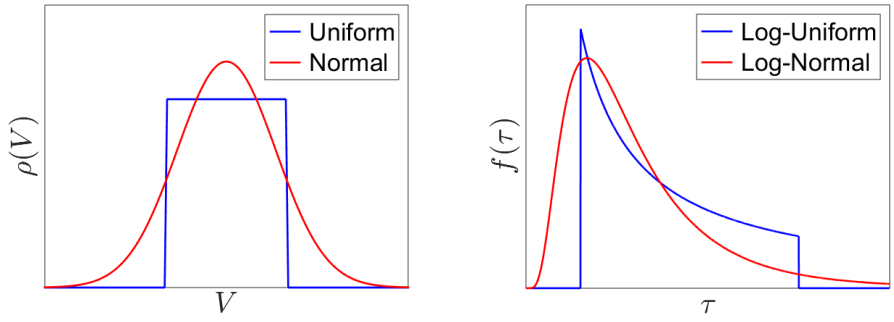

(a) **(b)**

Figure A.3: (a) Theoretical representation of a uniform and a normal distribution for SP grain volumes. (b) Theoretical representation of a log-uniform and a log-normal distribution for time-relaxation constants.

Now consider a collection of SP grains which are characterized by a normal distribution of volumes. In this case, we assume that superparamagnetism occurs primarily in ferrimagnetic grains around a certain size. This is represented by V_c, and marks the center of the volume distribution. Superparamagnetism is less frequently observed in ferrimagnetic grains whose volumes are greater than or less than V_c. The span of SP grain volumes is represented by the distribution's standard deviation α. The density function for the normal distribution is given by:

$$\rho(V) = \frac{1}{\alpha\sqrt{2\pi}} exp\left(\frac{-(V - V_c)^2}{2\alpha^2}\right) \tag{A.9}$$

Using the same method as before, the corresponding distribution of time-relaxation constants can be expressed as:

$$f(\tau) = \frac{1}{\tau\beta\sqrt{2\pi}} exp\left(\frac{-(ln\,\tau - ln\,\tau_c)^2}{2\beta^2}\right) \tag{A.10}$$

Eq. A.10 takes the form of a log-normal distribution. This distribution was proposed by Pasion (2007), to explain iron-bearing soils which could not be fit by assuming a log-uniform distribution of time-relaxation constants. The shape of the log-normal distribution is defined by parameters $ln\,\tau_c$ and β. τ_c is the Néel relaxation time corresponding to SP grains of volume V_c. β is the standard deviation $ln\,\tau$ for all SP grains. The general shape for both a uniform and a normal distribution of SP grain volumes can be seen in Figure A.3a. The corresponding log-uniform and log-normal distributions for time-relaxation constants are shown in Figure A.3b.

Appendix B

Deriving the Lower Branch of the Lambert W Function

We wish to solve expression (3.35) for $R_B = 1$ to obtain expression (3.38). This is equivalent to solving an expression of the form:

$$At^{-3/2} + lnt \approx -\gamma + ln\tau_2 \tag{B.1}$$

where:

$$A = \frac{ln(\tau_2/\tau_1)}{15Q(\rho/a)\sqrt{\pi}}\left(\frac{2+\Delta\chi}{\Delta\chi}\right)(\mu_0\sigma)^{3/2}a^3 \tag{B.2}$$

Using a change of variables, we let $u = t^{-3/2}$. With some algebra, expression (B.1) can be rewritten as:

$$-\frac{3}{2}Aue^{-\frac{3}{2}Au} \approx -\frac{3}{2}Ae^{\frac{3}{2}(\gamma - ln\tau_2)} \tag{B.3}$$

Solutions to an expression of the form $xe^x = C$ are defined as branches of the Lambert W function $W[n,C]$, where n are integer values (Corless et al., 1996). Therefore, the solutions u_n to expression (B.3) are:

$$u_n \approx -\frac{2}{3A}W\left[n, -\frac{3}{2}Ae^{\frac{3}{2}(\gamma - ln\tau_2)}\right] \tag{B.4}$$

We can use expressions (3.37) and (B.2) to show $A = \frac{2}{3}t_\beta^{3/2}$. By replacing $u_n = t_n^{-3/2}$:

$$\begin{aligned} t_n^{-3/2} &\approx -t_\beta^{-3/2}W\left[n, -t_\beta^{3/2}e^{\frac{3}{2}(\gamma - ln\tau_2)}\right] \\ \implies t_n &\approx t_\beta\left(-W\left[n, -\left(\frac{t_\beta}{\tau_2}e^{\gamma}\right)^{3/2}\right]\right)^{-2/3} \end{aligned} \tag{B.5}$$

Real-valued solutions $W[n,x]$ only exist for $n=-1,0$ (Corless et al., 1996). Additionally, for t_n to occur after the primary field has been removed ($t_n \geq 0$), $W[n,x]$ requires $-1/e \leq x \leq 0$. Thus, by Eq. (B.5):

$$\begin{aligned} -1/e &\leq -\left(\frac{t_\beta}{\tau_2}e^{\gamma}\right)^{3/2} \leq 0 \\ \implies e^{-\frac{2}{3}-\gamma} \approx 0.288267 &\geq \frac{t_\beta}{\tau_2} \geq 0 \end{aligned} \tag{B.6}$$

Recall that our choice in after-effect function (2.29) is only valid for $\tau_1 \ll t \ll \tau_2$. Therefore, the condition defined in expression (B.6) is reasonable under the assumption that $t_\beta \ll \tau_2$. We evaluated Eq. (B.5) for $n=0$ and noticed the solutions $t_0 \not\ll \tau_2$; which violates our conditions for the after-effect function. On the other hand, solutions of Eq. (B.5) for $n=-1$ were both physical and did not violate conditions for the after-effect function. Solutions obtained using $W[-1,x]$ consistently showed $t_\alpha \leq t_\beta$. As a result, the time t_α which solves $R_B = 1$ in expression (3.35) is given by:

$$t_\alpha \approx t_\beta \left(-W\left[-1, -\left(\frac{t_\beta}{\tau_2}e^{\gamma}\right)^{3/2} \right] \right)^{-2/3} \leq t_\beta \tag{2.51}$$